

Current Filamentation in Doped GaAs Corbino Disks

von
Dipl.-Phys. Georg Schwarz
aus Esslingen

Vom Fachbereich 4 (Physik)
der Technischen Universität Berlin
zur Verleihung des akademischen Grades
Doktor der Naturwissenschaften
genehmigte Dissertation

Berlin 2001
D 83

Arbeit eingereicht am 21. Dezember 2000

Tag der mündlichen Prüfung: 31. Januar 2001

Prüfungsausschuß:

Vorsitzender: Prof. Dr. Mario Dähne

Berichter: Prof. Dr. Eckehard Schöll, PhD
Prof. Dr. Udo Scherz

Zusammenfassung

Diese theoretische Arbeit beschäftigt sich mit der Musterbildung beim Stromtransport in dünnen dotierten GaAs-Filmen mit zwei konzentrischen Ringkontakten, sog. *Corbinoscheiben*. Experimentell war es kürzlich gelungen, den Stromfluß in solchen Proben mittels eines neuentwickelten Verfahrens orts aufgelöst abzubilden. Dabei waren ein oder mehrere Kanäle hoher Stromdichte, *Stromfilamente* genannt, in dem ansonsten niedrigleitenden Gebiet zwischen den beiden Kontakten gefunden worden.

Ein Ziel der vorliegenden Arbeit ist die Untersuchung der Bildungsdynamik dieser Strukturen, die in den Messungen bislang nicht zugänglich war. Dazu werden unter Einbeziehung eines Modells für den Tieftemperatur-Stoßionisationsdurchbruch in GaAs die klassischen Halbleitertransportgleichungen auf einem räumlich zweidimensionalen Grundgebiet numerisch gelöst.

Es zeigt sich daß, unabhängig von der Richtung der angelegten Spannung, sich zunächst eine radialsymmetrische Elektronendichtefront vom mittleren Kontakt her ausbreitet, die dann in fingerförmige Strukturen aufbricht. Jeder dieser *Streamer* bildet nach dem Erreichen der äußeren Elektrode ein Präfilament. Auf Grund der globalen Kopplung über die externe Beschaltung kommt es zu einem Wettbewerb zwischen den Präfilamenten, aus dem eines (oder einige wenige) als vollentwickeltes Filament hervorgeht, während die übrigen rekombinieren.

Der Ausbreitungsmechanismus der Front, deren Geschwindigkeit mehr als eine Größenordnung über der Driftgeschwindigkeit der einzelnen Ladungsträger liegt, wird herausgearbeitet. Er beruht wesentlich auf einer Abschirmung des elektrischen Feldes durch mittels Stoßionisation erzeugte freie Elektronen sowie auf der Geometrie der Probe. Es wird gezeigt, daß sich das verwendete Halbleitermodell formal auf das Standard-Streamermodell für Gase reduzieren läßt, was die hohe Ähnlichkeit zu den in diesen Systemen beobachteten Phänomenen erklärt.

Beim Anlegen einer Spannungsrampe kommt es zur aufeinanderfolgenden spontanen Entstehung mehrerer Filamente; das System zeigt Multistabilität und Hysterese in der Kennlinie in guter Übereinstimmung zu den experimentellen Ergebnissen. Unter dem Einfluß eines externen senkrechten Magnetfeldes wird eine Verkrümmung der Streamer in Richtung der Lorentzkraft beobachtet.

Abstract

This theoretical work deals with pattern formation in charge transport through thin doped GaAs films with two concentric ring contacts, so-called *Corbino disks*. Recently, the current flow through such samples had been visualized experimentally using a newly developed spatially resolved measurement technique. One or several channels of high current density between the two contacts, known as *current filaments*, were found embedded in the low-conducting rest of the sample.

One aim of this work is the investigation of the nucleation dynamics of those structures, which so far was not accessible experimentally. Making use of a model for the low temperature impact ionization breakdown in GaAs the classical semiconductor transport equations are solved numerically on a two-dimensional spatial domain.

An initial radially symmetric electron density front is found to expand from the central contact, regardless of the polarity of the applied bias, and then break up into finger-like structures. Upon reaching the outer electrode, each of those *streamers* forms a pre-filament. Due to the global coupling via the external circuit a process of competition occurs among the pre-filaments, one (or a small number) of which emerges as a fully developed filament, whereas the remaining ones recombine.

The propagation mechanism of the front, whose velocity is more than one order of magnitude higher than the drift velocity of a single carrier, is being resolved. It essentially depends on the screening of the electric field by free electrons produced through impact ionization as well as on the geometry of the sample. It is shown that the semiconductor model can formally be reduced to the standard streamer model in gases, which explains the high similarity to phenomena observed in those systems.

Applying a voltage ramp several filaments spontaneously form one after another; the system exhibits multistability and hysteresis in the current-voltage characteristic, in good agreement with experimental results. Under the influence of an external perpendicular magnetic field a twisting of the streamers in the direction of the Lorentz force is observed.

Teile der Ergebnisse dieser Arbeit wurden bisher bereits veröffentlicht in:
Parts of the results of this thesis have already been published in:

- G. Schwarz and E. Schöll. Simulation of current filaments in semiconductors with point contacts and Corbino disks. *Acta Technica CSAV*, 42, 669–684, 1997.
- G. Schwarz, C. Lehmann, and E. Schöll. Symmetry-breaking current instability in Corbino disks. In D. Gershoni, editor, *Proc. 24th International Conference on The Physics of Semiconductors (ICPS-24)*, Singapore, 1999. World Scientific Publishing (on CD).
- G. Schwarz, C. Lehmann, and E. Schöll. Symmetry-breaking multiple current filamentation in n-GaAs. *Physica B*, 272, 270–273, 1999.
- G. Schwarz, C. Lehmann, and E. Schöll. Self-organized symmetry-breaking current filamentation and multistability in Corbino disks. *Phys. Rev. B*, 61 (15), 10194–10200, 2000.
- G. Schwarz, C. Lehmann, A. Reimann, E. Schöll, J. Hirschinger, W. Prettl, and V. Novák. Current filamentation in n-GaAs thin films with different contact geometries. *Semicond. Sci. Technol.*, 15, 593–603, 2000.
- G. Schwarz, E. Schöll, R. Nürnberg, and H. Gajewski. Simulation of current filamentation in an extended drift diffusion model. In B. Fiedler, K. Gröger, and J. Sprechels, editors, *Proc. Equadiff 99*, volume 2, pages 1334–1336, Singapore, 2000. World Scientific Publishing.

Contents

1	Introduction	1
2	The underlying model	7
3	Simulations	16
4	Fronts and streamers	36
5	Multistability and hysteresis	56
6	Corbino disks in a transversal magnetic field	70
7	Conclusions	79
A	Material parameters	84
B	Analytical representations of the GR coefficients	85
C	Calculation of the steady state	87
D	A linear stability analysis	88

Chapter 1

Introduction

One basic aim of science, in particular of physics, is to develop a universal, yet precise understanding and description of the phenomena encountered in nature. The notion of universality is especially prevailing in the comparatively young scientific disciplines of nonlinear dynamics, often also referred to as “chaos science”, and pattern formation. Those disciplines investigate the temporal and spatio-temporal evolution of systems from different fields of science ranging from the study of live organism such as the growth of bacteria cultures, or brain or cortical activities, via cosmology, chemistry, or geophysical research like the forecast of earthquakes to socio-economic problems.

Semiconductors have proven to be versatile model systems for the study of nonlinear dynamics and pattern formation. They can easily be handled experimentally with an elaborate range of tempering and measurement techniques already available due to their technological and economic relevance. Modern growth technology such as molecular beam epitaxy (MBE) or metal organic chemical vapor deposition (MOCVD), developed to a high degree of perfection over the last 30 years, have enabled research to fabricate semiconductor samples with specific properties, i. e. “tailor” them to their individual needs. The global quantities like current or voltage can be directly measured and do not require any complicated preliminary conversion into electrical signals. By simply applying an external voltage, semiconductor devices can be driven far from thermodynamical equilibrium. Under high fields, semiconductors have been shown to exhibit a broad range of spatio-temporal phenomena, which can be conveniently controlled via external electrical signals and circuits. Moreover, there readily exist a number of well-tested theoretical models from different hierarchies for the description of the physical phenomena in semiconductor materials.

Transport instabilities in semiconductor materials, which can lead to the evolution of complex spatial, temporal, or spatio-temporal structures, can be characterized by a nonlinear dependence of the local current density j upon the local electric field \mathcal{E} . The two important generic cases are the N-shaped and the S-shaped current density-field characteristic (cf. Fig. 1.1). In the first case of N-shaped negative differential conductivity (NNDC), which arises for example through the Gunn effect, regions of different electric fields \mathcal{E}_1 and \mathcal{E}_2 can coexist for a given current density j . (The state corresponding to the field on the intermediate negative differential

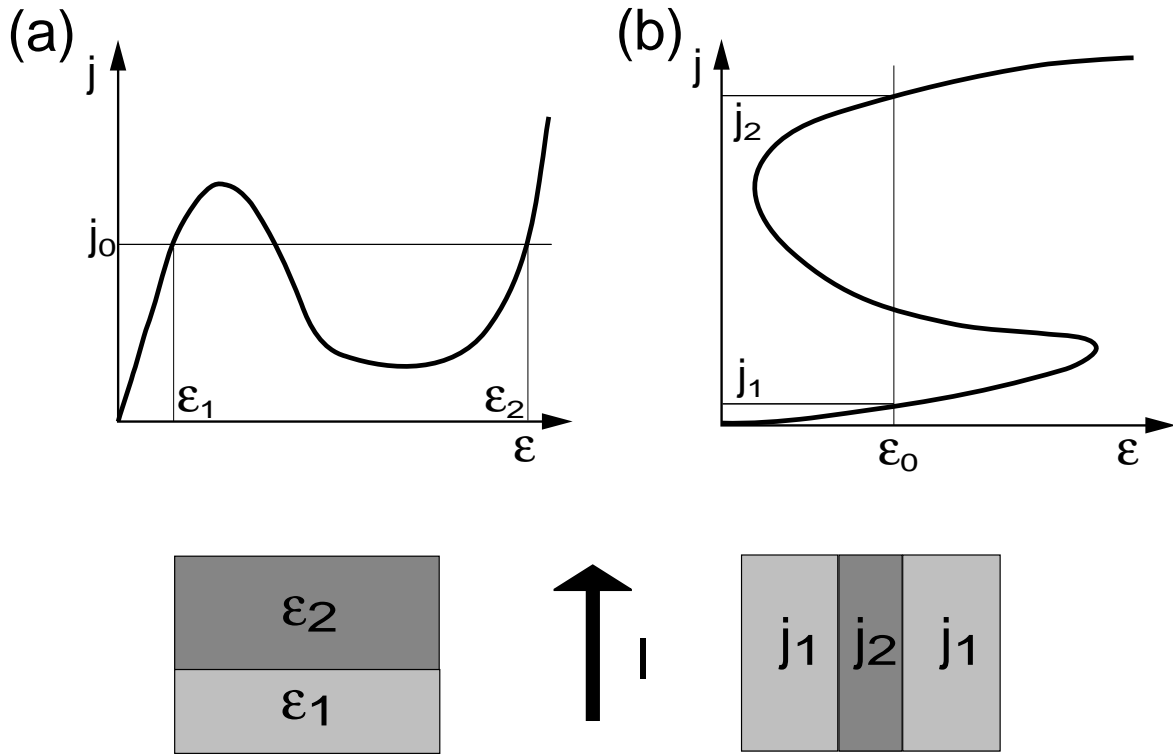


Figure 1.1: Schematic sketch of an N-shaped (a) and S-shaped (b) current density-field characteristic along with an example for bistability in the field (\mathcal{E}_1 , \mathcal{E}_2) and the current density (j_1 , j_2), respectively. The lower half depicts the typical resulting spatial structures, (a) domains and (b) filaments. The arrow indicates the direction of the current flow.

conductivity branch is typically unstable). This can lead to the development of electrical field domains, i. e. spatially inhomogeneous patterns in the direction of the current flow (cf. lower part of Fig. 1.1 (a)). For the case of S-shaped negative differential conductivity (SNDC) in turn a given electric field \mathcal{E} that lies within the region of bistability of the characteristic allows for two different current-densities $j_1 < j_2$. This can give rise to a channel of high current density j_2 , i. e. high conductivity, embedded in a region of low current density j_1 (cf. lower part of Fig. 1.1 (b)). Such a transversal structure is called a *current filament*.

In doped semiconductors at low temperatures transport instability arises through impact ionization of the electrons (or holes, for p-type material) from shallow impurities into the conductance band (or valence band, respectively). For sufficiently high electric fields, the newly created free carriers can themselves ionize further donors (or acceptors, respectively), leading to an impact ionization avalanche. This autocatalytic process, which can give rise to current filamentation, temporal oscillations and chaos, was modeled by SCHÖLL through a rate equation ansatz similar to chemical reaction equations [Sch87].

Experimentally, current filaments in thin semiconductor films were observed for p-Ge [May87] and for n-GaAs samples [May88] with the help of a scanning electron microscope through

electron beam induced current (EBIC). The surface of the semiconductor film is scanned line by line by a focused electron beam, and the resulting response of the sample current is recorded as a function of the scanning position. Within the walls of a filament the irradiation by electrons leads to a destabilization of the structure and thus a change in the current response, yielding a spatially-resolved picture of the shape of the current filament boundaries. A similar technique uses a scanning laser microscope to scan the sample surface [Bra89]. There the laser light leads to a creation of additional free carriers at the focal spot. In a region within a filament those additional free carriers can be neglected in comparison to the already existing free carrier concentration, thus they will not have any measurable effect on the sample current. In a region outside a filament, those extra free carriers are not sufficient to trigger a self-sustained impact avalanche, so there the sample current is not affected either. Only within the narrow area of transition between the low-conducting and the high-conducting sample regions, i. e. within the filament walls, the free carriers created by laser illumination are sufficient to locally enable an impact ionization avalanche. This again gives rise to a measurable change in the sample current when scanning across a filament boundary. That latter method is more suited particularly when studying the influence of an external magnetic field [Spa94], which would defocus an electron beam.

A highly successful imaging technique using *quenched photoluminescence* was developed by PRETTL and coworkers [Ebe96a, Pre97, Hir99]. Unlike the two scanning methods, which involve a localized irradiation that could mean a distortion of the pattern at that spot, the new technique uses a homogeneous illumination of the sample surface. That illumination, whose energy must be greater than the band gap, creates electron-hole pairs. Those electron-hole pairs can decay via radiative donor-acceptor pair recombination and exciton recombination. The emission of those two recombination channels, through a suitable optical filter, can simply be recorded by an infrared-sensitive camera. Within a filament however, the donor states (in case of an n-type material) will be depleted, which suppresses donor-acceptor and exciton recombination. Photoluminescence is thus locally quenched by the presence of a filament, and the respective regions will appear as darker areas on the camera image. Strictly speaking, that measurement technique does not directly visualize the local current density but the local degree of ionization of the donors.

The temporal resolution of that imaging technique is given by the speed of the camera, which can take a frame typically every 20 ms [Pre97]. The big advantage of the quenched photoluminescence technique over the previous two methods, in addition to its noninvasiveness to the current patterns, is the fact that it does not require any scanning of the thin-film sample but can directly produce a spatially resolved image of a filament that can be viewed in real-time.

Over the last two decades it has been demonstrated both in experiments as well as through analytic calculations using simple theoretical models and elaborate numerical simulations that impurity impact ionization at low temperatures can give rise to a multitude of spatio-temporal instabilities in semiconductors. Chaos in semiconductors was first observed by AOKI and coworkers [Aok81] and soon afterwards by TEITSWORTH *et al* [Tei83]. Using laser and electron beam scanning techniques it was possible to resolve the spatial structure of a current filament between two localized contacts in both p-Ge and n-GaAs samples. Theoretically, the instability of the homogeneous state was shown through a linear stability analysis [Sch87]. Early

theoretical work on current filamentation was restricted to spatially one-dimensional investigations. Breathing of cylindrical filaments [Sch90] as well as lateral movement of filaments under the influence of a perpendicular magnetic field [Hüp93c, Hüp93a] were obtained. Furthermore, simulations by HÜPPER exhibited intermittent and chaotic behavior [Hüp93c, Hüp93b], in agreement with experimental results. GAA found traveling waves in the direction of the current flow through a linear stability analysis and in one-dimensional longitudinal numerical simulations using periodic boundary conditions [Gaa96e].

An important step towards a better microscopically established theoretical description was the calculation of the specific field and concentration dependencies of the generation-recombination coefficients in the rate equations model for the cases of both p-Ge and n-GaAs, using a Monte Carlo simulation [Kuh93, Qua94, Hüp93a, Keh95]. KUNZ and in particular GAA made use of those Monte Carlo data for n-doped GaAs in numerical simulations on a two-dimensional spatial grid for current filamentation in thin-film samples with two point contacts located directly at the sample edges [Kun96c, Gaa96a, Gaa96b, Gaa96c]. The simulations gave insight into the nucleation process of a filament, showing that it evolves out of the initial nonconducting state via an intermediate *pre-filamentary* state into a fully developed filament. In that pre-filamentary state the shape of the current filament is already present with the free electron density and the current density being already notably higher within the pre-filament than in the surrounding non-conducting regions, but still a few orders of magnitude lower than in the later final filament. The results obtained for the shape of narrow filaments in the point contact geometry were in good agreement to experimental measurements in corresponding thin-film samples [Gaa96d].

Those simulations were extended by KUNIHIO to include the effect of an external magnetic field perpendicular to the sample surface [Kun96a, Kun97a, Kun97b]. There it was found that a field of the order of 10 mT leads to an asymmetric broadening of the current filament due to the Lorentz force. Also the electric field at the filament boundary, i. e. within the filament wall, which has to stabilize the filament against diffusion, was found to be increased at one side and decreased by the same amount on the other one. That asymmetric change in the strength of the boundary fields which is given by the additional force exercised by the magnetic field acting on the moving electrons had previously been observed experimentally in laser scanning measurements [Bra89].

A different approach was taken by NOVÁK. He numerically calculated the stationary solutions of the transport and generation-recombination equations for a one-dimensional transversal cross section through a current filament between two point contacts, assuming an unperturbed dipole structure for the electric field [Nov95a, Nov95b]. As a result, he found that diffusion could be neglected except within the narrow filament walls. There the electric field attains some critical value \mathcal{E}_c , which he could determine through comparison with experimental measurements. In the case of an additional perpendicular magnetic field an asymmetric transversal shift of the filament was obtained.

The results led him to the development of a phenomenological model for the description of the two-dimensional shape of a stationary filament [Nov96, Nov97a, Nov98b]. In that model the complicated kinetics of the different generation-recombination processes are hidden in a single

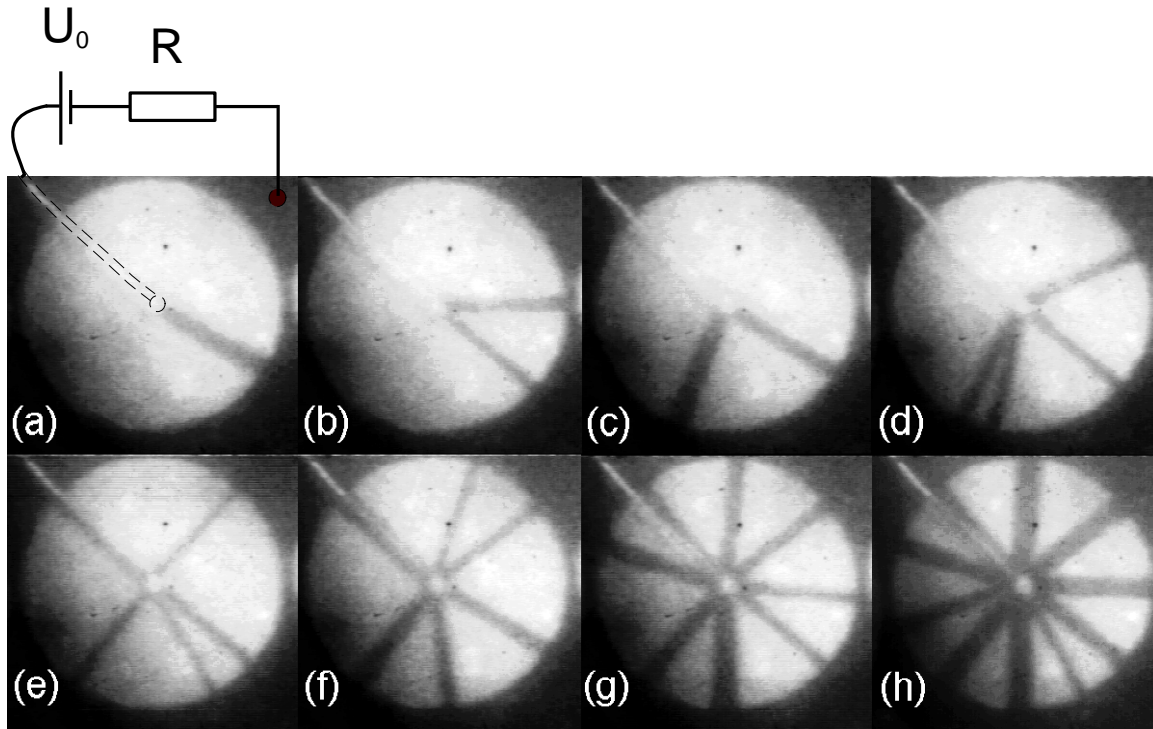


Figure 1.2: Experimental photoluminescence images of current filaments in a Corbino disk at different bias voltages (inner contact radius 0.04 mm, outer contact radius 1.05 mm, thickness of the epitaxial layer 3.0 μm). The dark areas correspond to regions of high current density. From (a) – (h) the total current I through the sample increases from 0.32 mA to 2.93 mA. (from [Hir97a])

S-shaped dependence of the conductivity σ on the field \mathcal{E} . His model furthermore assumes that the boundaries of a filament, where all gradients normal to the interface between the conducting and the non-conducting region have to vanish, are characterized by a specific constant transversal coexistence field \mathcal{E}_c . That way he arrived at a free boundary problem for the interface of the current filament which could be solved numerically. Those numerical results, which turned out to be in good agreement with the experimental findings, indicate that the shape of the contacts have a decisive influence on the shape of the fully-developed filament. They were confirmed by spatially two-dimensional simulations of broad current filaments by REIMANN for samples with two small circular contacts using the full dynamical generation-recombination model [Rei98, Sch00a].

For the latter sample geometry as well as for the previously considered samples with two point contacts located directly at the sample edges it was shown both experimentally and in simulations that the nascence of a filament can lead to a strong distortion of the electric field, i. e. the current flow does not follow the initial dipole field profile. This fact justifies the term of a *self-organized* filament [Gaa96d]. In those sample geometries the location of the filament, however, is strictly determined by the two sample contacts. In that respect the situation is qual-

itatively different in samples with two circular concentric contacts, so-called *Corbino disks*¹. Those Corbino disks mimic infinitely wide samples with stripe contacts, eliminating any lateral boundaries.

Current filaments in those sample geometries were visualized with the help of quenched photoluminescence by PRETTL and coworkers [Ebe96a, Hir97a, Hir97c, Hir97d]. It was found that for the application of a sufficiently high bias voltage a straight filament spontaneously forms between the two contacts (Fig. 1.2 (a)). With increasing applied voltage further filaments appear one after the other (Figs. 1.2 (b) – (h)).

Those experiments, however, cannot resolve the dynamical processes of the self-organized breaking of the symmetry and the nascence of a filament in those samples, which happen on a too short time scale. In order to study those phenomena one must perform numerical simulations of the dynamics of the full nonlinear generation-recombination and transport processes. That will be the subject of this thesis.

The aim of this research is thus twofold: at first, we want to resolve the processes which lead to the formation of current filaments in Corbino disk samples. Moreover though, the numerical investigation of current filamentation in that geometry, where filament formation constitutes a qualitatively different degree of self-organisation than in point contact geometries, also serves as a test to the underlying generation-recombination model, which has to inherently contain the necessary requisits for a spontaneous breaking of the radial symmetry if it is to reproduce current filamentation in a radially symmetric sample.

This thesis is organized as follows: after this introduction we will discuss in chapter 2 the theoretical model describing the low-temperature generation-recombination kinetics and charge transport in doped GaAs samples. In chapter 3 the numerical methods used for solving the resulting nonlinear dynamical system of partial differential equations (PDEs) are introduced. We will present simulations of the nucleation process of a current filament. Those simulations reveal that current filaments in a Corbino disk sample develop out of a radially symmetric super-fast impact ionization front through a symmetry-breaking instability. The nature of that impact ionization front will be analyzed in chapter 4, and it will be related to existing concepts of superfast switching in diodes and of “streamers”, rapidly progressing finger-like structures, encountered typically in ionizing gases. We will show that for the initial phase of filament formation the impact ionization model can in fact be formally reduced to the standard streamer model.

The following two chapters deal with a comparison of simulation results to corresponding experimental measurements. In chapter 5 we investigate the behavior of a sample subject to a bias ramp. We find multistability and hysteresis in the global current voltage characteristic, in good agreement with the experiment. In chapter 6 the influence of a external magnetic field normal to the sample surface is investigated. In the concluding chapter the results of the investigation are summarized, and questions that arise from them as well as possible further directions of research are discussed. The four appendices contain some additional technical material.

¹named after the Italian physicist Orso Mario Corbino (1876 – 1937)

Chapter 2

The underlying model

In this chapter we review the model used for the description of impact ionization in doped semiconductors at low temperatures. Originally developed by SCHÖLL [Sch82, Sch87], it has been used in spatially one-dimensional investigations for p-doped Ge [Sch90, Hüp93c, Hüp93b] and n-doped GaAs [Kun96b], as well as, more recently, in two-dimensional simulations of thin-film n-GaAs samples with two point contacts [Kun96a, Kun96c, Gaa96b, Gaa96c, Gaa96d, Gaa96e, Kun97a, Sch00a]. In this work we will also apply it to the simulation of Corbino disks [Sch97, Sch99a, Sch99b, Sch00b, Sch00c].

Since we are dealing with sufficiently doped semiconductor material we consider only charge transport through the majority carriers (i. e. electrons in the case of n-GaAs, which we shall assume in the following, although p-doped material can be treated analogously). Furthermore, lacking processes like optical excitation, we can neglect band-band transitions. It is therefore sufficient to consider electronic transitions between the localized donors and the conduction band states only.

In order to retain a computationally manageable model, we make use of a macroscopic level of description, characterizing the occupation of donor and conduction band states through electron densities instead of wave functions or distribution functions as in a quantum mechanical or a semi-classical model, respectively [Sch98a]. Since we are interested in stationary filaments, i. e. the coexistence of a low conducting and a high conducting phase, it is necessary for the model to exhibit bistability. It can be shown [Sch87] that in order to obtain a bistable system one needs to consider, apart from the electron density in the conduction band, $n(\underline{x}, t)$, at least two localized donor levels, $n_1(\underline{x}, t)$ and $n_2(\underline{x}, t)$. Here \underline{x} and t denote the spatial coordinate and time, respectively. While n_1 is the electron concentration in the donor ground state, n_2 is an 'effective' excited state which stands for the occupation of all the remaining excited states in the donor's hydrogen-like energy spectrum. The situation is sketched schematically in Fig. 2.1 along with the transition processes T_1^S , X_1^S , T^* , X^* , X_1^* , and X_1 considered in the model.

In our "hydrodynamic" semiconductor model the rate of change of the conduction band concentration can be expressed through the continuity equation

$$\dot{n} = -\underline{\nabla} \cdot \underline{j} + \phi(n, n_1, n_2, |\underline{\mathcal{E}}|) \quad (2.1)$$

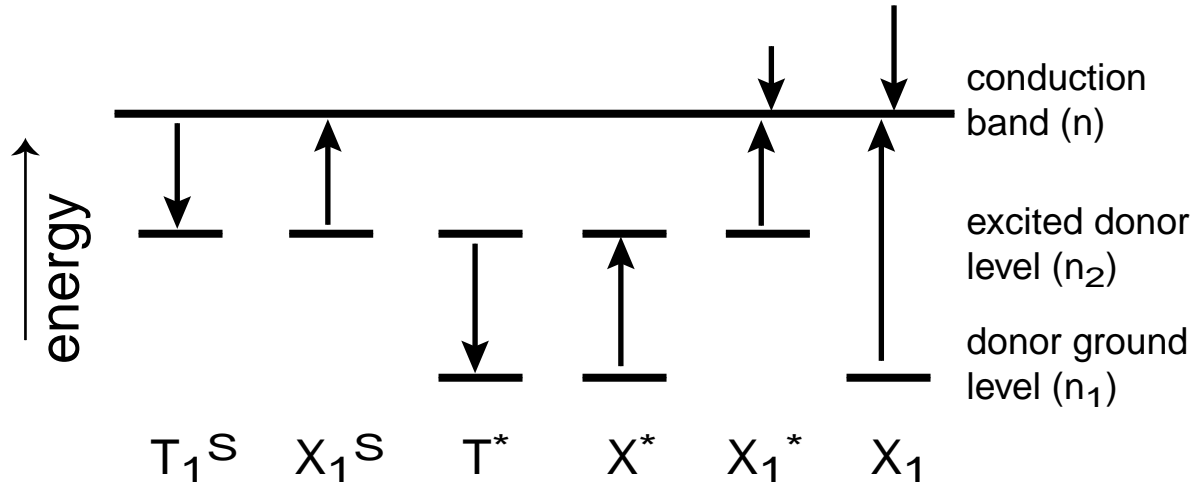


Figure 2.1: Two-level generation-recombination (GR) model for low temperature impact ionization in n-GaAs. n is the conduction band, and n_1 and n_2 are the localized donor ground and 'effective' excited level, respectively. T_1^S , X_1^S , T^* , X^* , X_1^* , and X_1 denote the GR processes considered.

with j the particle (i. e. electron) current density. Here, the dependence on time and space of the variables has been dropped for brevity. The net generation-recombination (GR) rate ϕ , which in eq. (2.1) takes the role of the source term, is a function of the electron concentrations n , n_1 , n_2 and of the strength of the local electric field $|\underline{\mathcal{E}}| = \mathcal{E}$. Analogously, the temporal evolution of the localized donor concentrations can be expressed as

$$\dot{n}_i = \phi_i(n, n_1, n_2, \mathcal{E}) \quad (2.2)$$

with $i = 1, 2$. For the reason of particle conservation,

$$\phi + \sum_i \phi_i = 0 \quad (2.3)$$

must always hold.

In the explicit two-level generation-recombination model [Sch87] the GR rates are given by the following rate equations:

$$\phi = X_1^S n_2 - T_1^S n p_t + X_1 n n_1 + X_1^* n n_2 \quad (2.4)$$

$$\phi_1 = T^* n_2 - X^* n_1 - X_1 n n_1 \quad (2.5)$$

$$\phi_2 = -\phi - \phi_1 \quad (2.6)$$

where N_D is the total density of donors and $p_t = N_D - n_1 - n_2$ the density of ionized donors. In eqs. (2.5), (2.6) X_1^S is the thermal ionization coefficient of the excited level, T_1^S is its capture coefficient, X_1 , X_1^* are the impact ionization coefficients from the ground and excited level,

respectively. X^* , T^* denote the transition coefficients from the ground level to the excited level and vice versa, respectively.

The two impact ionization coefficients as well as the capture coefficient into the excited donor level are functions of the electron concentrations and of the strength of the field: $X_1(n, n_1, n_2, \mathcal{E})$, $X_1^*(n, n_1, n_2, \mathcal{E})$, $T_1^S(n, n_1, n_2, \mathcal{E})$ (this dependence is suppressed in eqs. (2.5), (2.6)). It is this dependence that contains the essential nonlinearities of the model which are characteristic for the given material system. They can be obtained through a single particle Monte Carlo (MC) simulation which takes into account the relevant microscopic scattering processes.

For doped n-GaAs at liquid Helium temperature (4.2 K) such Monte Carlo simulations have been performed in [Keh95]. The microscopic rates of all band-impurity processes depend upon the electron densities in the conduction band and donor states. Those electron densities are calculated from the nonequilibrium carrier distribution function f . To obtain the carrier densities, the MC method has to be combined self-consistently with the rate equations (2.1)–(2.2) in the homogeneous steady state, where the GR coefficients X_1 , X_1^* , T_1^S are calculated by averaging the microscopic transition probabilities (P_{ii}^1 , P_{ii}^2 , P_{rec} for impact ionization from the ground state and from the excited state, and capture into the excited donor state, respectively) over the nonequilibrium electron distribution function $f(\underline{k})$, which is extracted from the MC simulation at each step:

$$\begin{aligned} X_1(n, n_1, n_2, \mathcal{E}) &= \frac{1}{nn_1} \int d^3k f(\underline{k}; n, n_1, n_2, \mathcal{E}) P_{ii}^1(\underline{k}, n_1), \\ X_1^*(n, n_1, n_2, \mathcal{E}) &= \frac{1}{nn_2} \int d^3k f(\underline{k}; n, n_1, n_2, \mathcal{E}) P_{ii}^2(\underline{k}, n_2), \\ T_1^S(n, n_1, n_2, \mathcal{E}) &= \frac{1}{np_t} \int d^3k f(\underline{k}; n, n_1, n_2, \mathcal{E}) P_{rec}(\underline{k}, p_t). \end{aligned} \quad (2.7)$$

Note that f and thus X_1 , X_1^* and T_1^S themselves depend parametrically on n , n_1 , n_2 and \mathcal{E} . An iterative procedure, where n_1 and n_2 are expressed by their steady-state dependence on n and \mathcal{E} , is used to obtain a self-consistent solution [Keh95].

One result of [Keh95] is that the impact ionization coefficients X_1 and X_1^* can be expressed as functions of just the electron temperature T_e . In this context the term *electron temperature* is meant as the second moment, i. e. the variance of the nonequilibrium energy distribution of the electrons, which for a heated Maxwellian amounts to the more usual definition as the temperature parameter in that distribution, but more generally can be applied to any energy distribution. T_e in turn depends on \mathcal{E} . However, this dependence turned out not to be unequivocal. For low free electron concentrations n we get a dependence $T_e^{lo}(\mathcal{E})$ while for n above a threshold value n_{th} a higher electron temperature $T_e^{up}(\mathcal{E})$ is obtained. This is shown in Fig. 2.2 where the Monte Carlo results are depicted as dots. The two lines represent an analytical fit of the MC data for T_e^{up} and T_e^{lo} , respectively. These smooth analytical representations for the electron temperature as well as for the GR coefficients have been derived by GAA [Gaa94, Gaa95, Gaa96b] and will be used in our numerical simulations. The detailed expressions can be found in appendix B.

The impact ionization rates X_1 and X_1^* , which can as well be expressed as functions of the electron temperature T_e , are depicted in Figs. 2.3 and 2.4, respectively, both as the MC results

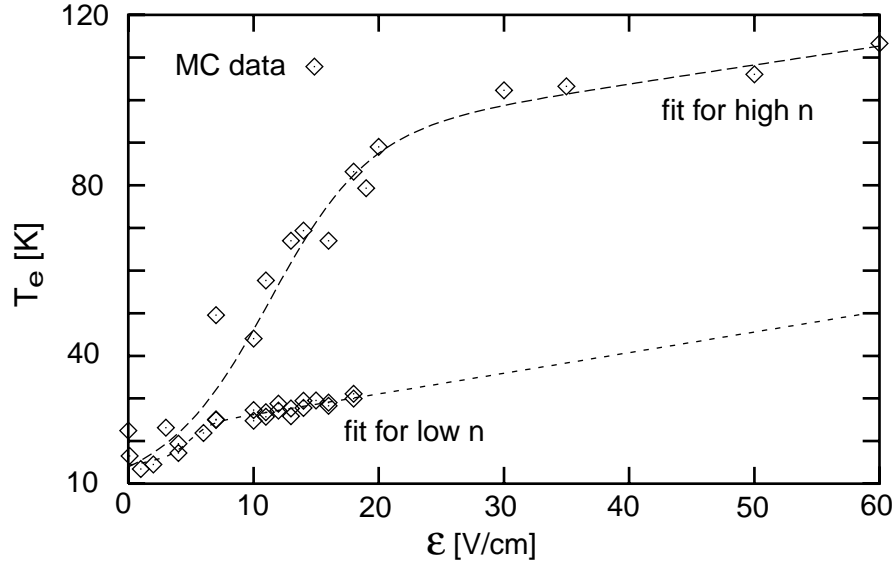


Figure 2.2: Electron temperature T_e as a function of the electric field \mathcal{E} for a free electron concentration n both below and above the threshold value n_{th} (from [Gaa94])

(single dots) and as fitted analytical representations (dashed curves). The recombination rate T_1^S (cf. Fig. 2.5) is a dual valued function of T_e , again with $T_1^S(T_e) = T_1^{Slo}(T_e)$ for a free electron concentration n below the threshold value n_{th} and $T_1^S(T_e) = T_1^{Sup}(T_e)$ for higher n . The remaining GR coefficients, X_1^S , X^* , and T^* , can be treated as constants. Their values for the case of n-GaAs are also found in appendix B.

For the conduction band particle current density \underline{j} we use the classical semiconductor drift-diffusion approximation

$$\underline{j} = -n\mu\underline{\mathcal{E}} - D\underline{\nabla}n \quad (2.8)$$

with the mobility μ and the diffusion constant D . For simplicity, we take μ as a constant and do not consider any dependence on \mathcal{E} , for example. This reflects the notion that the source for the filamentary instability is impact ionization. Thus the only nonlinearities of the model are contained in the GR rates. This is one important difference to other semiconductor systems like high field transport in doped superlattices [Pre94, Bon94] or to the Gunn effect where the essential nonlinearities can be expressed through a field dependence of the drift velocity [Sha92]. In this respect the model used here also differs from models for current filamentation developed by CHRISTEN [Chr94b, Chr94a] which include only a single impurity level and thus need a nonlinear field dependence of the carrier mobility to obtain an S-shaped current density-field characteristic.

For the relationship between μ and D we assume the Einstein relation (see e. g. [Ash76])

$$D = \mu k_B T_L / e \quad (2.9)$$

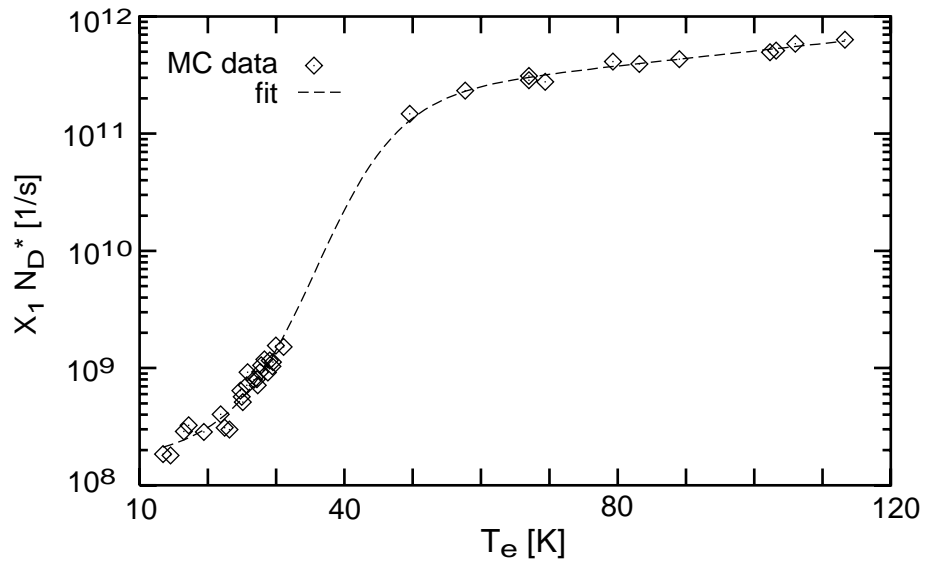


Figure 2.3: Impact ionization coefficient X_1 times the effective impurity concentration N_D^* as a function of the electron temperature T_e (from [Gaa94])

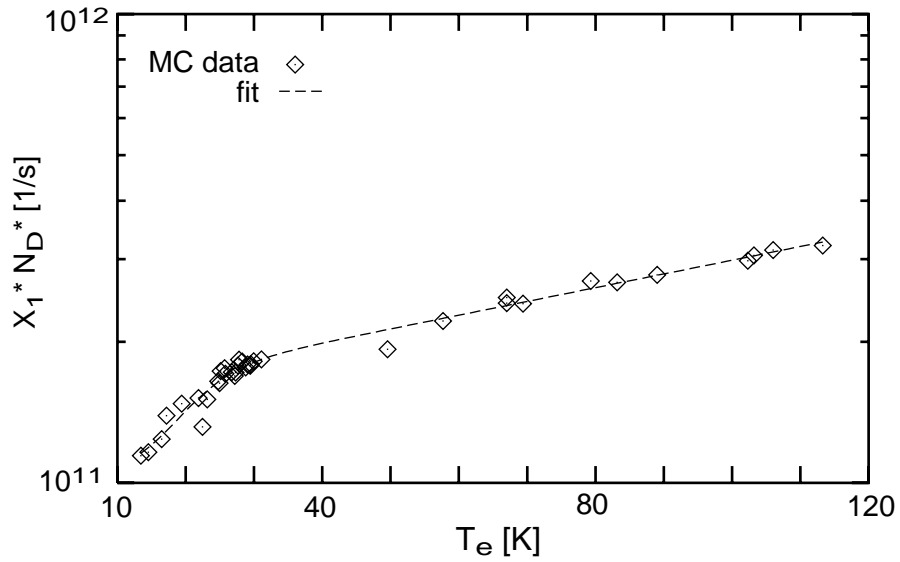


Figure 2.4: Impact ionization coefficient X_1^* times the effective impurity concentration N_D^* as a function of the electron temperature T_e (from [Gaa94])

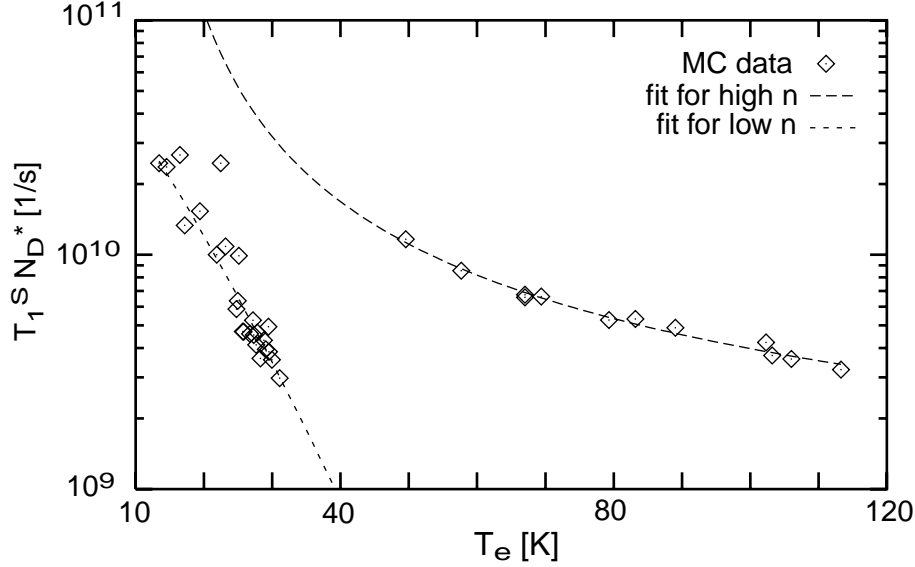


Figure 2.5: Recombination coefficient T_1^S times the effective impurity concentration N_D^* as a function of the electron temperature T_e for a free electron concentration n both below and above the threshold value n_{th} (from [Gaa94])

where k_B , T_L and e are Boltzmann's constant, the lattice temperature and the (positive) elementary charge, respectively. The various material parameters used for n-GaAs at liquid Helium temperatures are listed in appendix A.

The electric field is coupled to the carrier densities via Gauss's law

$$\epsilon \nabla \cdot \underline{\mathcal{E}} = \rho = e(N_D^* - n_1 - n_2 - n), \quad (2.10)$$

where ϵ is the dielectric constant for GaAs and $N_D^* \equiv N_D - N_A$ holds with the compensating acceptor concentration N_A .

It is important to note that none of the GR coefficients depends on n_1 or n_2 , just on the strength of the electric field \mathcal{E} (via T_e) and on the conduction band electron concentration n (which enters only through the ambiguity of T_e and T_1^*). Thus it follows directly from eqs. (2.5), (2.6) that ϕ and ϕ_i are linear in n_1 and n_2 . One can make use of this fact to directly calculate the steady state values of the donor electron densities n_1, n_2 for a given free electron concentration n and electric field \mathcal{E} [Sch87] (cf. appendix C).

In the steady state the charge density $\rho = e(N_D^* - n_1(n, \mathcal{E}) - n_2(n, \mathcal{E}) - n)$ is thus a function of n and \mathcal{E} only, $\rho(n, \mathcal{E})$. For a spatially homogeneous state, eq. (2.10) implies $\rho(n, \mathcal{E}) = 0$. The roots of $\rho(n, \mathcal{E})$, which can be solved numerically, are plotted in the n - \mathcal{E} parameter plane in Fig. 2.6. One obtains an S-shaped curve, i. e. within a certain field range $\mathcal{E}_h < \mathcal{E} < \mathcal{E}_{th}$ there exist three stationary state values $n_1 < n_2 < n_3$ of the free electron density for a given \mathcal{E} . For topological reasons n_1 and n_3 correspond to a stable stationary state while n_2 must be unstable (for constant field, i. e. under voltage controlled conditions). For the threshold and holding

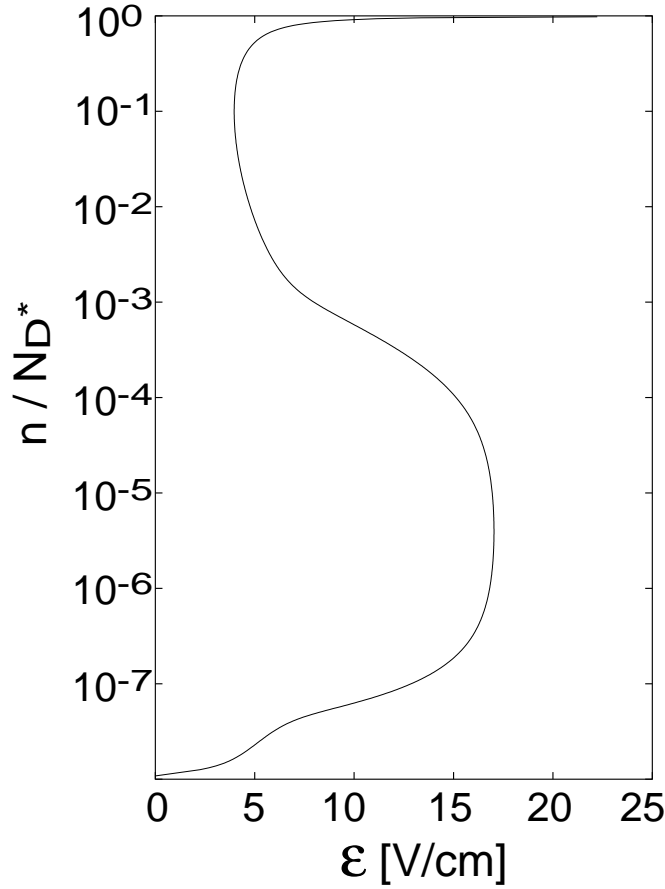


Figure 2.6: Solution of $\rho(n, \mathcal{E}) = 0$, i. e. electrically neutral configurations in the \mathcal{E} - n parameter plane

fields, where $\frac{\partial \rho}{\partial n}$ changes sign,¹ one reads off the values of $\mathcal{E}_{th} = 17$ V/cm and $\mathcal{E}_h = 4$ V/cm, respectively.

Since for a spatially homogeneous system, the diffusion term in eq. (2.8) vanishes and $j = n\mu\mathcal{E}$ holds the S-shaped n - \mathcal{E} characteristic directly results in an S-shaped j - \mathcal{E} characteristic (Fig. 2.7).

Some additional insight can be gained through the steady state distribution of the electron densities among the two localized donor levels and the conduction band. In Fig. 2.8 n , n_1 and n_2 are plotted along the steady state given by the S-shaped characteristic in Fig. 2.6. The curves are parametrized by the free electron density n . All three electron densities are scaled to units of the effective doping density N_D^* . On the low conductivity branch, corresponding to $\log_{10}(n/N_D^*) < -5.4$, the electron density in the donor ground level is virtually equal to the effective doping density N_D^* , while n_2 and n are almost empty. On the intermediate branch $\log_{10}(n/N_D^*) <$

¹Since in the steady state $d\rho = \frac{\partial \rho}{\partial n}dn + \frac{\partial \rho}{\partial \mathcal{E}}d\mathcal{E}$ holds and $d\rho = 0$ all along the $\rho = 0$ curve $\frac{\partial \rho}{\partial n}$ must be zero at the holding and threshold points where the curve is vertical in the \mathcal{E} - n plane and thus $d\mathcal{E}$ vanishes.

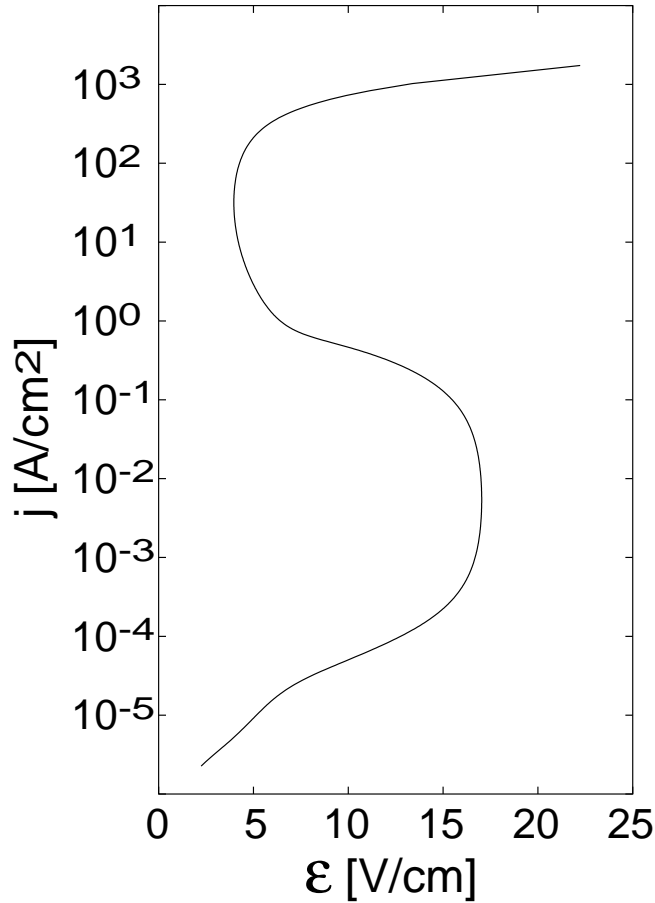


Figure 2.7: Calculated current density-field characteristic for n-GaAs (corresponding to the current-voltage characteristic for a completely homogeneous system)

$-1.0 = \log_{10}(n_{th}/N_D^*)$ the excited donor level n_2 becomes more and more populated at the expense of n_1 , and inversion between the ground and excited level sets in. With n approaching N_D^* on the S-shaped characteristic, both n_1 and n_2 must vanish since $n + \sum_i n_i = N_D^*$ must hold in the electrically neutral homogeneous steady state. The electron distributions show that for low electric fields, i. e. on the low conductivity branch, the generation-recombination cycle runs between the donor ground state and the conduction band, while on the high conductivity branch it is sustained by impact ionization of excited donor level electrons.

Combining a simple rate equation model approach with the results of a microscopic Monte Carlo simulation yields the advantage of having a microscopically founded description of the physical processes while at the same time retaining a system that is still computationally manageable on the macroscopic length and time scales required for the observation of pattern formation and even allows for some analytical considerations. It should be stressed that the model does not contain any experimental fitting parameters.

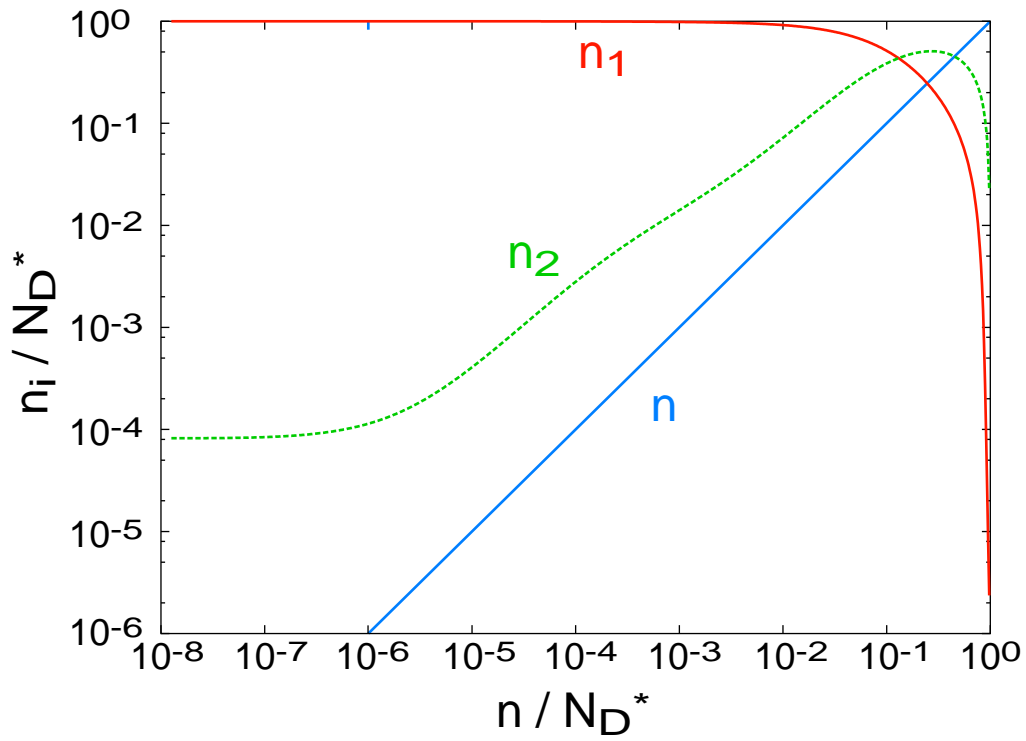


Figure 2.8: Calculated distribution of the electrons in the conduction band (n , blue) and donor ground and excited levels (n_1 , red, and n_2 , green, respectively) along the S-shaped characteristic in Fig. 2.6 representing the homogeneous steady states of the system. All densities n , n_1 , n_2 are given in units of the effective doping concentration N_D^* .

Chapter 3

Simulations

Following the outline of the underlying impact ionization model in the previous chapter we now turn to the numerical aspects of investigating current filamentation in GaAs. After an introduction at the beginning of this chapter to the numerical methods used to solve the semiconductor equations we present simulations of the nucleation of a current filament in a Corbino disk.

Although in special cases and under simplifying assumptions an astonishingly broad range of results can be gained through mere analytical considerations [Sch87] it normally takes a numerical approach to solve the full nonlinear system (2.1) – (2.10). This is particularly true for the Corbino disk geometry where, unlike in e. g. an infinitely long sample with stripe contacts, a zero-dimensional (i. e. spatially homogeneous) or an effectively one-dimensional treatment [Sch90, Kun92, Hüp93b, Hüp93c] is no longer sufficient to describe current filamentation.

To self-consistently solve eqs. (2.1), (2.2) and (2.10) we make use of the semiconductor simulation package *TeSCA*¹ [Gaj91]. It had originally been developed for the simulation of charge transport in Silicon devices but was later extended to include the low temperature impact ionization kinetics in n-GaAs [Kun96c, Sch00c].

It should be noted that due to the drift term in eq. (2.8) the numerical solution of the basic semiconductor equations, i. e. a drift-diffusion-reaction system, demands for considerably higher numerical stability of the algorithms involved than for example a reaction-diffusion model, which is often taken as a prototype for spatio-temporal pattern formation in dissipative systems [Mor98].² We make use of an implicit finite element scheme in space combined with a semi-implicit Euler scheme in time and efficient time-step control [Gaj93]. *Semi-implicit* here means that while for the critical transport terms (2.8) an implicit algorithm is employed to achieve the necessary numerical stability, the low-temperature generation-recombination processes for GaAs (eqs. (2.4), (2.5)), which have subsequently been implemented into the code, are treated in an explicit manner only.

¹Originally called *ToSCA*, short for Two-Dimensional Semi-Conductor Analysis Package, the name was slightly changed in 1999 due to trademark issues.

²For the pitfalls involved with numerically solving different types of partial differential equations (PDEs) see e. g. [Pre92]. A general introduction to the numerical treatment of the classical semiconductor transport equations can be found in [Sel84].

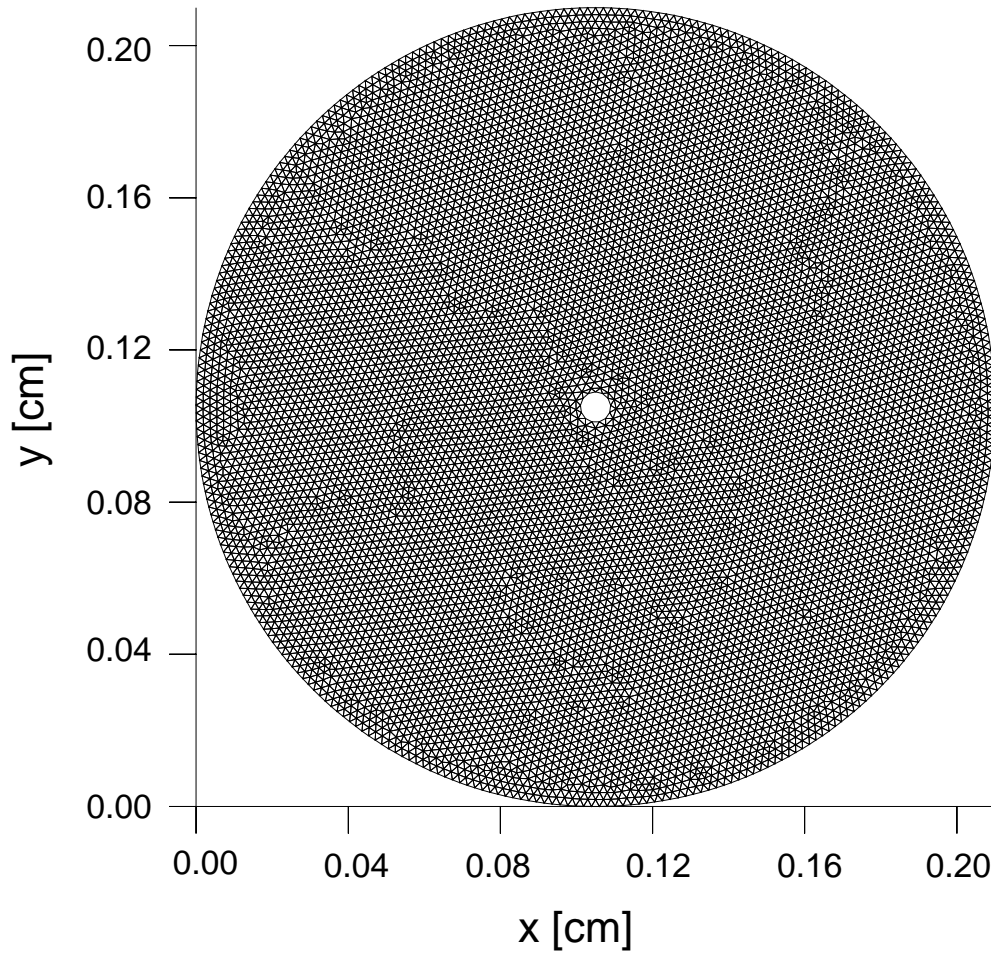


Figure 3.1: Typical spatial grid used by the finite element algorithm to simulate charge transport in a Corbino disk sample. (9989 mesh points combined into 19648 triangles, contact radii $R_1 = 0.04$ mm and $R_2 = 1.05$ mm with $N_1 = 13$, $N_2 = 317$ boundary points)

Since we are interested in spatial patterns in thin-film samples we consider current filamentation on a two-dimensional domain, effectively treating the sample thickness d as a mere scaling parameter for the total current. The finite element discretization requires the partition of the simulation domain into triangular subdomains. For reasons of numerical stability each triangle should be as equilateral as possible. To solve this problem we make use of the *EasyMesh* tool [Nic97] which employs a Delaunay triangulation algorithm in order to generate a suitable grid. EasyMesh requires the boundaries of the domain to be specified as polygons, whose number of points determine the density of points within the domain. For a Corbino disk we specify two closed polygons which approximate two concentric circles of radii $R_1 < R_2$. For the number of points of each of the two polygons, N_1 and N_2 respectively, we would choose primes in order to avoid, as much as possible, any artificial symmetry induced through the grid. A typical grid used in the simulations is shown in Fig. 3.1. It is made up of 9989 mesh points combined into 19648 triangles ($N_1 = 13$, $N_2 = 317$, $R_1 = 0.04$ mm, $R_2 = 1.05$ mm). It should be mentioned

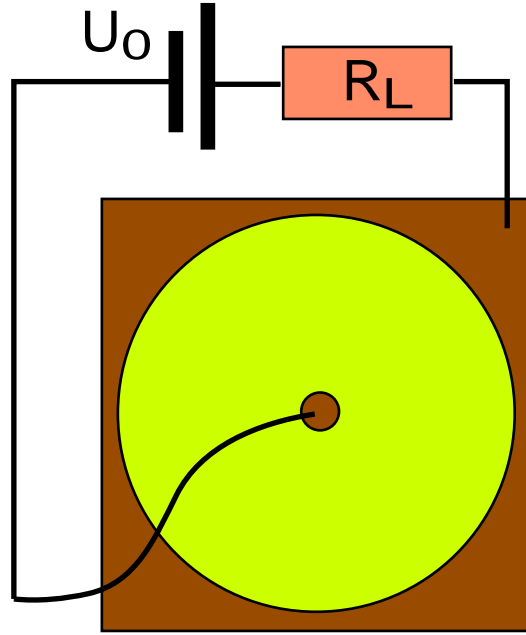


Figure 3.2: Schematic sketch of the Corbino disk sample in the electric circuit with load resistance R_L , voltage source U_0 .

that neither the mesh generator nor the simulation algorithm has any explicit knowledge of or makes any explicit assumption about the radial symmetry of the domain.

One major disadvantage of TeSCA's approach is the fact that it uses a grid which is fixed in time as opposed to some more complex adaptive grid algorithm. This is of particular concern when dealing with moving fronts, i. e. sharp gradients whose position traverses across almost the entire sample domain during the simulation. To still retain numerical stability and avoid artefacts a comparatively large total number of grid points and thus a respective amount of computing time, memory and storage is required.

The two circular Ohmic contacts of the Corbino disk we model as a carrier reservoir by applying Dirichlet boundary conditions for the free electron density n , which is fixed to N_D^* at the inner and outer radii, R_1 and R_2 , respectively.

We consider the sample to be biased by a DC voltage source U_0 via a load resistance R_L (cf. Fig. 3.2). For the voltage U across the sample Kirchhoff's law holds:

$$U = U_0 - R_L I. \quad (3.1)$$

Here, I is the total current through the sample, which is an integral quantity of the current density. In our nomenclature, we will denote the voltage U as *positive* if the cathode, i. e. the injecting contact for the electrons, is located at the inner contact (R_1) and as *negative* for reversed polarity.

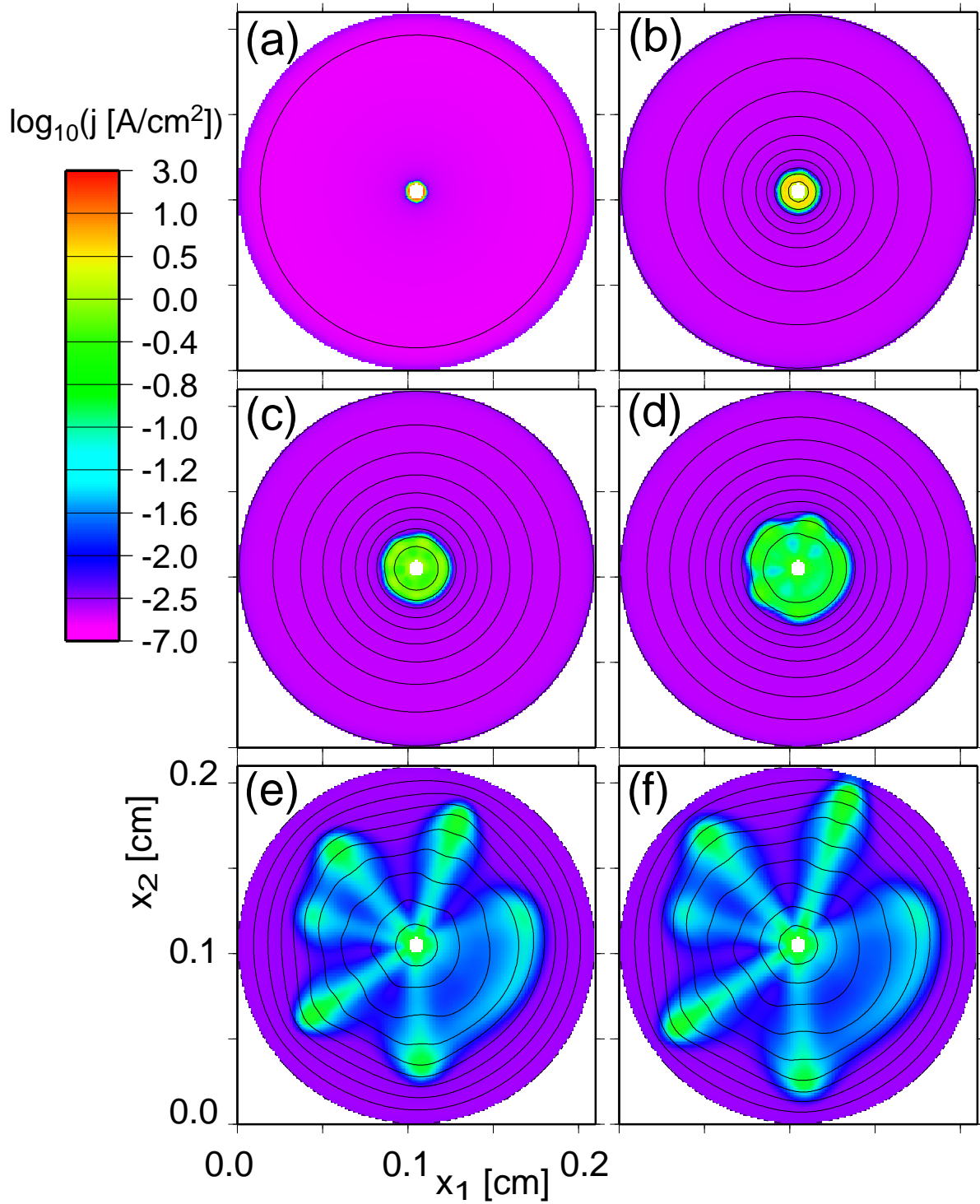


Figure 3.3: Simulation of the nascence of a current filament in an n-GaAs thin film Corbino disk sample with contacts radii $R_1 = 0.04$ mm, $R_2 = 1.05$ mm and an applied bias of $U_0 = 1.95$ V. From (a) – (f) the spatial distribution of the current density j is plotted for different times t : (a): $t = 1$ ps, (b): $t = 0.07$ ns, (c): $t = 0.15$ ns, (d): $t = 0.3$ ns, (e): $t = 1.3$ ns, (f): $t = 1.5$ ns. Equipotential lines are plotted spaced by 0.2 V. (continued on the next page)

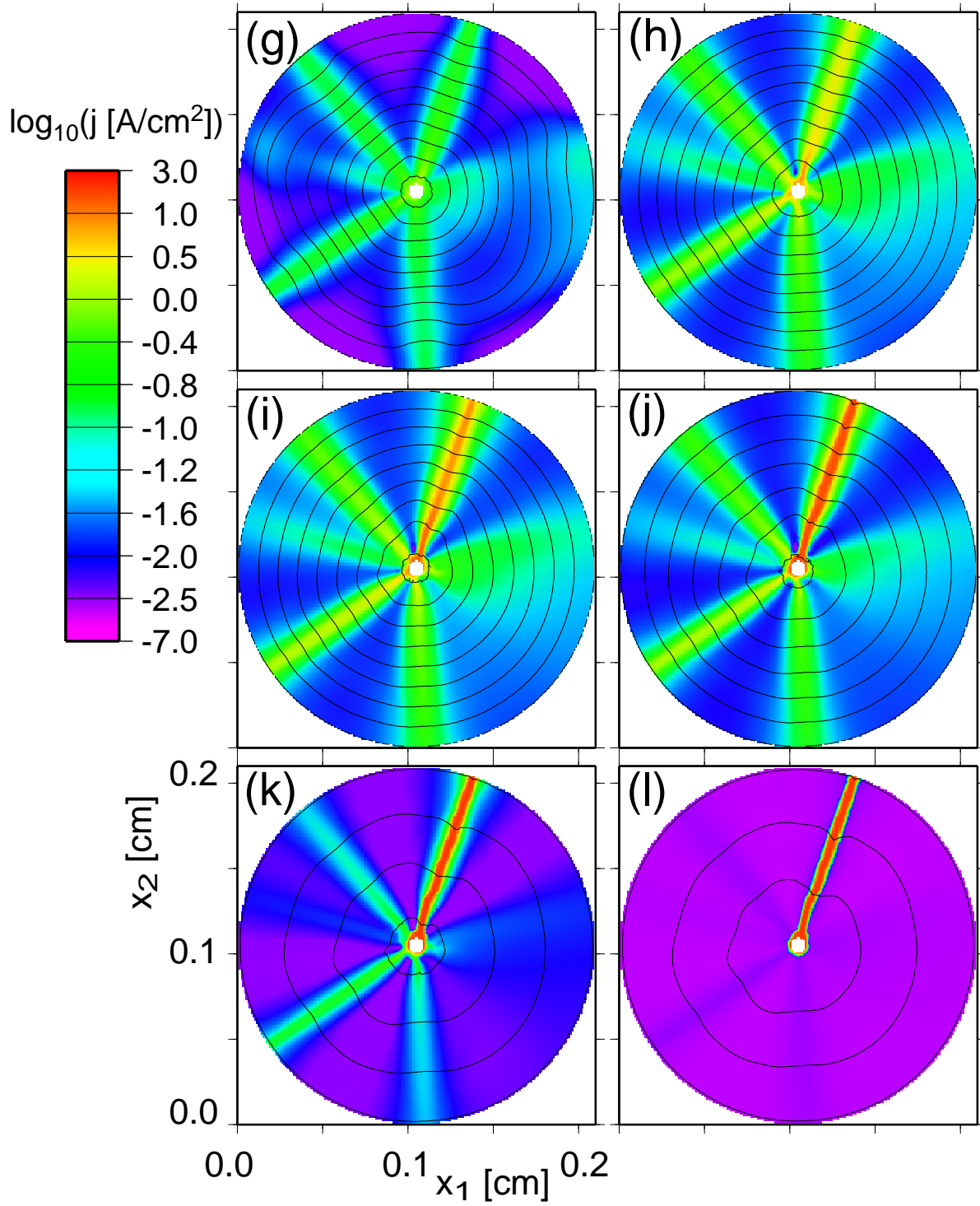


Figure 3.3: Simulation of the nascence of a current filament in an n-GaAs thin film Corbino disk sample with contacts radii $R_1 = 0.04 \text{ mm}$, $R_2 = 1.05 \text{ mm}$ and an applied bias of $U_0 = 1.95 \text{ V}$. From (a) – (l) the spatial distribution of the current density j is plotted for different times t : (g): $t = 2.5 \text{ ns}$, (h): $t = 5.0 \text{ ns}$, (i): $t = 5.7 \text{ ns}$, (j): $t = 6.0 \text{ ns}$, (k): $t = 6.5 \text{ ns}$, (l): $t = 10.0 \text{ ns}$. Equipotential lines are plotted spaced by 0.2 V . (continued from previous page)

For time $t = 0$ TeSCA starts the simulation from the equilibrium (i. e. $U_0 = 0$) distribution of the electron densities n , n_1 , n_2 , which are homogeneous except near the contacts. In the simulation we initially apply the bias U_0 in a linear voltage ramp of 1 ps, after which U_0 is kept constant.

We first consider a radially symmetric sample with contact radii $R_1 = 0.04$ mm, $R_2 = 1.05$ mm and thickness $d = 3$ μ m with an applied bias of $U_0 = 1.95$ V and a load resistance of $R_L = 10$ k Ω . Those values have been chosen to match the typical configuration of the experiments [Hir97a, Hir97d]. The spatial grid used in the numerical simulation is the triangulation depicted in Fig. 3.1.

Fig. 3.3 shows the spatial distribution of the current density j as a logarithmic color plot at different times t after the onset of the voltage ramp. In Fig. 3.4 the corresponding spatial free electron density profiles are depicted. The thin black lines denote electrical equipotential lines spaced by 0.2 V. Note that in the current density series a non-uniform color scale has been chosen as a compromise to best visualize the relevant spatial patterns during all stages of the filamentation process, which involves a difference in magnitude of several orders in both current and electron densities.

Initially at $t = 1$ ps, when the voltage ramp has reached its final value of $U_0 = 1.95$ V, we still have an almost homogeneous, nonconducting state (Figs. 3.3, 3.4 (a)). This shows that on the relevant time scale the bias U_0 can be regarded as instantaneously applied. The equipotential lines are concentric circles³. Only around the inner contact, the cathode, a small region of increased current density has formed. That central region of increased current density starts to expand in diameter (Fig. 3.3 (b) at $t = 0.07$ ns), forming a concentric current density front departing from the cathode. The free electron density within that region is about $n = 10^{12}$ cm⁻³, which is already four orders of magnitude higher than in the rest of the sample, i. e. we can speak of a sharp electron density front expanding into the nonconducting region (Fig. 3.4 (b)).

For about $t = 0.15$ ns (Figs. 3.3, 3.4 (c)) that front is already noticeably modulated. Moreover, we can clearly see that the equipotential lines just ahead of the advancing front get squeezed, indicating a locally increased potential gradient, i. e. a higher field in that region, while behind the front the density of the equipotential lines, i. e. the electric field strength, is considerably lower than in the initial field distribution.

With further expansion of the front its radial symmetry gets more and more lost. At $t = 0.3$ ns (Figs. 3.3, 3.4 (d)) it has clearly broken up into six “fingers”, which we will call “streamers” for reasons that will be motivated in detail in the next chapter. Each of those streamers continues towards the outer ring electrode with their rounded “heads” penetrating into the low-conductivity region ahead of them and again leading to a locally increased curvature and squeezing of the equipotential lines. Along the “tails” of the streamers, where the free electron density is somewhat lower than in the streamer heads but still considerably higher than in the nonconducting region, the equipotential lines are straight equidistant lines across the streamer’s width, indicating a constant field along each of them. The latter can easily be explained as a requirement

³due to the high turn-on current I – cf. Fig. 3.5 – the sample voltage U is quite small in Fig. 3.3 (a). For the chosen $\Delta U = 0.2$ V of this series only one equipotential line is visible. Only in Fig. 3.3 (b), when I has sufficiently decreased, does the increase of the distances between the equipotential lines with increasing radial coordinate r become visible, as expected for a $1/r$ field distribution in an electrically neutral radially symmetric system.

from the continuity equation. Thus the streamers already strongly distort the initial concentric $1/r$ field distribution (cf. Figs. 3.3, 3.4 (e) at $t = 1.3$ ns).

The speed of advance slightly varies among the six streamers, with the fastest one expanding at about $v_s = 6 \cdot 10^7$ cm/s. This is about the same as the expansion velocity of the initial circular front, but it is more than one order of magnitude higher than the drift velocity $v_d = \mu \mathcal{E} = 4 \cdot 10^6$ cm/s taken at the highest field $\mathcal{E} = 40$ V/cm just at the heads of the streamers. That fact already clearly indicates that what we see cannot be just a wave of individual carriers drifting from the cathode to the anode, but instead must be a collective phenomenon. That aspect will be further elaborated in the following chapter where the nature of the front is investigated.

At about $t = 1.5$ ns (Figs. 3.3, 3.4 (f)) the fastest of the six streamers reaches the anode with the other ones following within about the next ns (Figs. 3.3 3.4 (g)). That first streamer is also the strongest, most prominent one, and it is the one that has first dissolved from the front. The two slowest streamers are barely visible in the color density plot of the current density due to the particular color scale selected, but their presence can clearly be seen through the distortion of the equipotential profile from circular to locally straight, parallel, equidistant equipotential lines.

Having reached the outer contact the streamers, the free electron density within which is still three orders of magnitude below the effective doping density $N_D^* = 5 \cdot 10^{15}$ cm $^{-3}$, now each constitute a pre-filament. The free electron density within those pre-filaments starts to slowly increase as a result of the ongoing impact ionization (Fig. 3.4 (h) at $t = 5$ ns). Consequently the current densities of the streamers and thus the overall current I also increases (Fig. 3.3 (h)). This can be seen in Fig. 3.5 where the red curve shows the total current I through the sample on a logarithmic scale over time. The letters indicate the corresponding spatial profiles in Figs. 3.3, 3.4.

At about $t = 5.7$ ns it becomes apparent that the pre-filament which had formed first has grown the fastest (Figs. 3.3, 3.4 (i)). Its free electron density rises above $n_{th} = 0.1 N_D^* = 5 \cdot 10^{14}$ cm $^{-3}$. Consequently, impact ionization in that filament is greatly enhanced leading to a fast further increase of n and thus j in that pre-filament (Figs. 3.3, 3.4 (j) at $t = 6.0$ ns).

As a consequence of the sharp increase of the total current I (cf. Fig. 3.5) the voltage drop across the external resistance R_L also increases, leading to a drop in the sample voltage U according to Kichhoff's law (3.1) and thus in the electric field \mathcal{E} of each of the pre-filaments. This can also be seen from the expanding equipotential lines in Figs. 3.3, 3.4 (j), (k), (l). As a result of the decline of the field, the free electron density in the remaining five "later" pre-filaments starts to recombine (Fig. 3.4 (k) at $t = 6.5$ ns), which brings about a decline of their current densities as well (Fig. 3.3 (k)).

After 10 ns we are left with a single fully developed current filament (Figs. 3.3, 3.4 (l)); the other pre-filaments have died out. This result matches with the measured stationary current profile in Fig. 1.2 (a). Note also that as in the experiments the remaining filament has very sharp, parallel boundaries. Its width does not increase with increasing radial coordinate r inspite of the symmetry of the sample. This is a direct evidence of self-organization, which has already been found in experiments and numerical simulations of current filamentation between two point contacts [Gaa96b].

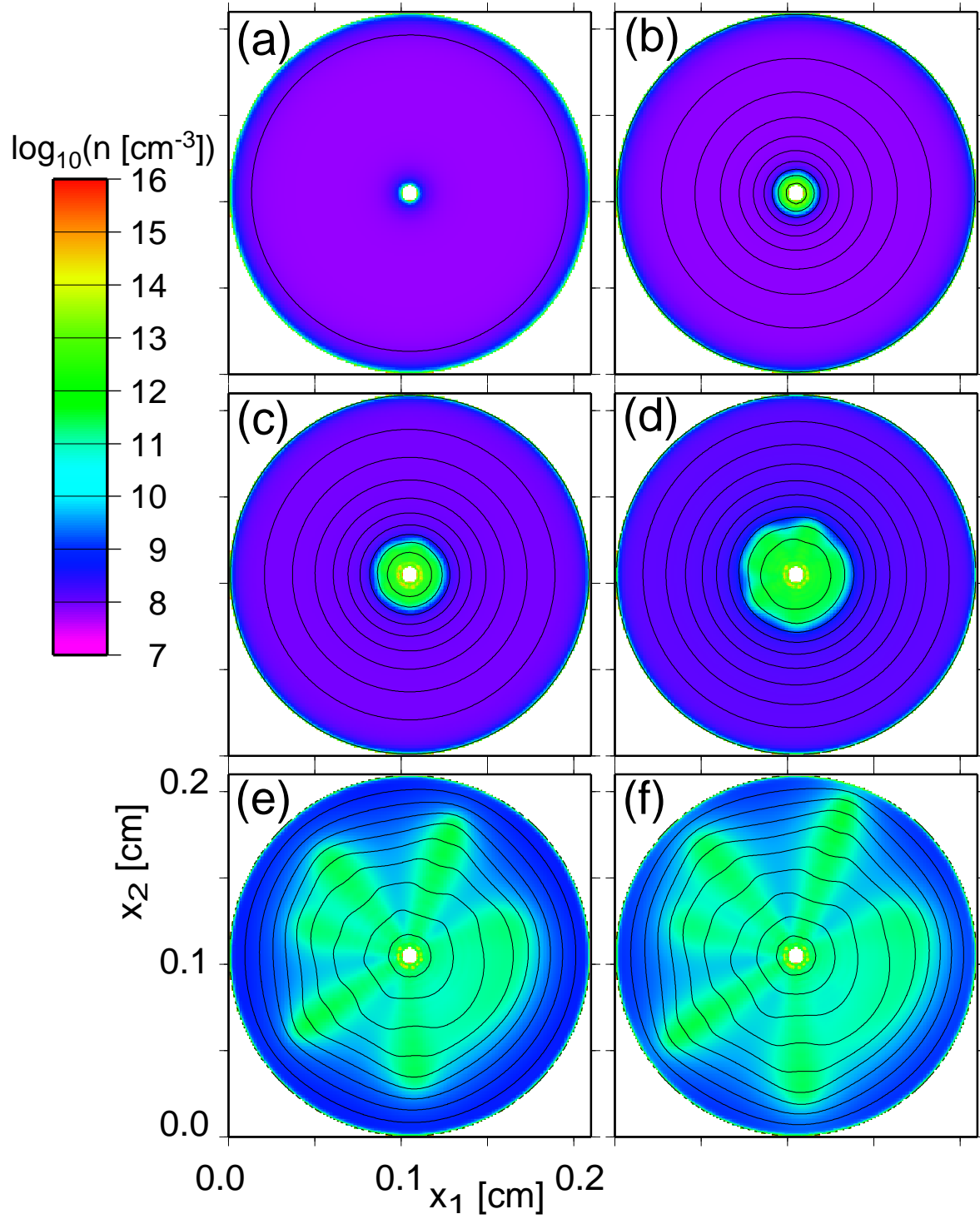


Figure 3.4: Calculated spatial profiles of the free electron distribution n and equipotential lines corresponding to the current density profiles of Fig. 3.3. (continued on the next page)

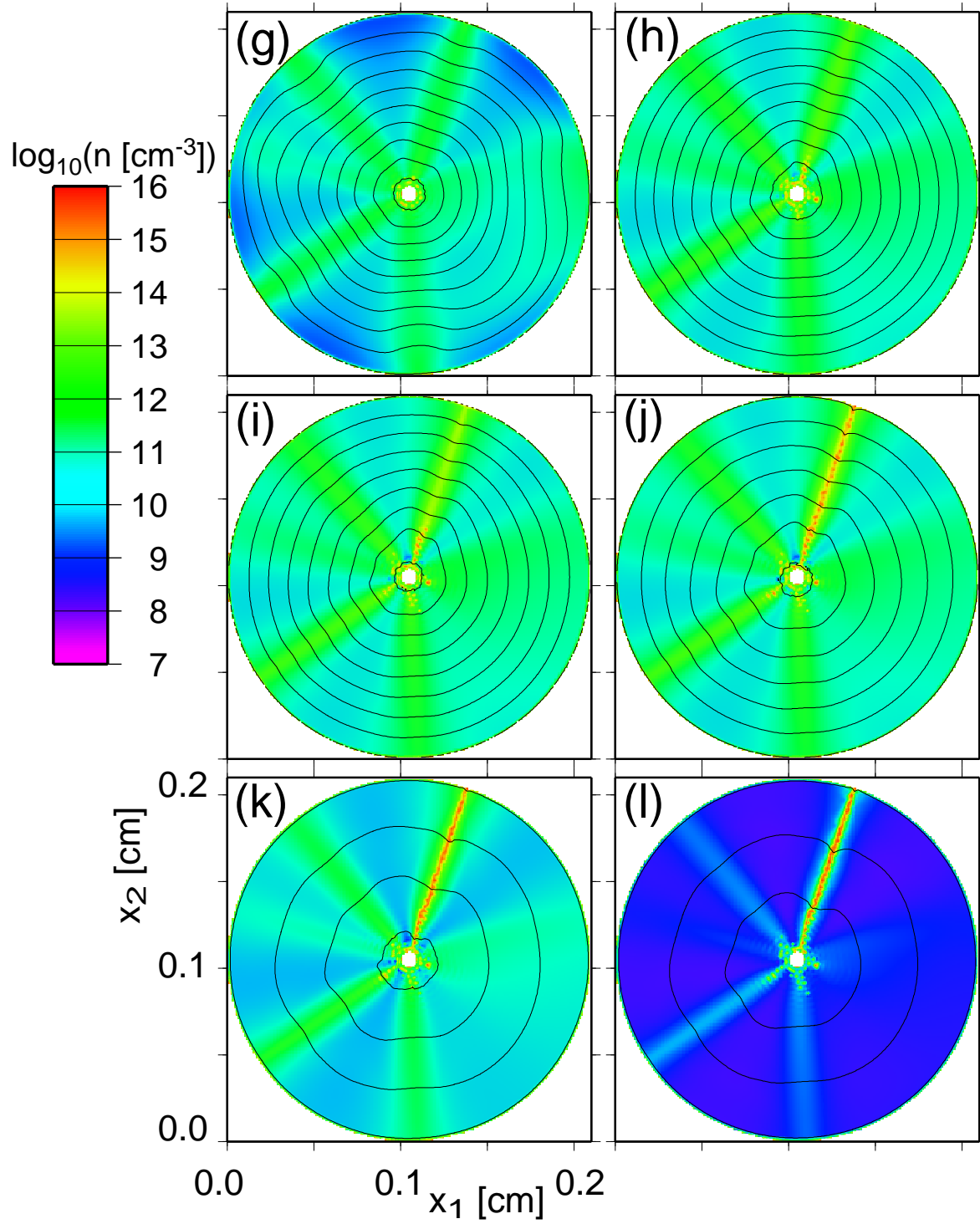


Figure 3.4: Calculated spatial profiles of the free electron distribution n and equipotential lines corresponding to the current density profiles of Fig. 3.3. (continued from previous page)

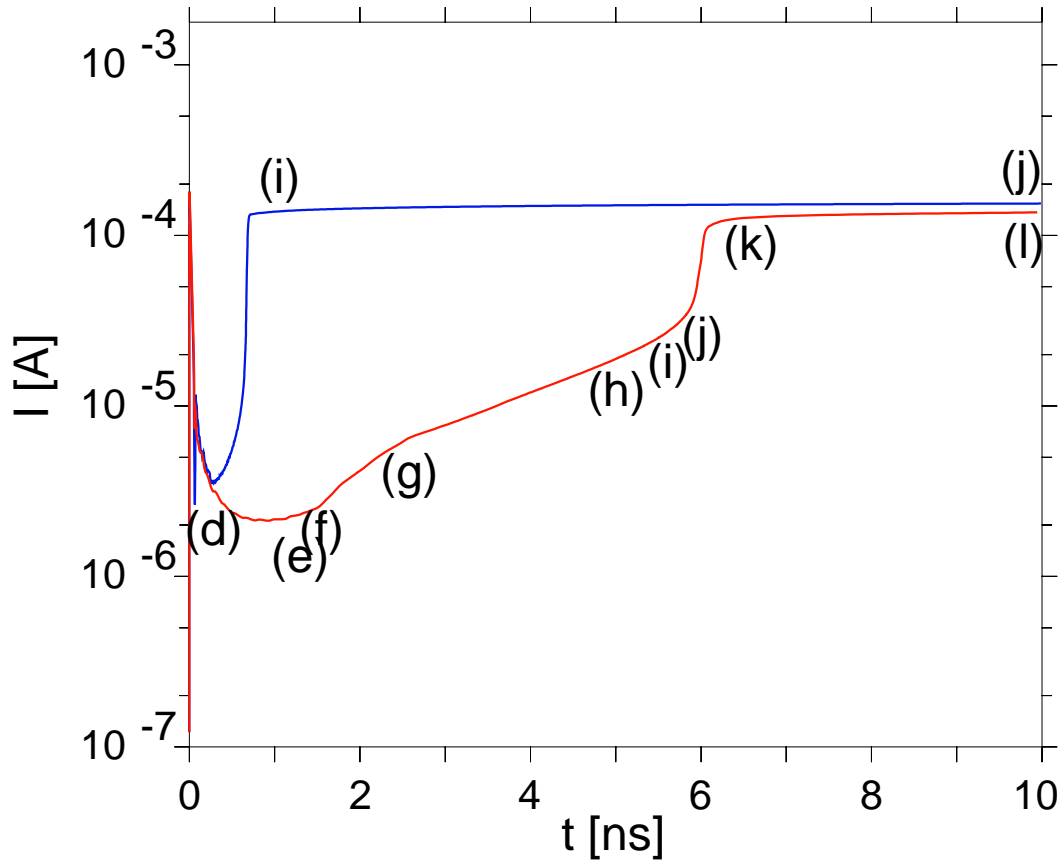


Figure 3.5: Total current I vs. time t during the formation of a current filament in a Corbino disk for a bias voltage $U_0 = 1.95$ V (red curve) and $U_0 = -1.95$ V (blue curve). The letters indicate the corresponding spatial profiles depicted in Figs. 3.3, 3.4 and Figs. 3.7, 3.8, respectively.

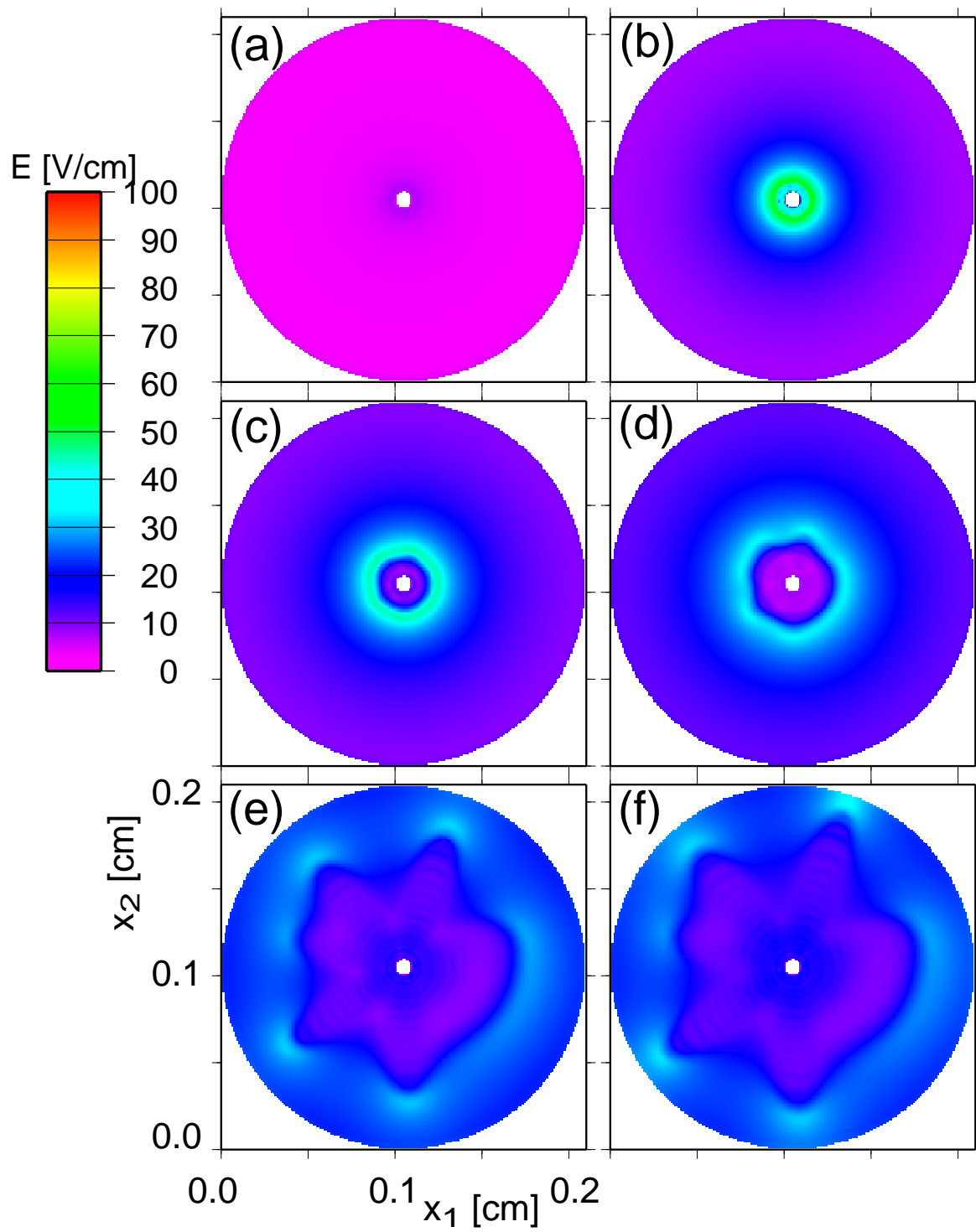


Figure 3.6: Calculated spatial profiles of the electric field E corresponding to current density profiles of Fig. 3.3. (continued on the next page)

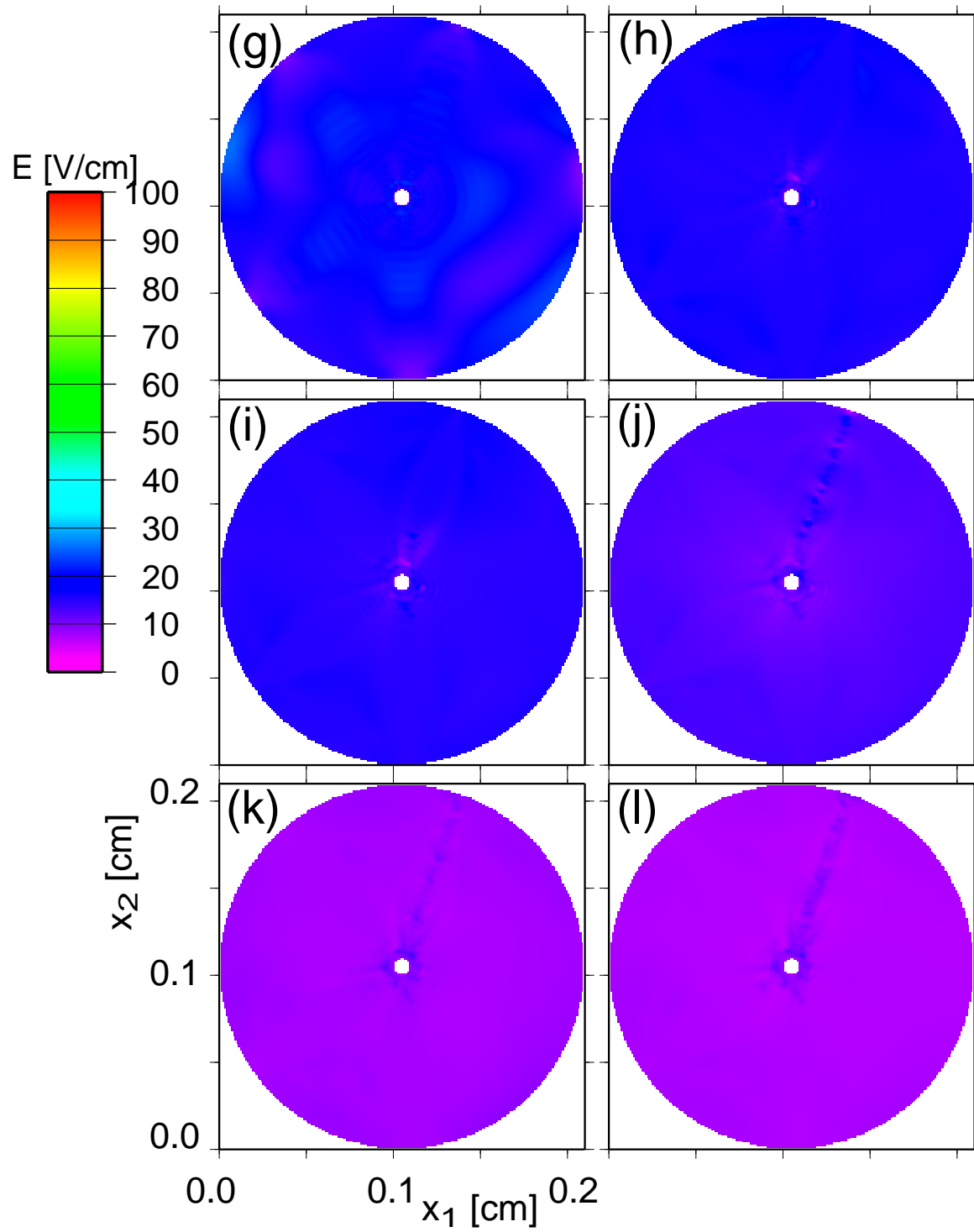


Figure 3.6: Calculated spatial profiles of the electric field \mathcal{E} corresponding to current density profiles of Fig. 3.3. (continued from previous page)

For the later detailed discussion of the propagation mechanism of the initial expanding front and the streamers (chapter 4) it is helpful to have a brief look at this point already at the spatial

profiles of the electric field corresponding to Figs. 3.3, 3.4 (a) – (l). They are plotted in Fig. 3.6. We see that the system starts from a radially symmetric distribution with the highest fields of up to 70 V/cm at the central contact (for a truly infinitely sharp rise of U_0 and vanishing current one would expect an initial field of even $\frac{U_0}{\ln(R_2/R_1)} \frac{1}{R_1} \approx 150$ V/cm at the inner contact; for a derivation of that expression see appendix D). With the expansion of the front the field just ahead of it assumes a constant value of approximately $\mathcal{E} = 40$ V/cm (Figs. 3.6 (b), (c)) which is also kept in the streamers' heads during their advance through the sample (Figs. 3.6 (d) – (f)). The most important feature to note however is the fact that the field behind the front and, to some lesser extend, later behind the streamers' heads is significantly lower than ahead of it, in contrast to what one might expect from the mere geometry. We thus conclude that the free electrons which have been generated through impact ionization in the high field region of the front or the streamers' heads lead to a screening of the electric field behind. This effect will turn out to be of importance to the propagation mechanism.

Next, we look at a simulation of the situation with reversed polarity, i. e. the central contact is now the anode. The spatial current, free electron density and electric field plots are found in Figs. 3.7, 3.8, and 3.9, respectively. The total current I as a function of time is plotted as the blue curve in Fig. 3.5. Starting again from an almost homogeneous, low conducting state (Figs. 3.7, 3.8 (a) at $t = 1$ ps) an impact ionization front starts to spread from the central contact (Figs. 3.7, 3.8 (b) at $t = 0.07$ ns) where the field is the highest due to the sample geometry (cf. the corresponding field profiles in Fig. 3.9). With roughly 10^8 cm/s the front velocity is about the same as in the previously discussed case of positive bias voltage. This is particularly noteworthy since here the movement of the front is opposite to the direction of the particle current. The electric field profile in Fig. 3.9 (c) ($t = 0.15$ ns) again shows a screening of the field behind the front. The field just ahead of the front is about 50 – 60 V/cm, which is higher than for positive U_0 .

For $t = 0.2$ ns (Figs. 3.7, 3.8 (d)) the front has become noticeably modulated. At $t = 0.4$ ns (Figs. 3.7, 3.8 (e)) those modulations have evolved into seven streamers. This time, the difference in expansion speed among the different streamers is much stronger than in the case of positive bias U_0 . The fastest streamer, which has developed from the most pronounced modulation, progresses at about $2 \cdot 10^8$ cm/s (Figs. 3.7, 3.8 (f) at $t = 0.6$ ns) and is even further accelerated shortly before reaching the outer contact (Figs. 3.7, 3.8 (g), $t = 0.64$ ns). The field ahead of the fast streamers is about 75 V/cm (Fig. 3.9 (f)) or even higher (Fig. 3.9 (g)). Within the fastest streamer, the free electron density is already above the threshold density $n_{th} = 5 \cdot 10^{14}$ cm $^{-3}$ before it reaches the outer electrode. Therefore, competition among the streamers via the external circuit is much fiercer than for positive U_0 . As soon as the first streamer has hit the cathode it “ignites” as an almost fully developed filament, skipping the pre-filamentary phase. This results in a much faster rise of the total current in Fig. 3.5 and consequently a more rapid drop of the sample voltage U . The other streamers do not even manage to reach the outer contact but instead decay on the time scale given by the recombination processes (Figs. 3.7, 3.8 (h), (i) at $t = 0.7$ ns, $t = 1.0$ ns, respectively). The final situation is again very similar to the positive bias case with a single current filament remaining (Fig. 3.7 (j), $t = 10$ ns).

In summary, we have seen in this chapter that the comparatively simple rate equation model for low temperature impact ionization combined with the classical semiconductor transport

equations is able to produce self-organized current filamentation in a Corbino sample in good agreement with the results of experimental measurements for such sample geometries. Here, effects of self-organization play an even more crucial role than for the nascence of a current filament between two point contacts [Gaa96d] where they only determine the shape of the filament and the distortion of the electric dipole field but where the position of the filament is fixed through the contacts.

For a Corbino sample in contrast, the nascence of a filament occurs through a symmetry breaking process: an impact ionization front forms at the central contact where the field is the highest due to the circular geometry, regardless of the polarity of the bias. That radially symmetric front expands in diameter with impact ionization creating free carriers that lead to a screening of the field behind the front. The circular front becomes unstable and breaks up into streamers which continue towards the outer electrode where they each form a pre-filament.

Further impact ionization leads to an increase in the free electron density within the pre-filaments and thus to a rise of the total current I through the sample. Due to the external load resistance, which via Kirchhoff's law (3.1) here acts as the global coupling mechanism, this is connected to a drop of the sample voltage U and thus of the electric field in each of the pre-filaments. As a result, the pre-filaments compete for voltage with each other. For the given parameters, only one of them, the one which had first reached the outer contact, prevails, while the others slowly decay. We can thus speak of a "winner takes all" dynamics.

With the obvious exceptions of the initial symmetry and the final competition between several pre-filaments this multi-stage formation process is very similar to the results obtained by Gae et al. for point-contact samples [Gaa96b, Gaa96c]. This becomes apparent, for example, by comparing the total current I over time t in Fig. 3.5 to the corresponding results in [Gaa96c]. For a sample whose two point contacts are much smaller than their distance l , as they are discussed there, this does not come too much of a surprise if one thinks of them as two adjacent Corbino disks with large outer radii $\frac{1}{2}l$ each (i. e. virtually plane outer contacts) and opposite polarity combined into a single sample.

The radial symmetry of the Corbino disks enables us to easily study the mechanism of the superfast impact ionization front which had not been identified in previous theoretical investigations of low temperature impact ionization in GaAs samples, although it is present in the initial stage of current filamentation in those other geometries, too. A more detailed analysis will be the subject of chapter 4.

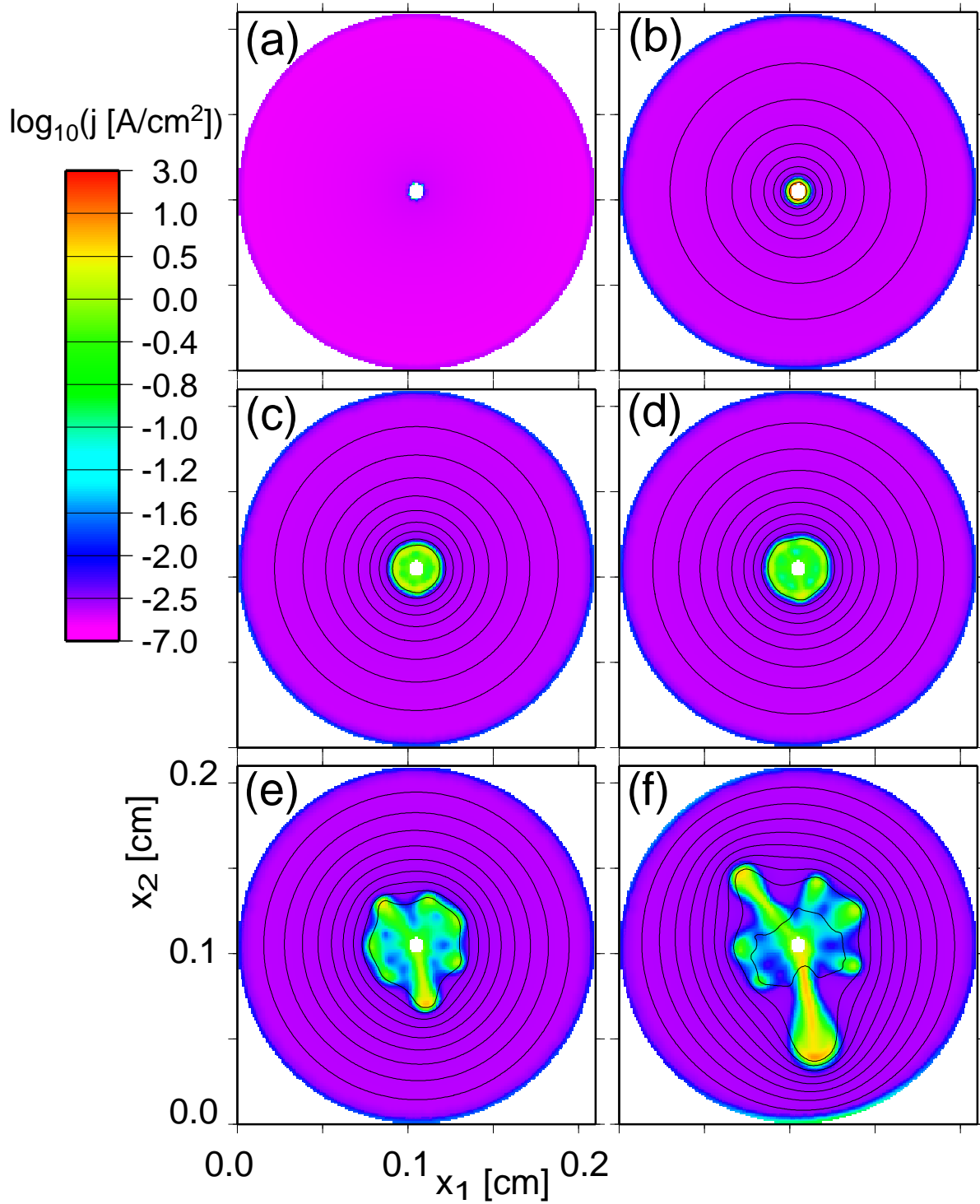


Figure 3.7: Simulation of the nascence of a current filament in an n-GaAs thin film Corbino disk sample with contacts radii $R_1 = 0.04$ mm, $R_2 = 1.05$ mm and an applied bias of $U_0 = -1.95$ V, i. e. the central electrode is the anode. In (a) – (j) the spatial distribution of the current density j is plotted for different times t : (a): $t = 1$ ps, (b): $t = 0.07$ ns, (c): $t = 0.15$ ns, (d): $t = 0.2$ ns, (e): $t = 0.4$ ns, (f): $t = 0.6$ ns. Equipotential lines are plotted spaced by 0.2 V. (continued on the next page)

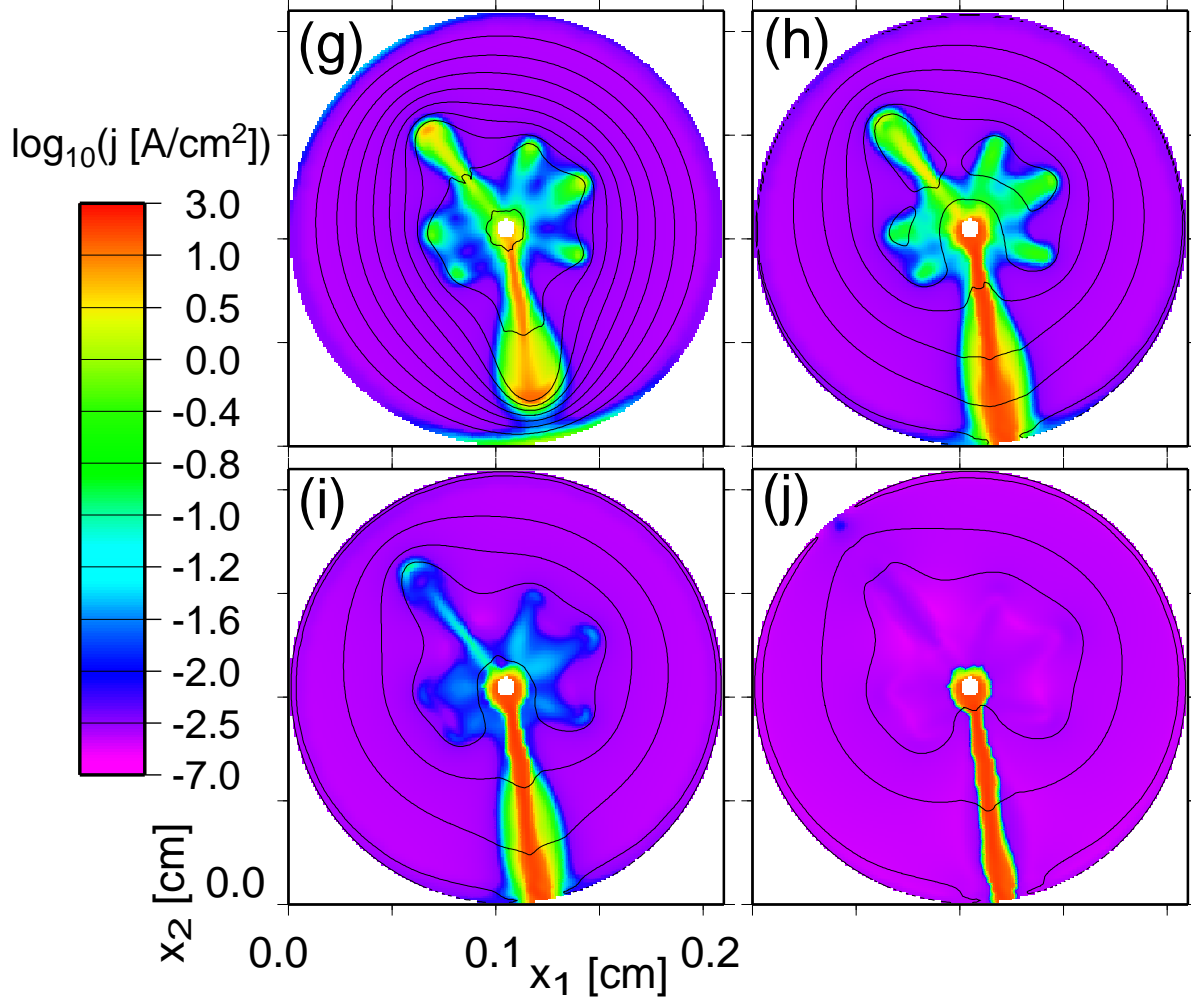


Figure 3.7: Simulation of the nascence of a current filament in an n-GaAs thin film Corbino disk sample with contacts radii $R_1 = 0.04$ mm, $R_2 = 1.05$ mm and an applied bias of $U_0 = -1.95$ V, i. e. the central electrode is the anode. In (a) – (j) the spatial distribution of the current density j is plotted for different times t : (g): $t = 0.64$ ns, (h): $t = 0.7$ ns, (i): $t = 1.0$ ns, (j): $t = 10.0$ ns. Equipotential lines are plotted spaced by 0.2 V. (continued from previous page)

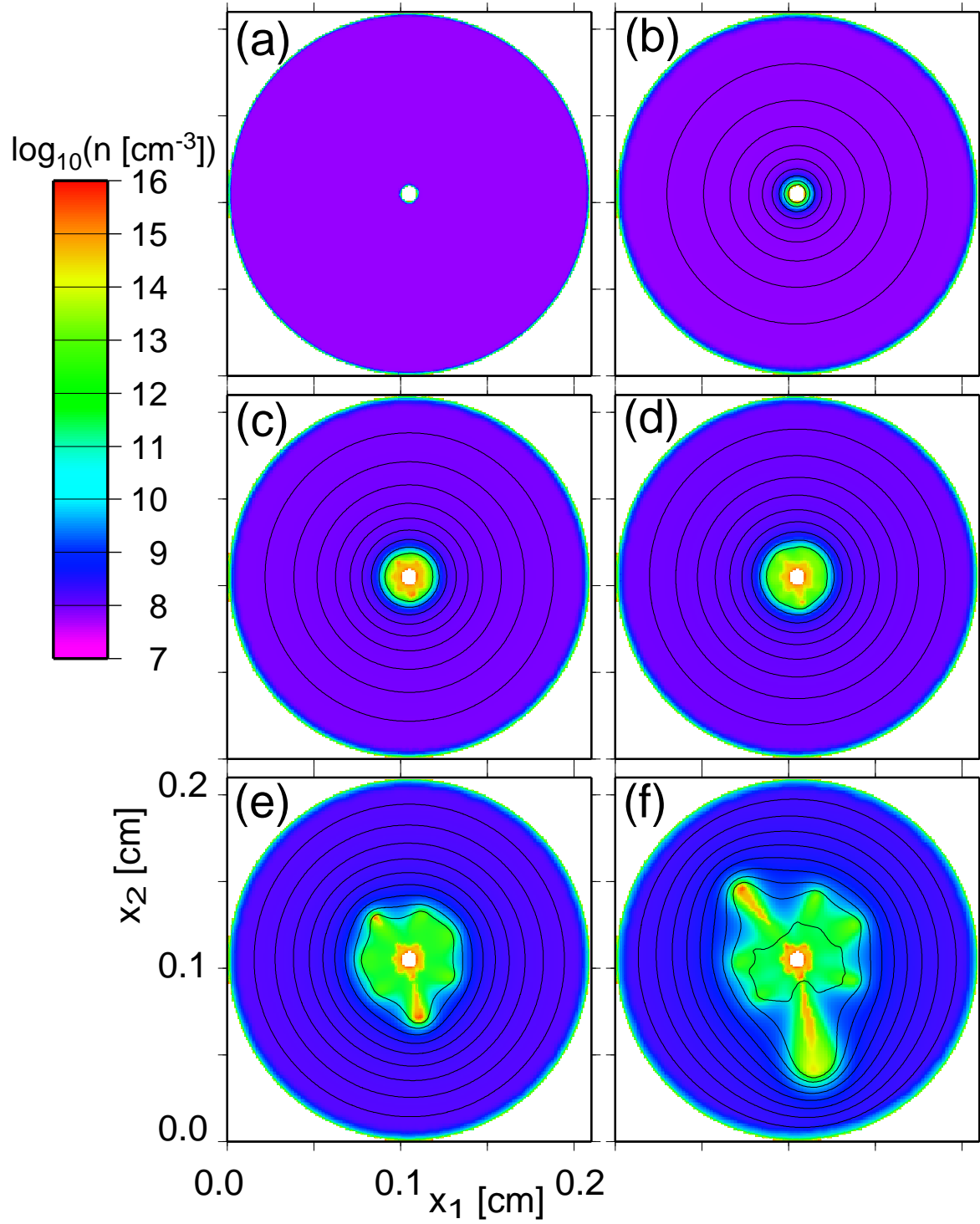


Figure 3.8: Calculated spatial profiles of the free electron distribution n and equipotential lines corresponding to the current density profiles of Fig. 3.7. (continued on the next page)

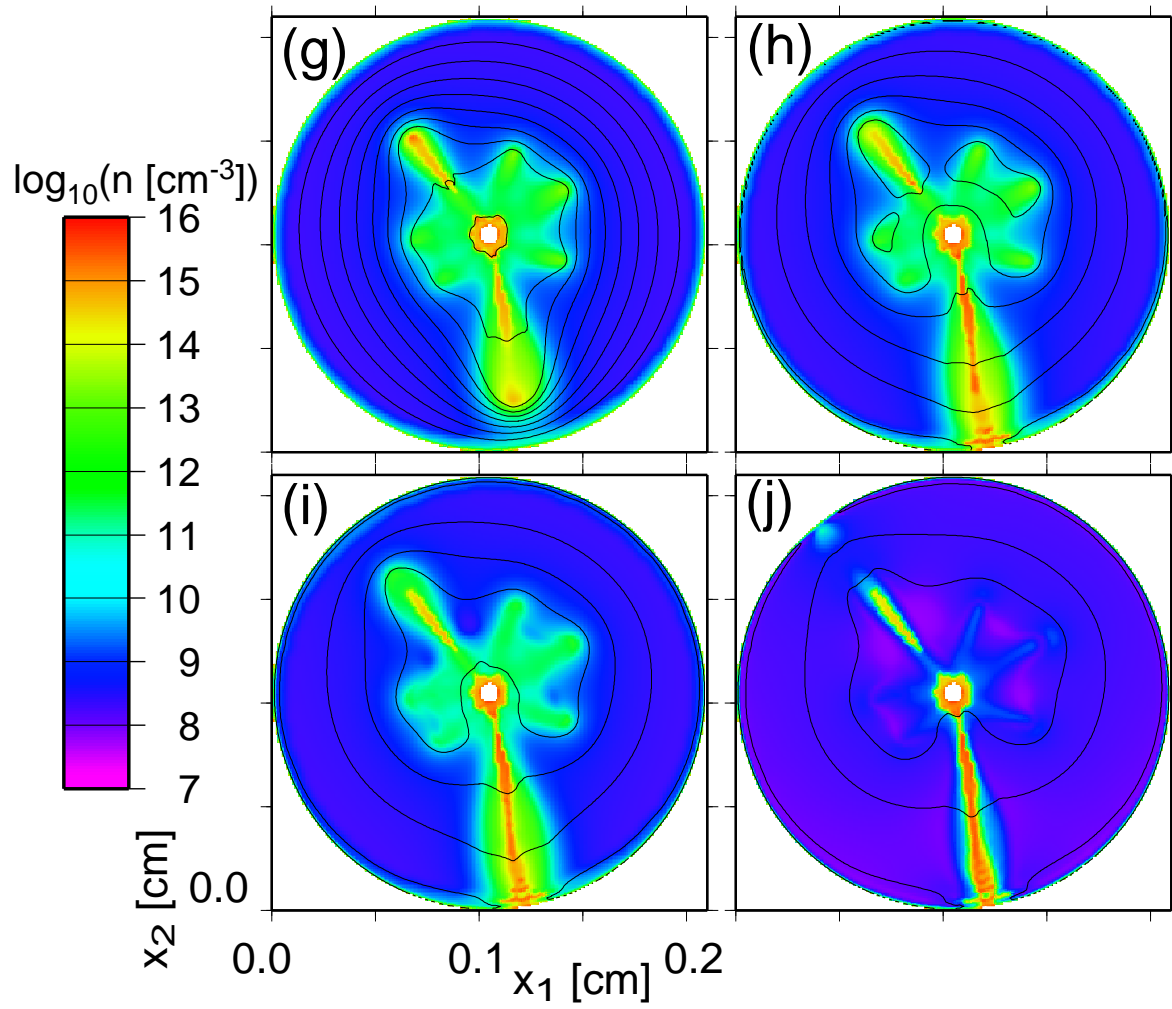


Figure 3.8: Calculated spatial profiles of the free electron distribution n and equipotential lines corresponding to the current density profiles of Fig. 3.7. (continued from previous page)

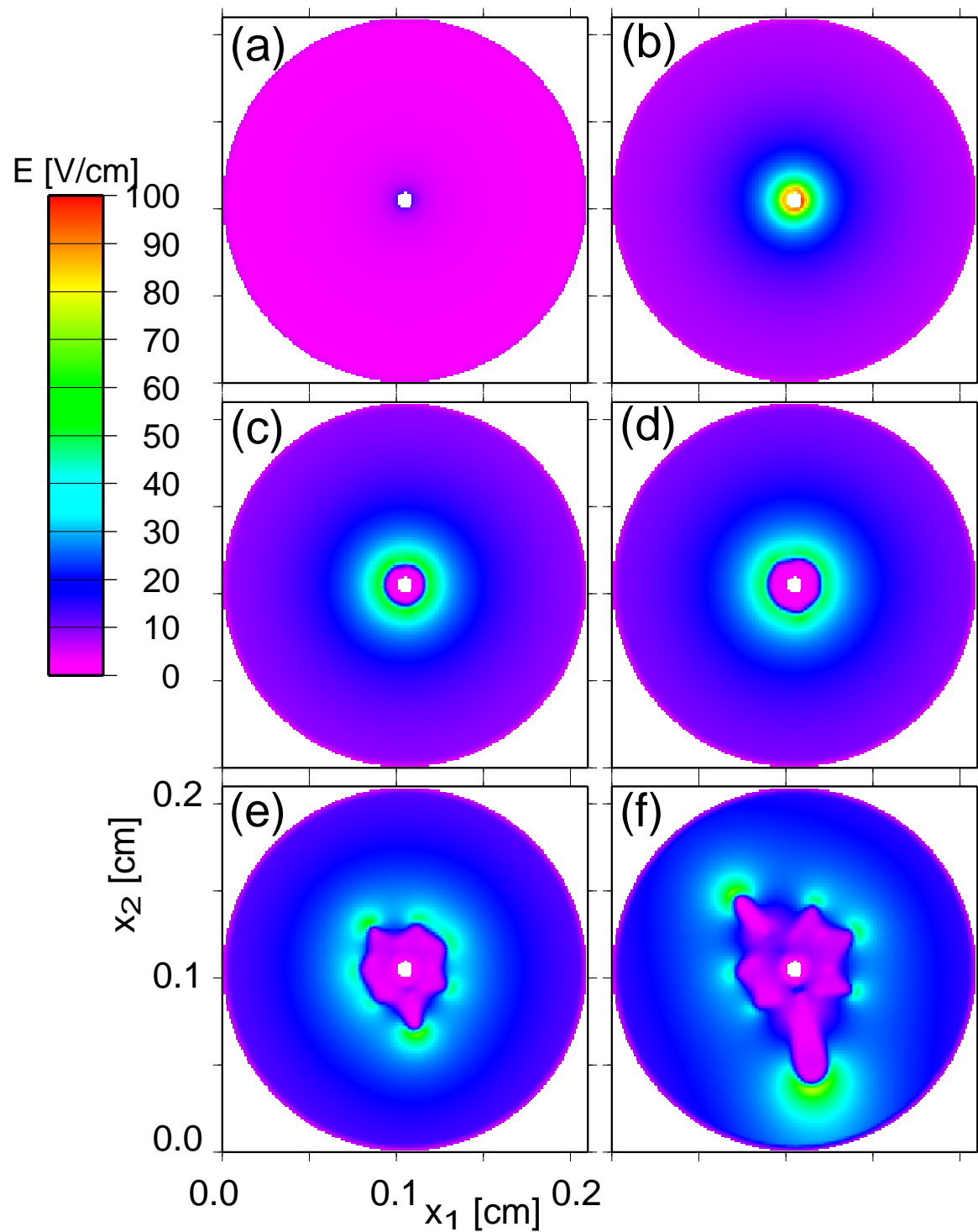


Figure 3.9: Calculated spatial profiles of the electric field E corresponding to current density profiles of Fig. 3.7. (continued on the next page)

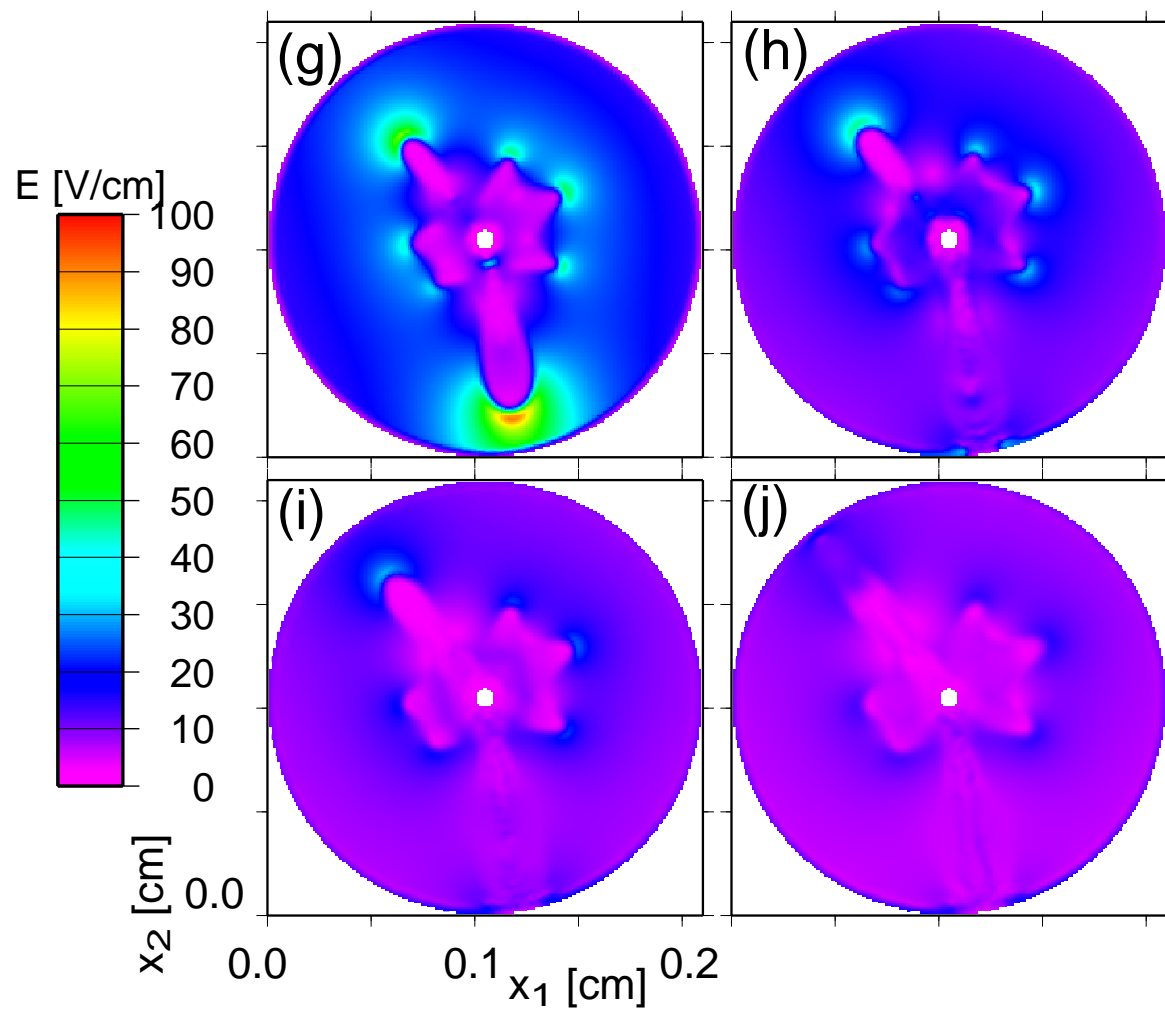


Figure 3.9: Calculated spatial profiles of the electric field E corresponding to current density profiles of Fig. 3.7. (continued from previous page)

Chapter 4

Fronts and streamers

We have seen in the previous chapter that current filamentation in a Corbino sample occurs as a multi-stage process: upon application of a bias voltage free carriers are generated starting around the central contact. That region of increased free electron density subsequently expands radially with a speed of about an order of magnitude faster than the drift velocity of a single electron. The expanding radial impact ionization front separating the high and the low conductivity regions acquires a growing transversal (azimuthal) modulation and breaks up into several finger-like streamers. Those streamers, upon reaching the outer contact, each constitute a pre-filament. In the final stage one of them emerges as a fully developed filament through a process of competition mediated by the external circuit, whereas the remaining pre-filaments decay.

In this chapter we will have a closer look at the mechanism of the superfast impact ionization front, motivating the term “streamer”. We will see that it is closely related to phenomena observed in other semiconductor structures and in gas discharges.

In Fig. 4.1 the radial distribution of both the free electron density n (green dots) and the electric field \mathcal{E} (red dots) in a Corbino disk of radii $R_1 = 0.25$ mm and $R_2 = 1.0$ mm are shown for different times t after application of a bias of $U_0 = 3.0$ V. It should be stressed that the distributions have been obtained by simply plotting each data point on the domain grid as a function of its distance r to the center of the Corbino sample, i. e. the spatial dependence on the azimuthal angle in polar coordinates has simply been dropped. Since there is no averaging involved a thin line represents a perfectly radially symmetric distribution, while a thicker line indicates a certain loss of radial symmetry of the developing pattern.

Starting from a low, virtually homogeneous distribution of about $n = 10^8$ cm⁻³ (Fig. 4.1 (a)) the free electron concentration sharply increases to somewhat above $n = 10^{12}$ cm⁻³ near the central contact ($r = 0.025$ cm) (Fig. 4.1 (b)). During the same interval of time, the electric field distribution \mathcal{E} , which in Fig. 4.1 is plotted on a linear scale ranging from 0 V/cm to 70 V/cm, rises from an almost vanishing profile for $t = 1$ ps (Fig. 4.1 (a))¹ to a monotonically decreasing field profile which is the highest at the central contact with about $\mathcal{E} = 70$ V/cm.

¹As we have seen in chapter 3 the reason for the vanishing sample voltage U at that stage inspite of the already fully present bias U_0 is the high initial current I .

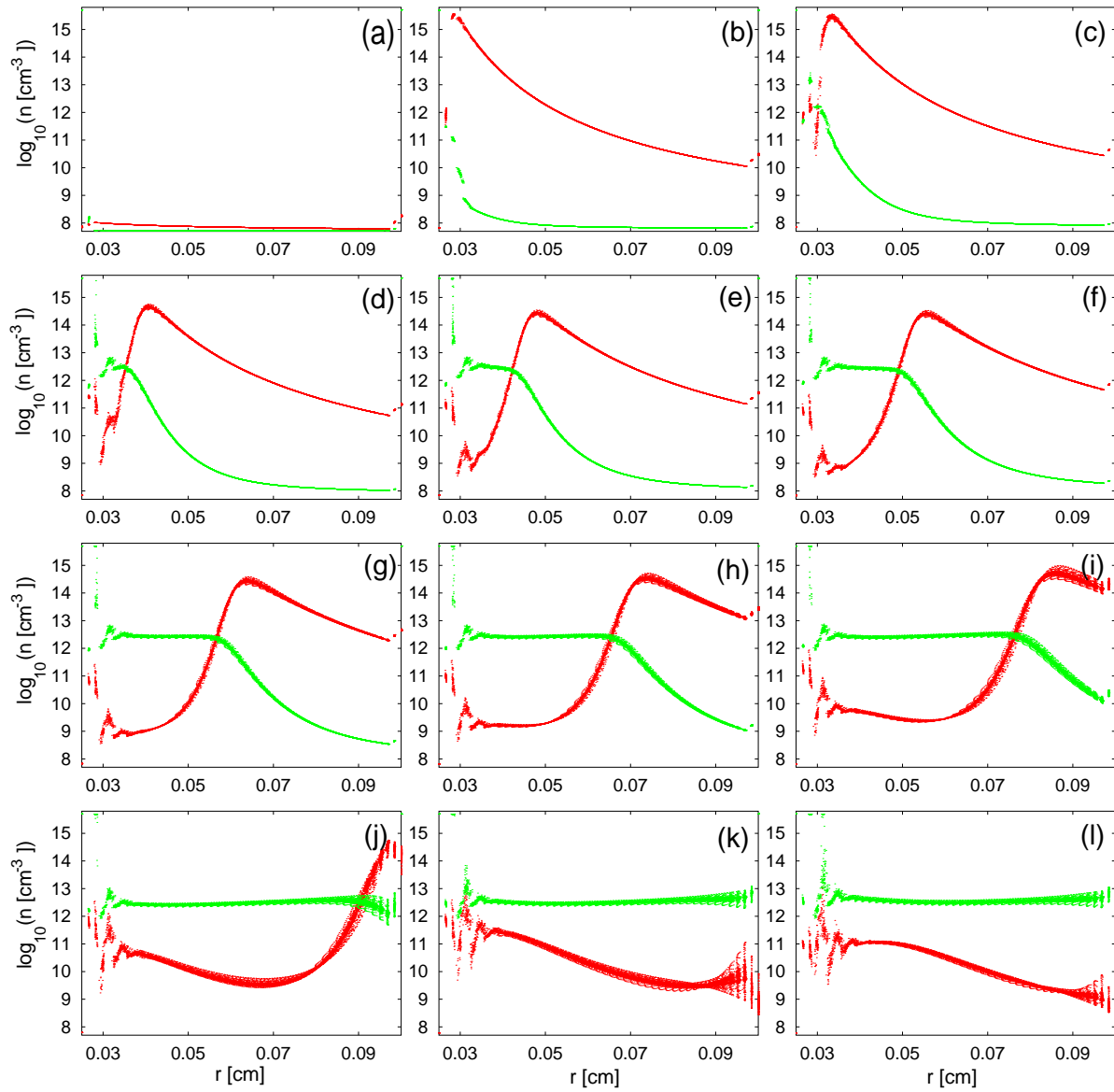


Figure 4.1: Radial distribution of the free electron density n (green dots; logarithmic scale) in a Corbino sample with radii $R_1 = 0.25$ mm, $R_2 = 1.0$ mm and an applied voltage of $U_0 = 3.0$ V at different times t . Red dots: linear plot of the radial distribution of the electric field \mathcal{E} (lower bound $\mathcal{E} = 0$ V/cm, upper bound $\mathcal{E} = 70$ V/cm). (a): $t = 1$ ps, (b): $t = 0.03$ ns, (c): $t = 0.06$ ns, (d): $t = 0.09$ ns, (e): $t = 0.12$ ns, (f): $t = 0.15$ ns, (g): $t = 0.18$ ns, (h): $t = 0.21$ ns, (i): $t = 0.24$ ns, (j): $t = 0.27$ ns, (k): $t = 0.30$ ns, (l): $t = 0.33$ ns.

In Fig. 4.1 (c) ($t = 0.06$ ns) one can see that the electric field profile has “decoupled” from the central contact, and its peak value has shifted towards larger r . The free electron distribution profile has become less steep, i. e. n has been rising monotonically in the region next to the central contact. This motion continues with time (Figs. 4.1 (d) – (i)). The peak of the electric field distribution progresses towards the outer contact, leaving behind a region with very low

field. Apart from this translation in space the overall field profile remains quite unchanged. The free electron distribution n also forms a rigidly moving front which follows the peak field with some small lag. Behind the front, where \mathcal{E} is very low, n attains a spatially constant value of some 10^{12} cm^{-3} . The radial velocity of the fronts is almost $3 \cdot 10^8 \text{ cm/s}$, which is, as already seen in the previous chapter, over one order of magnitude higher than the electron drift velocity of $7 \cdot 10^6 \text{ cm/s}$ taken at the peak field.

Once the fronts have reached the outer electrode (Fig. 4.1 (j)) we get an almost homogeneous free electron distribution again, albeit with a free electron density that corresponds to that of a pre-filament and is thus more than four orders of magnitude higher than that of the initial state. The electric field profile again assumes a monotonically decreasing shape (Fig. 4.1 (k)). Both profiles at the contacts already exhibit clear signs of loss of radial symmetry, indicating the beginning formation of the pre-filamentary state (Fig. 4.1 (l)).

Additional insight into the process of front expansion can be gained from the spatial profiles of the charge density ρ as well as the trapped electron densities n_1 and n_2 . In Fig. 4.2 the corresponding charge density profiles are plotted in units of the elementary charge e . A logarithmic scale is used for both positive and negative values. This makes it necessary to set to zero any values $-1 \text{ cm}^{-3} \leq \rho/e \leq 1 \text{ cm}^{-3}$. The values have been smoothened by averaging across small intervals Δr since the original data contains both positive and negative values on small spatial scales as a result of the numerical algorithm used in TeSCA.

We start with a slightly negative charge distribution, which is homogeneous except near the contacts (as a result of the boundary conditions) (Fig. 4.2 (a)). In Fig. 4.2 (b) a positive charge accumulation above that background forms near the central contact. That peak further increases and travels through the sample with the peak of the electric field (cf. Fig. 4.1). Thus the localized space charge indicates the momentary front position in Figs. 4.2 (c) – (i).

In Fig. 4.3 profiles of the three electron densities n , n_1 and n_2 are shown on a logarithmic scale. Initially (Fig. 4.3 (a)), we have a homogeneous spatial distribution: almost all electrons are trapped in the donor ground level, i. e. n_1 is almost identical to the effective doping density $N_D^* = 5 \cdot 10^{15} \text{ cm}^{-3}$. n_2 is about $1/10000$ of that value, and n is again more than three orders of magnitude smaller than n_2 , i. e. there are virtually no free electrons. That distribution approximately corresponds to the homogeneous equilibrium (i. e. $U = 0$) state that can be calculated analytically (cf. appendix C)². As already discussed in Fig. 4.1 the free electron density builds up near the cathode, and subsequently that region of higher free carrier density expands radially towards the anode. We read off from Fig. 4.3 that both n_1 and n_2 in contrast stay largely constant in time and homogeneous across the sample radius, again with the exception of the contact regions.

From those results we can give an explanation for the mechanism of front propagation. Upon application of the external bias to the contacts a monotonically decreasing radial field distribution builds up as a result of the circular geometry of the sample. Due to the minor homogeneous negative background charge density (cf. Fig. 4.2) that field distribution does not exactly

²The steady state values for the case $\mathcal{E} = 0$ are $n = 1.1 \cdot 10^{-8} N_D^* = 5.4 \cdot 10^7 \text{ cm}^{-3}$, $n_2 = 8.2 \cdot 10^{-5} N_D^* = 4.1 \cdot 10^{11} \text{ cm}^{-3}$ and $n_1 = N_D^* - n - n_2 \approx N_D^* = 5 \cdot 10^{15} \text{ cm}^{-3}$

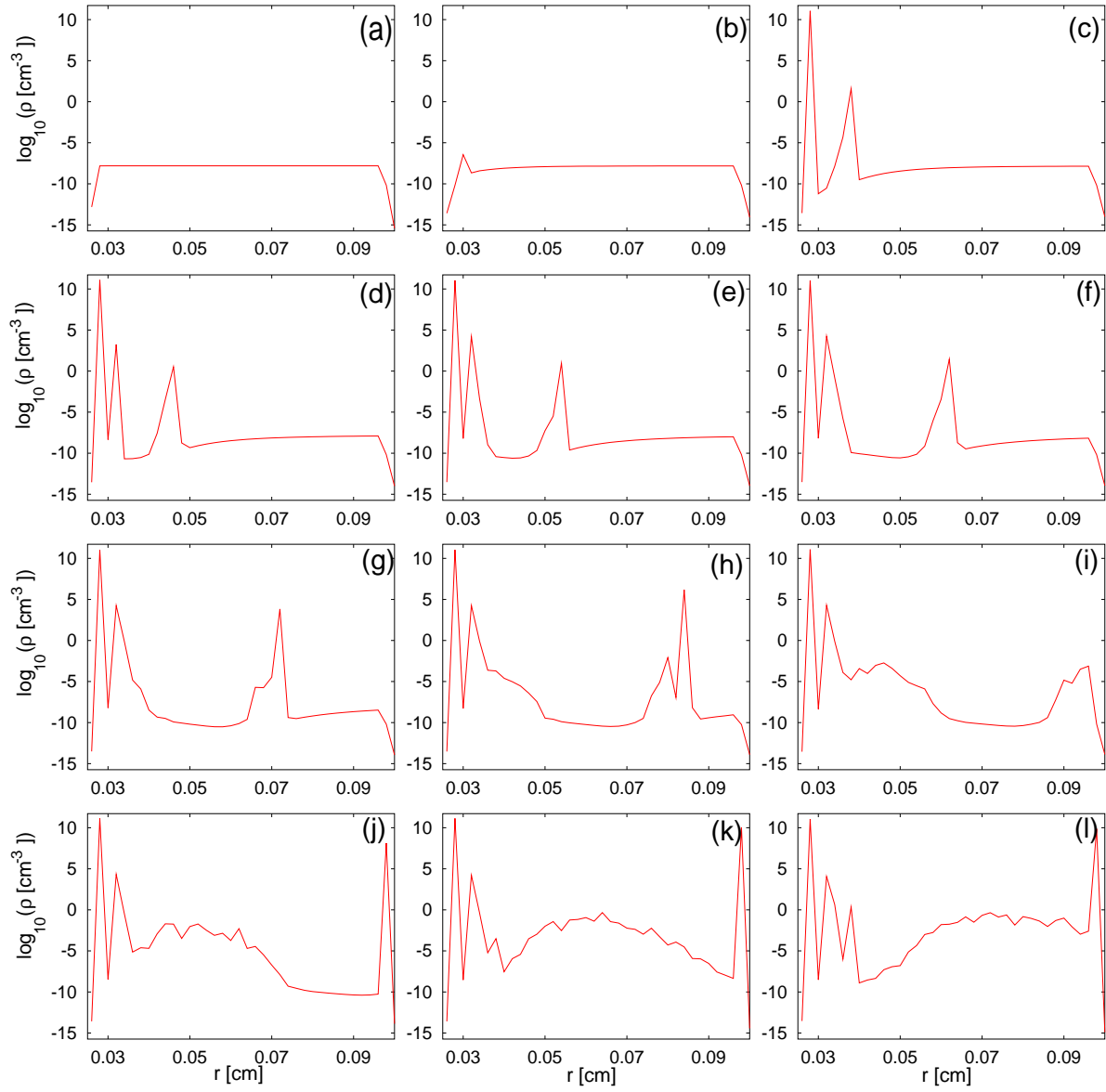


Figure 4.2: Radial distribution of the charge density ρ (divided by the elementary charge e) on a logarithmic scale for both positive and negative values (values of $|\rho/e| < 1 \text{ cm}^{-3}$ are set to zero) in a Corbino sample with radii $R_1 = 0.25 \text{ mm}$, $R_2 = 1.0 \text{ mm}$ and an applied voltage of $U_0 = 3.0 \text{ V}$ corresponding to Fig. 4.1.

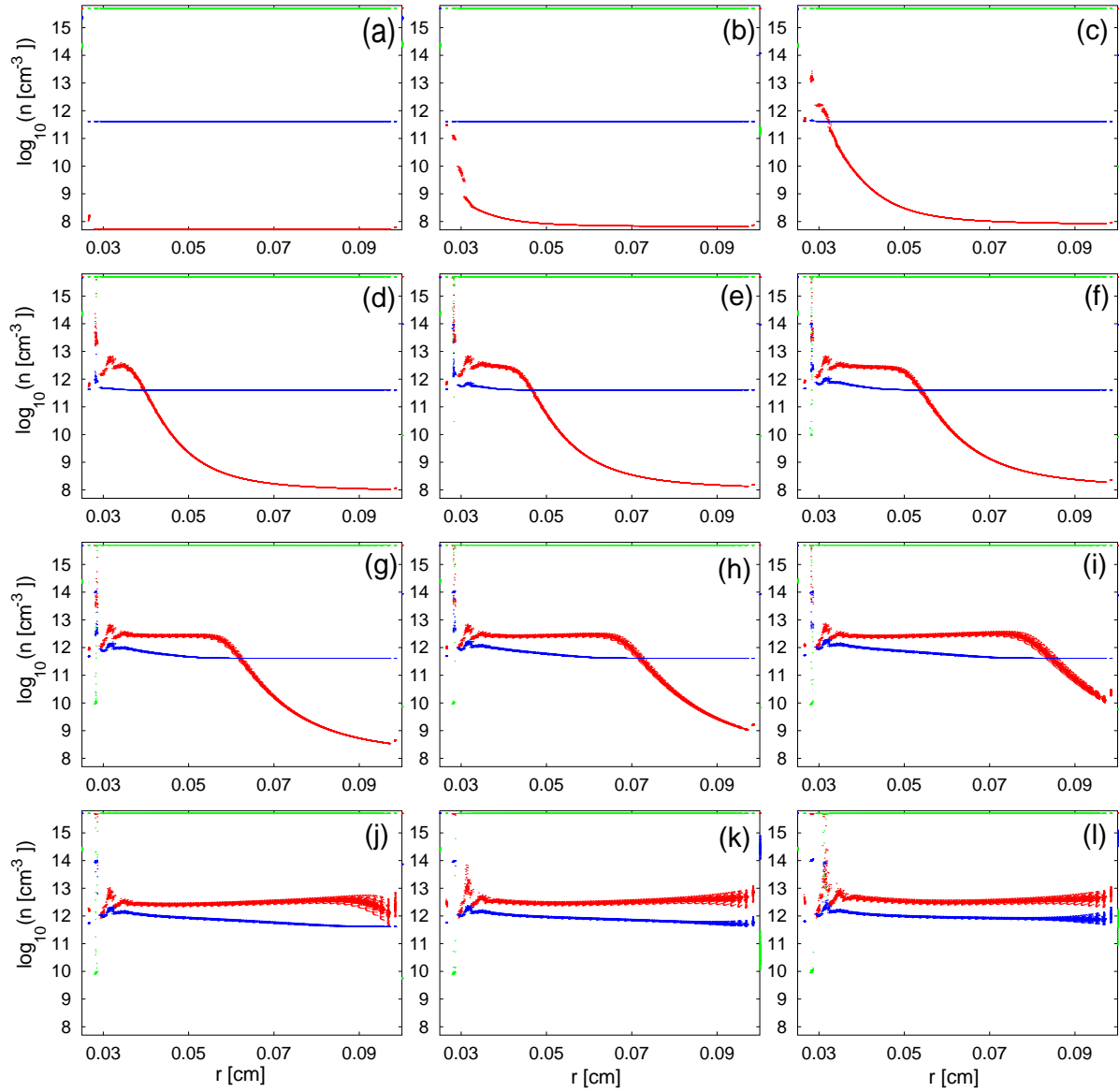


Figure 4.3: Radial distribution of the free electron density n (red dots), donor ground state and excited state, n_1 (green dots; located just below the upper bound) and n_2 (blue dots), respectively, in a Corbino sample with radii $R_1 = 0.25$ mm, $R_2 = 1.0$ mm and an applied voltage of $U_0 = 3.0$ V corresponding to Fig. 4.1.

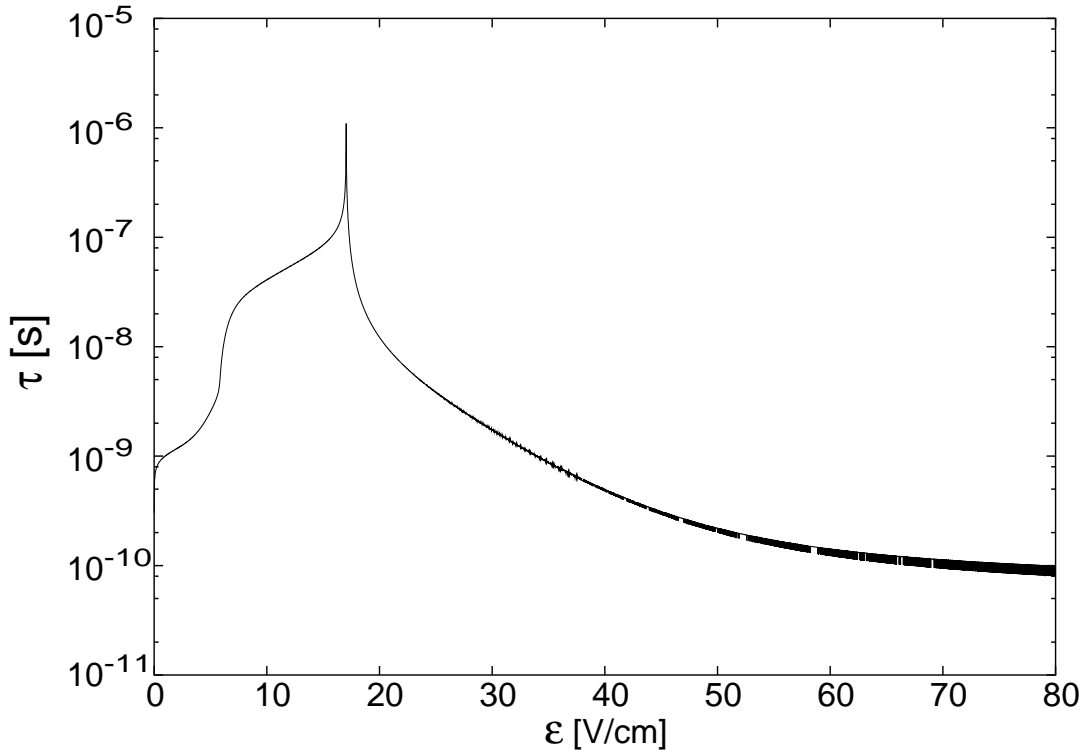


Figure 4.4: Rise time τ of the free electron density from the equilibrium state as a function of the electric field \mathcal{E} . The values have been calculated numerically for the generation-recombination coefficients of appendix B.

decrease with $1/r$ as it would in plane polar coordinates for an electrically neutral system, but the profile is still close to that dependence.

To understand the further process, it is necessary to take a look at the dynamics of the generation-recombination processes. In Fig. 4.4 the time τ it takes the free electron density n to grow by the fraction $1/e$ of the difference between the equilibrium value and the respective steady state value has been plotted as a function of the electric field \mathcal{E} . To obtain that rise time τ for a given value of \mathcal{E} first the corresponding steady state value of the free electron density, $n^f(\mathcal{E})$ has been calculated by numerically solving the local generation-recombination kinetics (i. e. using eqs. (2.1), (2.2) and setting the current density to zero) using a simple Euler scheme and starting with the equilibrium electron concentrations as the initial values n^i, n_1^i, n_2^i . $n^f(\mathcal{E})$ is then the value of n the system converges to. In a second calculation the local dynamics is again solved numerically until n reaches $n^i + \exp(-1)(n^f - n^i)$. τ is then the time it took the system to reach that point.

We see that τ goes to infinity for $\mathcal{E} = \mathcal{E}_{th} = 17 \cdot \text{V/cm}$ and monotonically decreases for higher values of the electric field. This numerical result agrees with the general theoretical considerations by SCHÖLL for the threshold switching delay time τ_d which predict τ_d to be proportional

to $1/(\exp(\Delta\mathcal{E}) - 1)$, where $\Delta\mathcal{E} = \mathcal{E} - \mathcal{E}_{th}$ is the field corresponding to the so-called *overvoltage*. (cf. chapter 2.2 of Ref. [Sch87]). As a result we see that it takes the local electric field \mathcal{E} to be at least somewhat above the threshold value in order for the system to reach the upper branch of the stable current-density field characteristic within a finite time, and the higher the field is, the faster that process works.

Getting back to the initial monotonically decreasing electric field profile, we conclude from those considerations that the rise of n is the fastest where \mathcal{E} is the highest, i. e. right at the central contact. The developing rigid spatial profile of n is a consequence of the monotonically decreasing rise time τ with increasing $\Delta\mathcal{E} = \mathcal{E} - \mathcal{E}_{th}$. Even though the electric field is above \mathcal{E}_{th} across the entire sample only near its peak is \mathcal{E} high enough to lead to a sufficiently fast rise of n . This means that a considerable amount of free carriers is created only around the peak of \mathcal{E} . Now those newly created free carriers give rise to an effective screening of the electric field, as can be seen in Fig. 4.1. That latter process is governed by the Maxwellian relaxation time $\tau_M = \varepsilon/(en\mu)$ which here is of the order of 10^{-11} s.

A screening of the electric field in one part of the sample in turn means that the voltage U must drop almost entirely across the remaining part, i. e. the region ahead of the front. Since that region gets smaller the further the front expands towards the outer contact the local field in every point of that latter region rises (assuming the overall current I and thus the voltage drop across the load resistance does not change significantly), enabling a faster local increase of n . This is a purely geometrical effect which relies on the finite size of the sample. That way the electric field front can traverse across the entire sample from the inner to the outer electrode with the free electron front following it slightly behind. That mechanism of front propagation does not involve an individual electron traversing the sample making it possible to obtain a front velocity faster than the single carrier drift velocity, i. e. a *superfast* front.

It should be noted that for the mechanism of the moving impact ionization front, which is an inherently transient process, the S-shape of the local stationary current-density field relation does not play a role.

This mechanism of front propagation is remarkably similar to the one found for TRAPATT (*TRApped Plasma Avalange Triggered Transit*, cf. [Del70]) like fronts in high-voltage Silicon sharpening diodes [Min94, Min97b, Min97a, Min00, Foc97]. In those $p^+ - n - n^+$ structures there exists a constant background charge due to the doping, which in a rectangular geometry leads to a spatial field gradient. The theory now assumes that impact ionization sets in instantaneously as soon as the local field is above a threshold field \mathcal{E}_a . For an appropriate sample voltage this condition is met initially only within a small active zone near the $p^+ - n$ junction. The free carriers created by impact ionization lead to a screening of the electric field, which causes the total voltage to drop across a smaller part of the sample, increasing the electric field in that remaining part and shifting the interface given by the threshold field \mathcal{E}_a further into the previously non-active region.

In that model it is important that there exist already free carriers in the non-active region, i. e. the system exhibits some degree of pre-ionization. If that was not the case, impact ionization, which is proportional to the free electron concentration, could only set in once carriers from the adjacent active region have penetrated. The impact ionization front thus could progress only

with the drift velocity of the carriers, and one would not obtain a superfast impact ionization front.

The essential mechanism of front propagation in those structures is the same as in doped GaAs Corbino disks: an inhomogeneous, monotonically decreasing field profile causes impact ionization only within a portion of the sample. Screening of the electric field due to newly created free carriers effectively reduces the length of the sample across which the voltage drops, leading to an increase of the local electric field in that remaining area and thus encouraging impact ionization and further screening in more and more of the sample area. Thus in both cases the mechanism is an effect of the finite size (length or radius, respectively) of the sample.

The two semiconductor systems differ in the mechanism responsible for the essential initial spatially monotonically decreasing electric field distribution: in the Corbino disk it is the radial geometry, while in the Silicon $p^+ - n - n^+$ diode it is the charge of the naked donors in the n-base. Another difference in both models is that for the latter one impact ionization is assumed to set in instantaneously once a threshold field \mathcal{E}_a has been reached, while for low temperature impact ionization in GaAs we have seen that the field must be sufficiently above \mathcal{E}_{th} to produce enough free carriers for an effective screening. The latter fact is the reason why in the n-GaAs Corbino samples the front has an electric field that lies considerably above the threshold field \mathcal{E}_{th} . It is in particular that latter difference between the two systems that makes the description of the front dynamics for n-GaAs considerably more complicated.

We have seen in Fig. 4.3 that the trapped electron concentration in the excited donor level, n_2 , remains quite constant in both space and time while the ionization front traverses the sample. This allows a further simplification of our model by eliminating that variable: eq. (2.4) then reduces to

$$\phi \approx \left(-T_1^S (N_D - N_D^* - n_2) + X_1 N_D^* + X_1^* n_2 \right) n + X_1^S n_2. \quad (4.1)$$

Here we have made use of the additional result of the simulations that the electron concentration in the donor ground state, n_1 , is approximately N_D^* . In (4.1) the first term, in particular the impact ionization X_1 is dominating, and the term $X_1^S n_2$ can be neglected. Since the free electron density n is still much lower than $n_{th} = 0.1 N_D^* T_1^S$, X_1 and X_1^* are functions of \mathcal{E} only.

We can thus rewrite eq. (4.1) as $\phi \approx \alpha(\mathcal{E})n$ with a field-dependent ionization coefficient α . With eqs. (2.1), (2.2), (2.10) and $\phi_1 = -\phi$ we arrive at a system of equations that is formally identical to the standard streamer model for ionization in gases [Vit94, Saa98]:

$$\dot{n} + \underline{\nabla} \cdot \underline{j} = \alpha(\mathcal{E})n \quad (4.2)$$

$$\dot{n}_1 = -\alpha(\mathcal{E})n \quad (4.3)$$

$$\epsilon \underline{\nabla} \cdot \underline{\mathcal{E}} = \rho = e((N_D^* - n_2) - n_1 - n) \quad (4.4)$$

with \underline{j} being the sum of the drift and the diffusion current density as in eq. (2.8). In eq. (4.3) n_1 takes the role of the heavier ions in the gas which are assumed to be immobile. We have thus demonstrated that our model for n-doped GaAs at low temperatures for the case of the

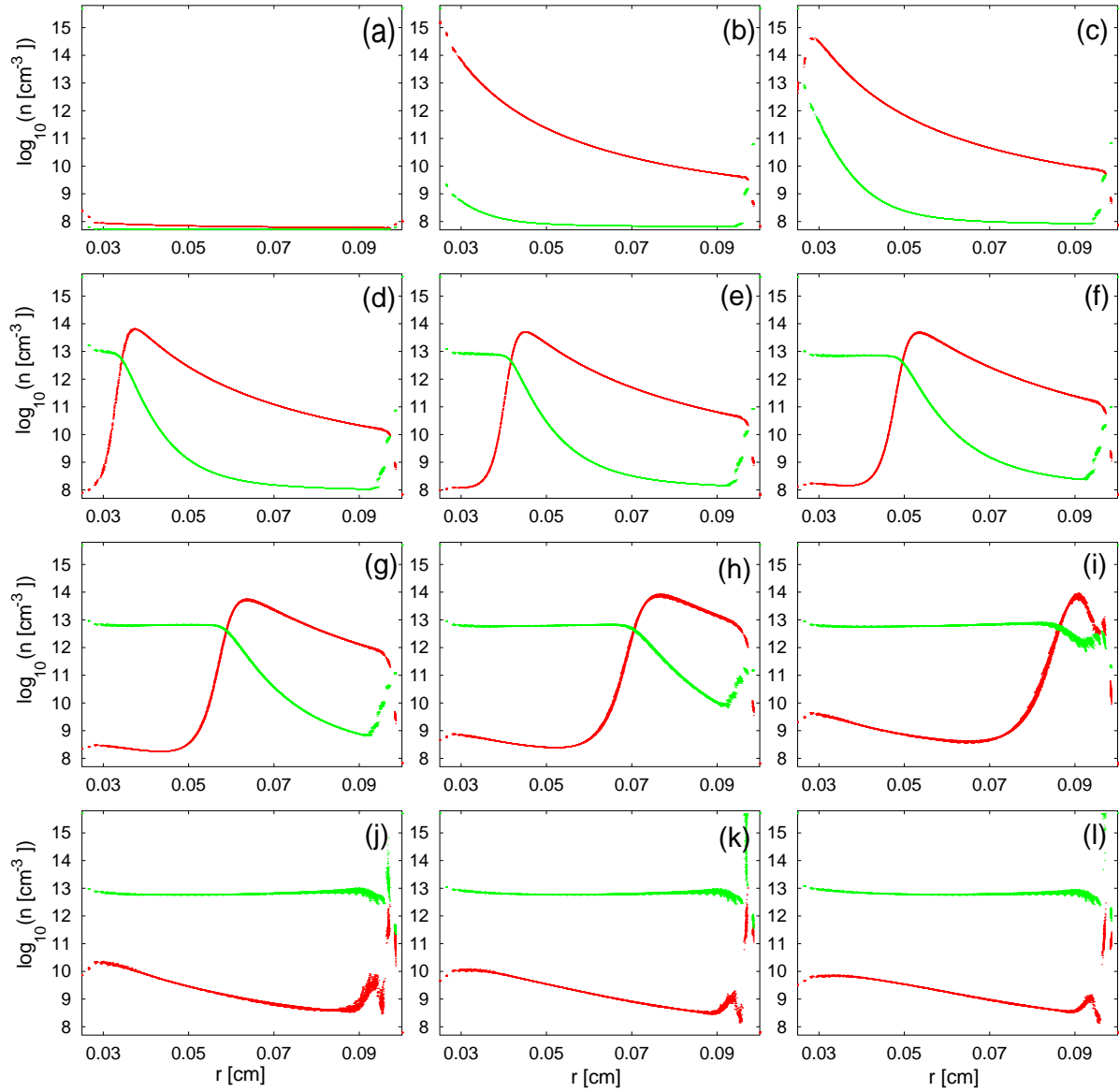


Figure 4.5: Radial distribution of the free electron density n (green dots; logarithmic scale) in a Corbino sample with radii $R_1 = 0.25$ mm, $R_2 = 1.0$ mm and an applied voltage of $U_0 = -3.0$ V at different times t . Red dots: linear plot of the radial distribution of the electric field \mathcal{E} (lower bound $\mathcal{E} = 0$ V/cm, upper bound $\mathcal{E} = 85$ V/cm). (a): $t = 1$ ps, (b): $t = 0.03$ ns, (c): $t = 0.06$ ns, (d): $t = 0.09$ ns, (e): $t = 0.12$ ns, (f): $t = 0.15$ ns, (g): $t = 0.18$ ns, (h): $t = 0.21$ ns, (i): $t = 0.24$ ns, (j): $t = 0.27$ ns, (k): $t = 0.30$ ns, (l): $t = 0.33$ ns.

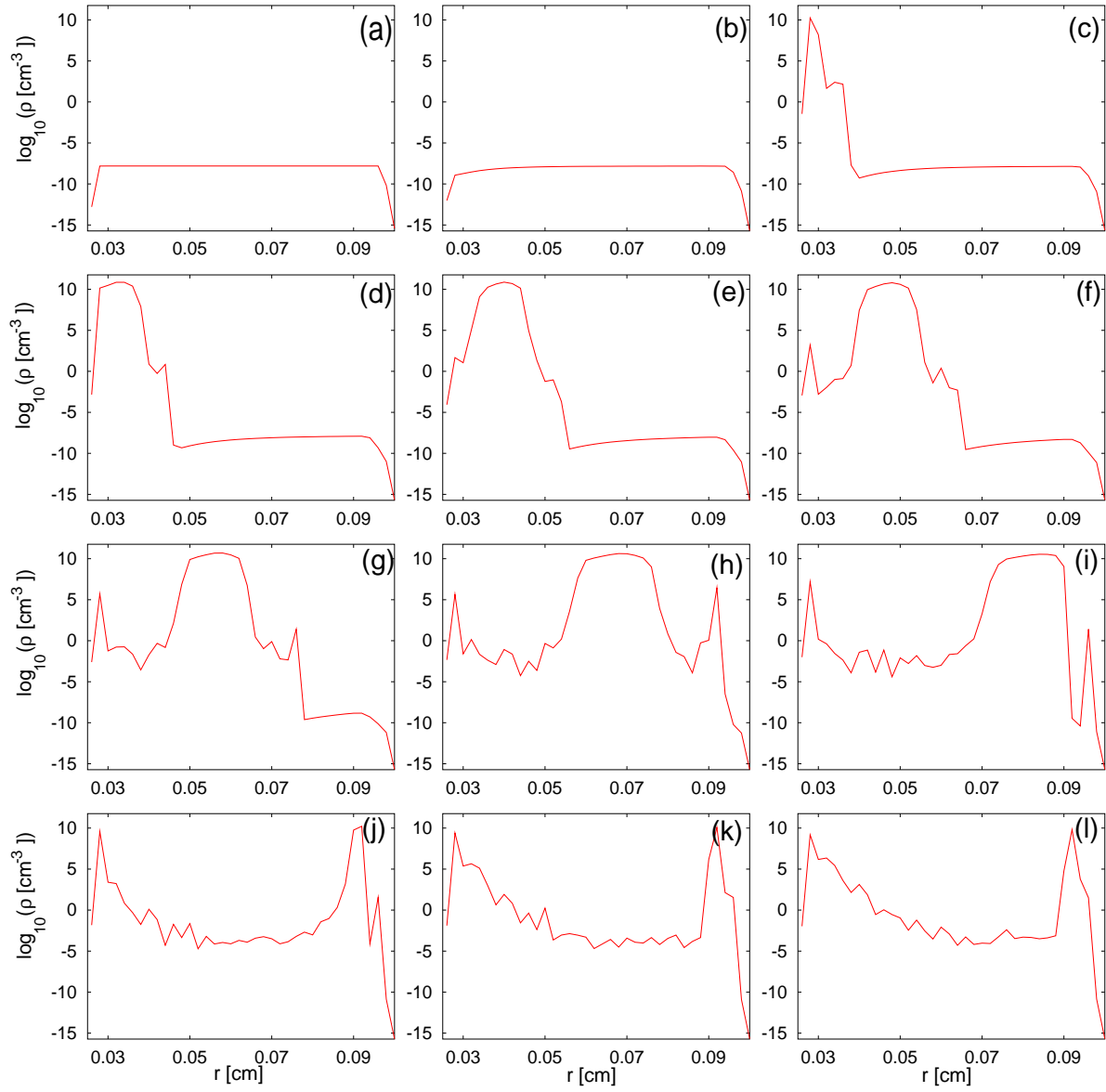


Figure 4.6: Radial distribution of the charge density ρ (divided by the elementary charge e) on a logarithmic scale for both positive and negative values (values of $|\rho/e| < 1 \text{ cm}^{-3}$ are set to zero) in a Corbino sample with radii $R_1 = 0.25 \text{ mm}$, $R_2 = 1.0 \text{ mm}$ and an applied voltage of $U_0 = -3.0 \text{ V}$ corresponding to Fig. 4.5.

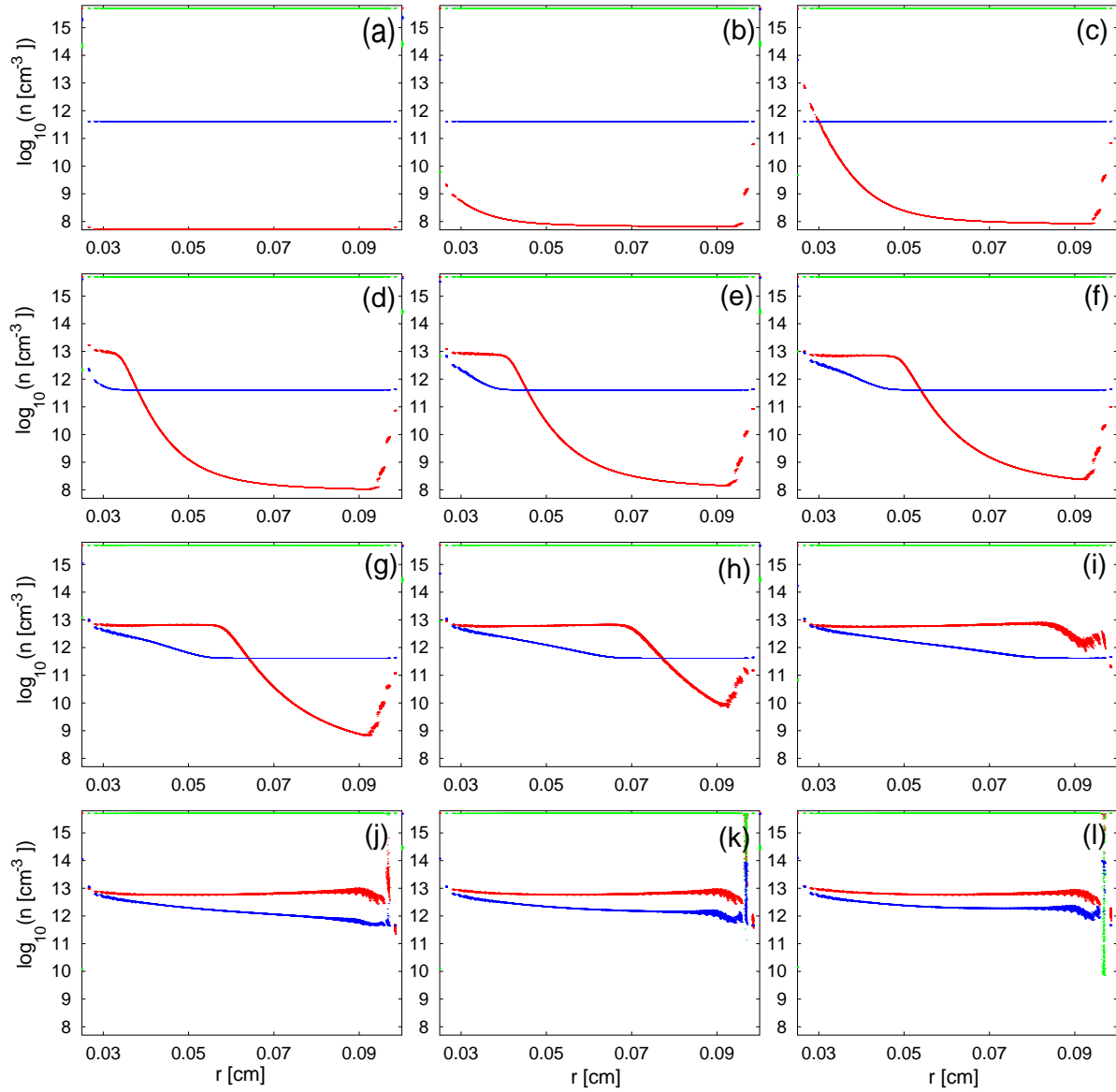


Figure 4.7: Radial distribution of the free electron density n (red dots), donor ground state and excited state, n_1 (green dots; located just below the upper bound) and n_2 (blue dots), respectively, in a Corbino sample with radii $R_1 = 0.25$ mm, $R_2 = 1.0$ mm and an applied voltage of $U_0 = -3.0$ V corresponding to Fig. 4.5.

propagating impact ionization front can be reduced to the model used to describe streamer formation in gases, with a different specific impact ionization coefficient $\alpha(\mathcal{E})$ though.

Figs. 4.5, 4.6, 4.7 are equivalent to Figs. 4.1, 4.2, 4.3 except that the polarity of the external bias has been reversed ($U_0 = -3.0$ V), i. e. the central contact is now the anode. We see a similar behavior as in the previous case of positive polarity with the charge density peak connected to the front being much more pronounced (Fig. 4.6). That similarity for reversed bias is to be expected from the mechanism of front propagation described above since the expansion of the

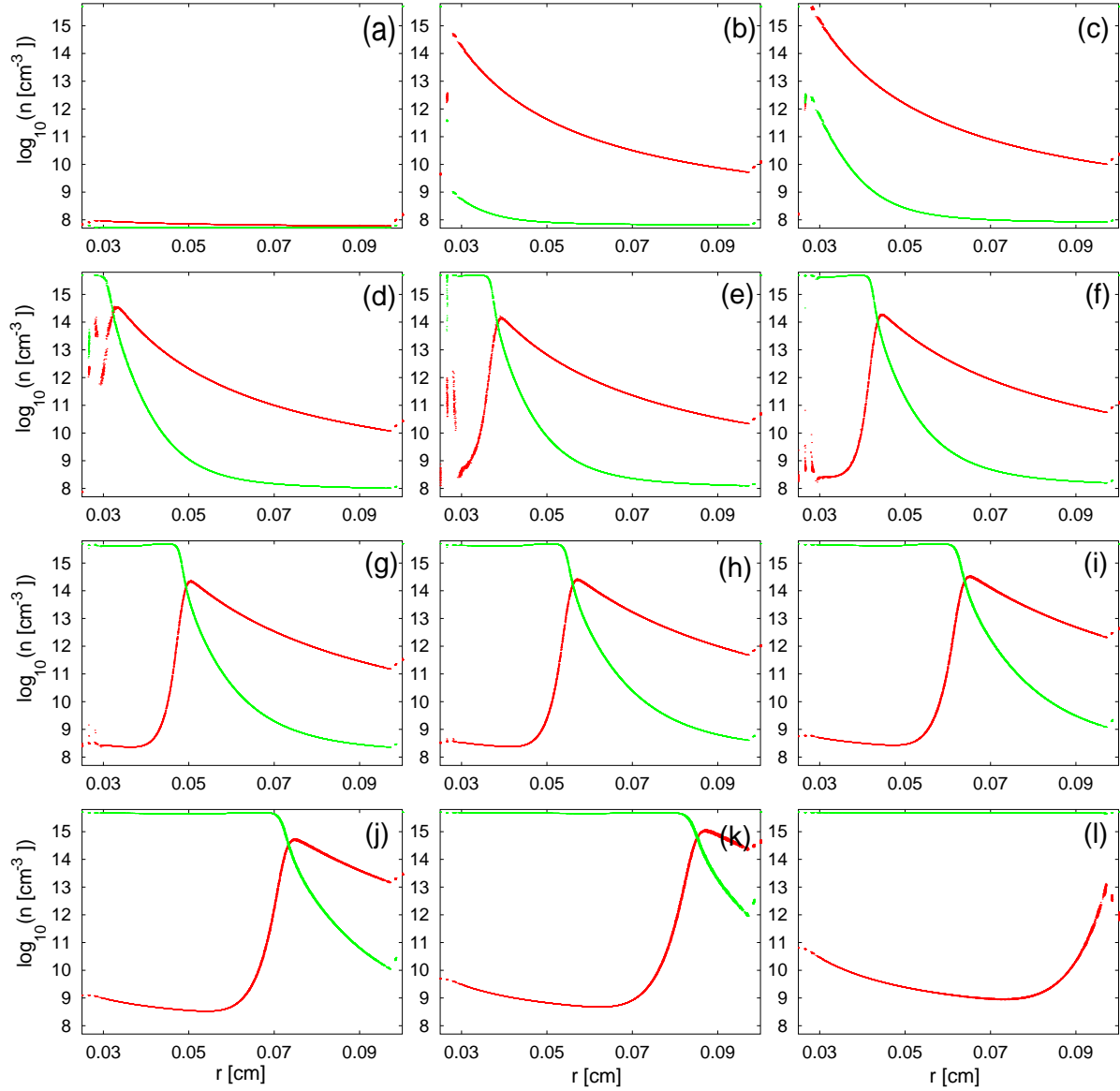


Figure 4.8: Radial distribution of the free electron density n (green dots; logarithmic scale) in a Corbino sample with reduced mobility, radii $R_1 = 0.25$ mm, $R_2 = 1.0$ mm and an applied voltage of $U_0 = 3.0$ V at different times t . Red dots: linear plot of the radial distribution of the electric field \mathcal{E} (lower bound $\mathcal{E} = 0$ V/cm, upper bound $\mathcal{E} = 80$ V/cm). (a): $t = 1$ ps, (b): $t = 0.03$ ns, (c): $t = 0.06$ ns, (d): $t = 0.09$ ns, (e): $t = 0.12$ ns, (f): $t = 0.15$ ns, (g): $t = 0.18$ ns, (h): $t = 0.21$ ns, (i): $t = 0.24$ ns, (j): $t = 0.27$ ns, (k): $t = 0.30$ ns, (l): $t = 0.33$ ns.

front is essentially a result of the monotonically decreasing radial field profile which is given by the mere geometry of the sample. As the movement of the individual carriers does not play a role it is not of importance which of the contacts is the injecting electrode.

An interesting effect can be obtained when artificially reducing the current density j . In the simulations this can be achieved by simply reducing the mobility μ according to eqs. (2.8), (2.9).

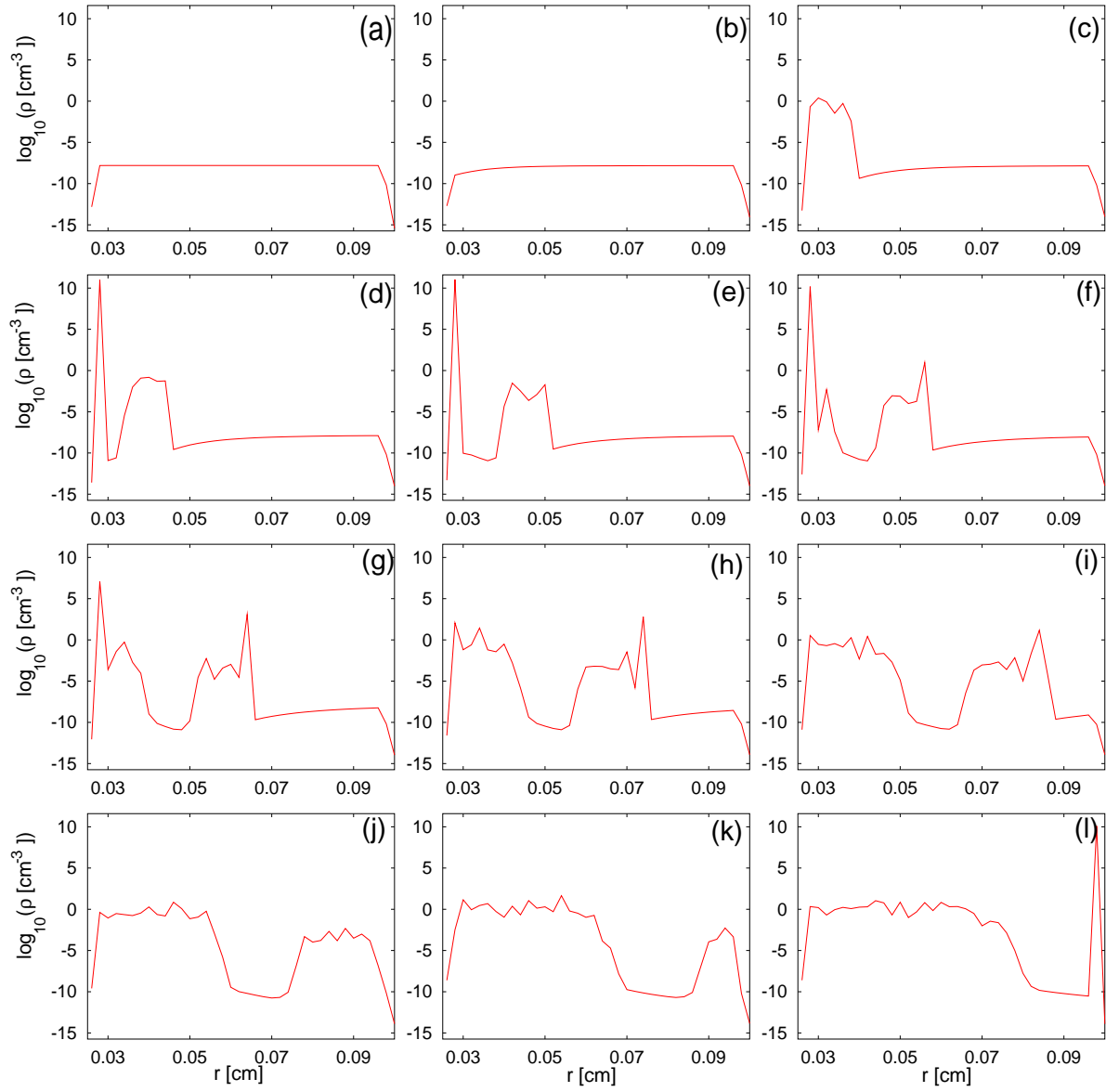


Figure 4.9: Radial distribution of the charge density ρ (divided by the elementary charge e) on a logarithmic scale for both positive and negative values (values of $|\rho/e| < 1 \text{ cm}^{-3}$ are set to zero) in a Corbino sample with radii $R_1 = 0.25 \text{ mm}$, $R_2 = 1.0 \text{ mm}$ and an applied voltage of $U_0 = 3.0 \text{ V}$ corresponding to Fig. 4.8.

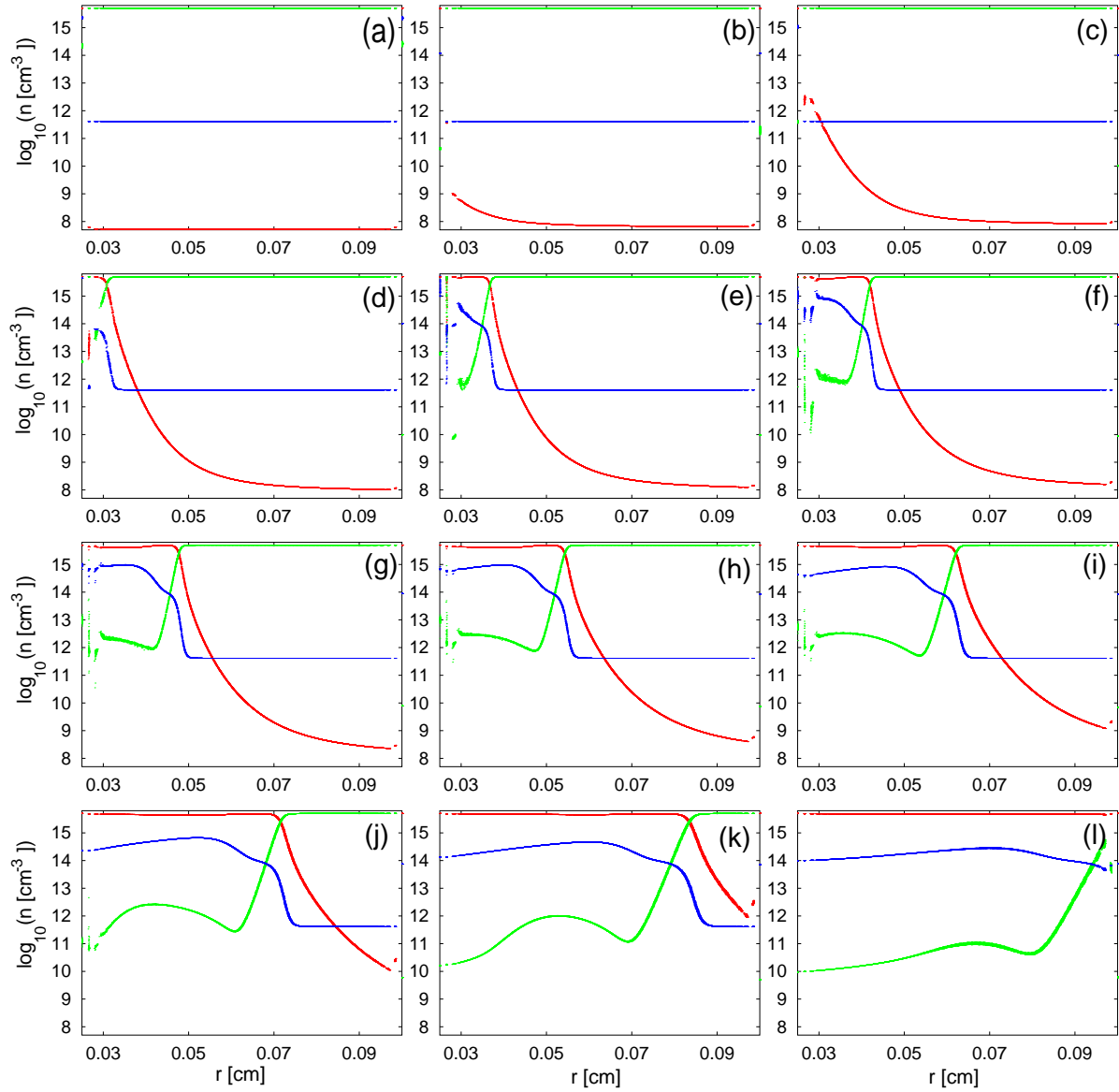


Figure 4.10: Radial distribution of the free electron density n (red dots), donor ground state and excited state, n_1 (green dots; located just below the upper bound) and n_2 (blue dots), respectively, in a Corbino sample with radii $R_1 = 0.25$ mm, $R_2 = 1.0$ mm and an applied voltage of $U_0 = 3.0$ V corresponding to Fig. 4.8.

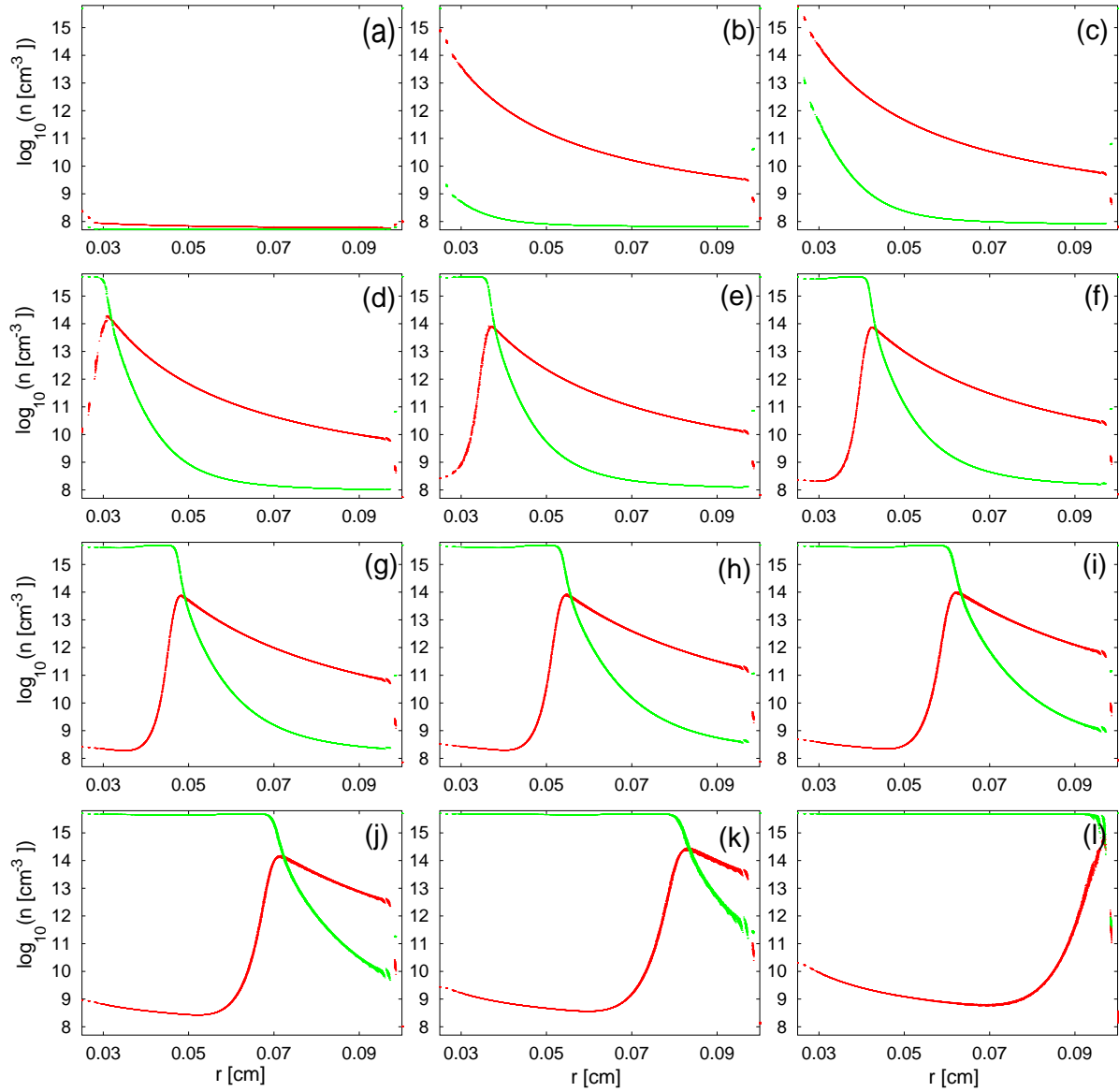


Figure 4.11: Radial distribution of the free electron density n (green dots; logarithmic scale) in a Corbino sample with reduced mobility, radii $R_1 = 0.25$ mm, $R_2 = 1.0$ mm and an applied voltage of $U_0 = -3.0$ V at different times t . Red dots: linear plot of the radial distribution of the electric field \mathcal{E} (lower bound $\mathcal{E} = 0$ V/cm, upper bound $\mathcal{E} = 88$ V/cm). (a): $t = 1$ ps, (b): $t = 0.03$ ns, (c): $t = 0.06$ ns, (d): $t = 0.09$ ns, (e): $t = 0.12$ ns, (f): $t = 0.15$ ns, (g): $t = 0.18$ ns, (h): $t = 0.21$ ns, (i): $t = 0.24$ ns, (j): $t = 0.27$ ns, (k): $t = 0.30$ ns, (l): $t = 0.33$ ns.

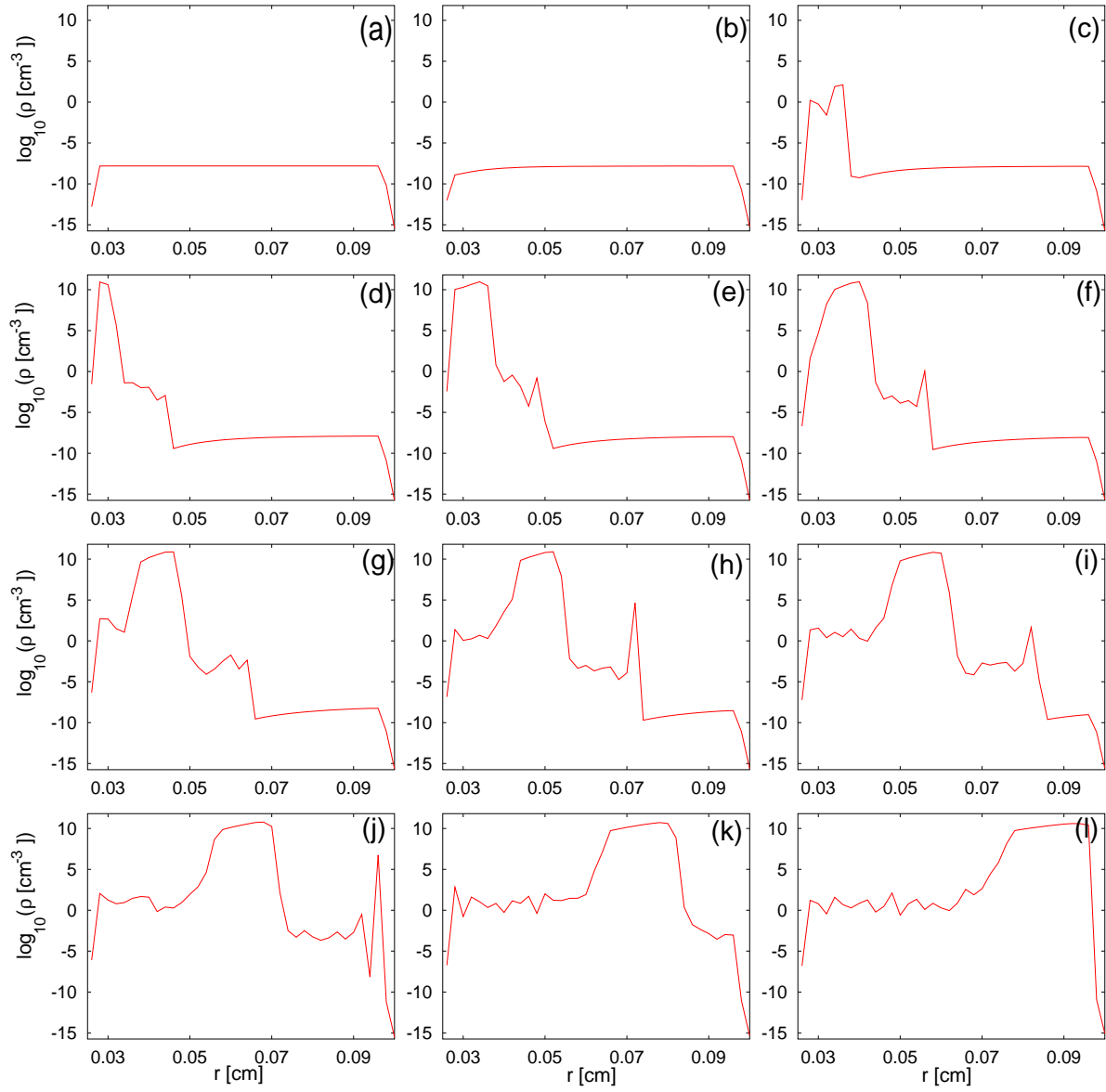


Figure 4.12: Radial distribution of the charge density ρ (divided by the elementary charge e) on a logarithmic scale for both positive and negative values (values of $|\rho/e| < 1 \text{ cm}^{-3}$ are set to zero) in a Corbino sample with radii $R_1 = 0.25 \text{ mm}$, $R_2 = 1.0 \text{ mm}$ and an applied voltage of $U_0 = -3.0 \text{ V}$ corresponding to Fig. 4.5.

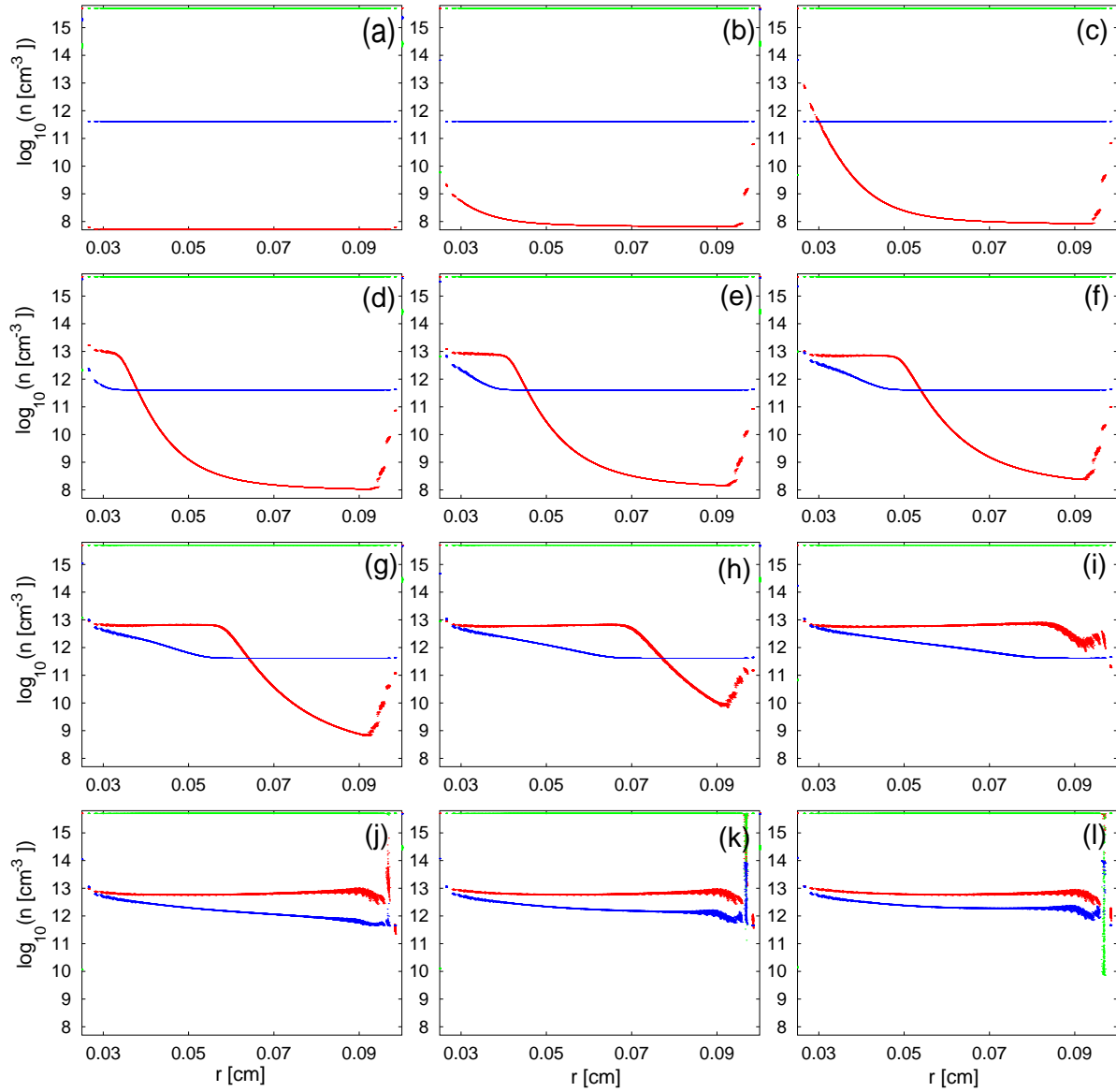


Figure 4.13: Radial distribution of the free electron density n (red dots), donor ground state and excited state, n_1 (green dots; located just below the upper bound) and n_2 (blue dots), respectively, in a Corbino sample with radii $R_1 = 0.25 \text{ mm}$, $R_2 = 1.0 \text{ mm}$ and an applied voltage of $U_0 = -3.0 \text{ V}$ corresponding to Fig. 4.11.

Setting μ to exactly zero would suppress any pattern formation since the system would have been reduced to the homogeneous generation-recombination process. We have thus changed μ to $1/1000$ of its original value. The results can be seen in Figs. 4.8 through 4.10 and 4.11 through 4.13 for positive and negative U_0 , respectively.

In both cases we again obtain the previously discussed mechanism for the impact ionization front which progresses with almost the same velocity as for the original mobility (about one third more slowly). This is a further indication that the individual movement of carriers is not

relevant. We note however that here the free electron density n behind the front immediately rises to almost the final value $N_D^* = 5 \cdot 10^{15} \text{ cm}^{-3}$ which corresponds to a state on the upper branch of the stationary current density-field characteristic and is found in stable, fully developed filaments. A possible explanation is that with a higher mobility and thus higher current density the free carriers produced by impact ionization get swept out of the active zone so fast that impact ionization cannot reach a high efficiency.

The question which naturally arises at this point after investigating the mechanism of the moving impact ionization front is why and under which conditions that radially symmetric front breaks up and how many streamers will develop. In principle an answer could be expected directly from an appropriate linear stability analysis. In a rigorous sense, such an analysis should be carried out by linearizing the full spatially two-dimensional constitutive equations about a time-dependent radially symmetric solution of a moving front in the finite system with constraints given by the external circuit, considering small azimuthal fluctuations. Such a calculation would require, at least to a good approximation, the knowledge of an expression for the radial symmetric solution of the nonlinear system, and it leads to an eigenvalue problem of spatial functions which again would have to be treated numerically.

Often linearizing around a homogeneous stationary state of a system, which can be done analytically and thus can be expected to lead to a better understanding of the system than a purely numerical analysis, yields good qualitative agreement to simulation results of the dynamics of the full space and time dependent nonlinear system. For low temperature impact ionization such an analysis has successfully been carried out in the case of transversal fluctuations by SCHÖLL and DRASDO for breathing cylindrical filaments [Sch87, Sch90] and by HÜPPER for the lateral movement of a current filament under the influence of a perpendicular magnetic field [Hüp93a, Hüp93c] as well in the case of longitudinal fluctuations, where GAA found traveling carrier density waves [Gaa96e]. In the case discussed here however, such an analysis around a homogeneous or at least electrically neutral state does not yield a wave length selection mechanism for the azimuthal instability (cf. appendix D). The deeper reason why here a stability analysis around a homogeneous state turns out to be an insufficient description is that an important assumption which had been made in all the former analyses, namely that the electric field \mathcal{E}_{\parallel} parallel to the transport is dominant in the GR terms and can be treated as spatially constant along the sample or even acting as a mere parameter, is no longer valid here. We have seen in the previous analysis that screening of the electric field, for instance, and more generally a spatially highly inhomogeneous field distribution along the transport direction are inherent conditions for the mechanism of the superfast impact ionization front. For the same reason the simple method of equal area rules, which has successfully been used to derive conditions of stability or, with the help of a co-moving frame, interfacial velocities in reaction-diffusion systems or for cylindrical filaments [Mor98, Sch87, Sch90, Sch01], cannot be applied to the impact ionization front because here both the electron concentrations and the electric field \mathcal{E} are spatially varying variables along the direction of current flow which are coupled through Gauss's law. Unlike for example in the Gunn effect, here the electrical charge density ρ , i. e. the spatial derivative of the electric field, is not directly identical to the free electron density, but they are rather coupled indirectly through the nonlinear generation-recombination relations, which makes a simple elimination of one of those quantities impossible and hence prevents

solving the integration across the sample length.

A qualitative argument for the instability of the impact ionization front against transversal (which here means azimuthal) fluctuations can be given as follows: a small bulge in the front coordinate (in the picture of a sharp interface) that points outwards in the direction of expansion will lead to a local squeezing of the equipotential lines just ahead of it. This is associated with a local increase in the curvature of the front and an increase of the local electric field. Thus impact ionization is locally enhanced, and the generation of free carriers is sped up at that position. Immediately at the tip of that bulge the interface between low and high free electron density will advance faster than in its vicinity. Analogously, small parts of the interface that slightly lag behind will lead to a stretching of the local potential profile, i. e. a local decrease of the electric field and hence of the rate of free electron generation through impact ionization. That positive feedback mechanism should lead to an amplification of small transversal fluctuations. However, in order to obtain a specific finite number of initial streamers one also requires a mechanism that limits the wavelength of the instability, damping out short wavelength transversal fluctuations. In the Mullins-Sekerka instability [Mul64] of a planar solidification interface expanding into an undercooled liquid, which bears a lot of similarity to the impact ionization front discussed here, that stabilizing mechanism on small spatial scales is given by curvature effects [Mor98]. Similar instability mechanisms of moving planar or curved [Pel88] interfaces have been identified in various areas such as flame fronts, dendrite growth, or viscous fingering occurring when air is pressed into a viscous fluid. While in those systems the dispersion relation $\lambda(k)$ for fluctuations transversal to the interface is generally positive and proportional to k for small transversal wave vectors k , the critical wave vector k_n above which $\lambda(k)$ is negative, i. e. the interface is stable against respective spatial fluctuations, depends of the short wavelength physics of the individual system [Saa98].

In media where propagation of an impact ionization front into a pre-ionized region occurs finger-like streamers similar to the ones obtained for GaAs in chapter 3 have been found both in experiments [Bas76] (for semiconductors) and in numerical simulations [Dha87] (for Nitrogen gas). A qualitative model with respect to streamers in plasmas was proposed by D'YAKONOV and KOCHAROVSKY [D'y88, D'y89].

For streamers propagating into a non-ionized state, i. e. with the velocity of the single carriers, numerical simulations were published for N_2 by VITELLO *et al* [Vit94]. Inspired by those simulations EBERT, VAN SAARLOOS and CAROLI took on with the theoretical description of that process [Ebe96b, Ebe97b]. They started their investigation with planar fronts, arguing that the relevant length scales of the interfacial zone are small compared to the width of a streamer. They proposed to treat the problem of streamer dynamics on two separate spatial scales: an *inner scale* on which the ionization processes occur within a thin sheet, as well as an *outer scale* on which pattern formation should be studied in an interfacial description. Our simulations of GaAs Corbino disks have shown that there such a separation of spatial scales does not exist.

The most important common feature of streamers evolving both into pre-ionized and into non-ionized media is the fact that screening of the electric field by free carriers plays a crucial role for the propagation mechanism. Since this has been shown to be the case for n-GaAs Corbino

disks as well it serves as the deeper motivation for our use of the term “streamer”, apart from the simple geometrical similarity of the resulting current density patterns.

For $p^+ - n - n^+$ Si diodes MINARSKY and RODIN have theoretically investigated the transverse stability of a propagating planar impact ionization front [Min94, Min97b, Min97a, Min00]. They analytically derived a mechanism for the long wave instability and also arrived at qualitative arguments for the minimum width of a streamer. More quantitative results are expected from numerical simulations which are subject of current research.

Chapter 5

Multistability and hysteresis

So far, we have studied the time-resolved process of nascence of a single filament in a thin-film Corbino sample. In this chapter we will investigate what happens upon slowly, i. e. quasi-statically increasing the applied bias U_0 . Unlike the results of the previous chapters such simulations can be directly compared to corresponding experimental measurements, which allows us to draw conclusions as to the quality of our underlying theoretical model.

In Fig. 5.1 a series of experimental photoluminescence images of a Corbino disk sample with increasing bias voltage is shown. With no applied bias (Fig. 5.1 (a)) we have a homogeneously low-conducting sample. We see that at a certain voltage a current filament, visible in Fig. 5.1 (b) as a dark stripe, spontaneously forms. With increasing bias it gets noticeably thicker (Fig. 5.1 (c)), until a second filament appears to have split from it (Fig. 5.1 (d)). The angle between the two filaments does not remain fixed but widens with further increase of the bias (Fig. 5.1 (e)). Another filaments forms (Fig. 5.1 (f)) which further broadens and shifts with rising current (Figs. 5.1 (f), (g)). The existing filaments can completely rearrange (Fig. 5.1 (h)) and grow in width (Fig. 5.1 (i)). Additional filaments appear and broaden (Figs. 5.1 (j), (k)) until the sample is almost entirely covered (Fig. 5.1 (l)).

The observation that a filament keeps its position over some part of the voltage ramp and then spontaneously shifts by a considerable angle is a strong indication that pinning at some sample inhomogeneities plays a role. When repeating the measurements with the same sample, the filaments do not necessarily appear at the same locations nor in the same order. A small perturbation such as a temporary change in the illumination of the sample at constant voltage might lead to a rearrangement of the existing filaments [Hir99]. This is a sign of the high degree of symmetry of the sample. In all cases, however, one obtains an increasing number of filaments with increasing current. An individual current filament can to some degree vary in width to account for a change in the overall current. There seems to be though a maximum filament width which is not exceeded, but instead a new filament appears. This experimental observation is in contrast to measurements in samples with stripe contacts where no such limit has been found [Hir00]. A possible explanation for that fact is given by the stationary model by NOVÁK which when applied to the Corbino geometry yields a decreasing local electric field \mathcal{E} near the outer contact in the middle of an existing filament with increasing filament width

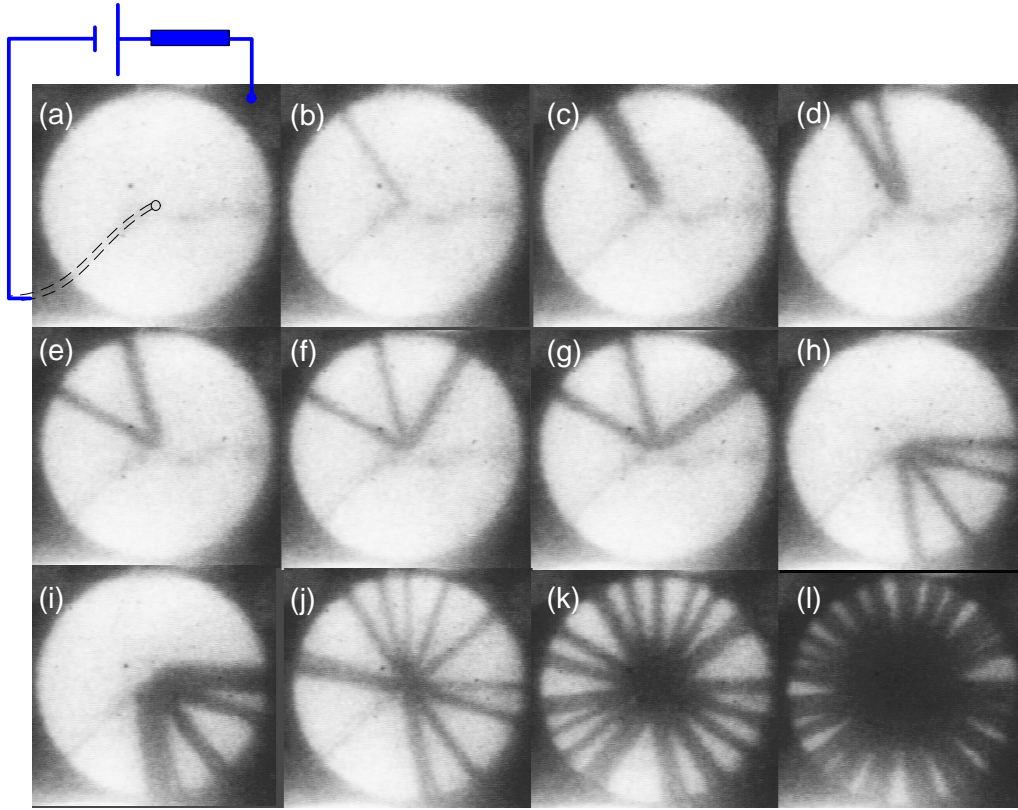


Figure 5.1: Experimental photoluminescence images of current filaments in a Corbino disk at different bias voltages (inner contact radius 0.04 mm, outer contact radius 1.05 mm, thickness of the epitaxial layer 3.0 μm). The dark areas correspond to regions of high current density. From (a) – (l) the total current I through the sample increases: (a): $I = 0$ mA, (b): $I = 0.10$ mA, (c): $I = 0.43$ mA, (d): $I = 0.45$ mA, (e): $I = 0.47$ mA, (f): $I = 0.58$ mA, (g): $I = 0.77$ mA, (h): $I = 0.80$ mA, (i): $I = 1.54$ mA, (j): $I = 1.71$ mA, (k): $I = 4.08$ mA, (l): $I = 7.08$ mA. (from [Sch00a])

[Nov97a, Hir00]. For some critical width the field at that point will be below the holding field \mathcal{E}_h , which can explain the existence of a maximum observed filament width and which might indicate a starting point for a splitting process. Since the stationary model cannot account for the dynamics of such a process and since the number of filaments present in the sample as well as their positions enter the model as a fixed assumption it cannot conclude whether such a splitting actually takes place or whether the system reacts to an increase in the overall current by the nucleation of an additional filament at some different position.

Fig. 5.2 shows a series of stationary experimental photoluminescence images of a Corbino sample with a larger central contact subject to increasing current. Here as well the number of filaments increases with rising current I . Again we can observe a tendency of new filaments to appear next to the already existing ones.

There is strong experimental evidence that the consecutive formation of an additional filament

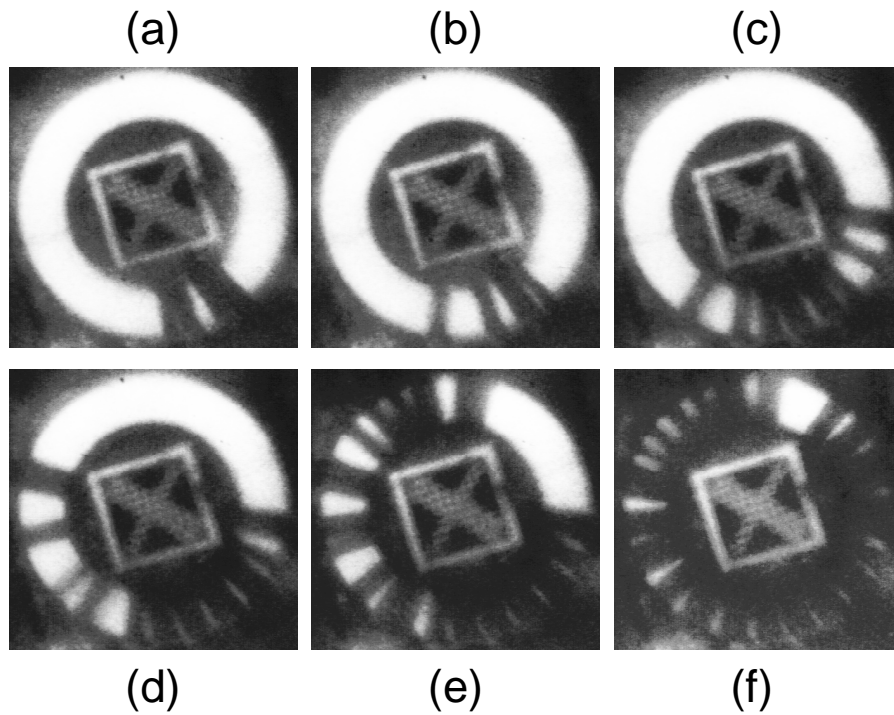


Figure 5.2: Experimental photoluminescence images of current filaments in a Corbino disk at different bias voltages (inner contact radius 0.1 mm, outer contact radius 1.5 mm, thickness of the epitaxial layer $3.0 \mu\text{m}$). The dark areas correspond to regions of high current density. From (a) – (f) the total current I through the sample increases: (a): $I = 1.54 \text{ mA}$, (b): $I = 1.58 \text{ mA}$, (c): $I = 3.73 \text{ mA}$, (d): $I = 5.73 \text{ mA}$, (e): $I = 9.54 \text{ mA}$, (f): $I = 13.0 \text{ mA}$. (from [Sch00a])

occurs through splitting of an existing one in at least some of the instances [Hir99, Hir00]. A direct experimental proof however is not possible due to the limited time resolution of the applied imaging technique. That is one motivation for an investigation through numerical simulations.

To simulate current filamentation in a Corbino disk under the effect of a subsequently increasing bias we again start from equilibrium by applying a small initial voltage U_0 in a virtually instantaneous ramp of 1 ps. We subsequently let the system evolve at that constant bias for an interval of time Δt . Δt should be long enough for the system to adapt to the change in the applied external voltage and reach a stationary state again. This reflects the notion of a sequential bias ramp and of measurements that are slow compared to the time scales of pattern formation, which holds in the corresponding experiments. After that interval of time we again linearly increase the bias by a small step ΔU_0 within 1 ps and anew simulate the dynamics for a further period Δt before taking the next voltage step ΔU_0 .

Fig. 5.3 depicts stationary spatial current density profiles of such a voltage sweep for a Corbino sample with inner and outer contact radii of $R_1 = 0.06$ mm and $R_2 = 1.05$ mm, respectively. We have started with an initial bias of $U_0 = 1.0$ V which we have subsequently increased in steps of $\Delta U_0 = 0.5$ V with an intermediate time interval of $\Delta t = 30$ ns between each bias step. Δt was chosen to be sufficiently longer than the nucleation time for a fully developed current filament obtained in the simulations in chapter 3.

For $U_0 = 1.5$ V (Fig. 5.3 (a)) the system is completely low-conducting. The equipotential lines are concentric circles. After the next voltage step (Fig. 5.3 (b) at $U_0 = 2.0$ V) a stable filament has formed. With further increase of the applied voltage U_0 the current density within the filament rises only slightly, while the filament's width increases (Figs. 5.3 (c) – (e)). The filament has parallel lateral borders, in agreement with experimental results [Hir00]. As a consequence, the electric field is notably distorted. Within the filament the equipotential lines are straight equidistant lines, reflecting the spatially constant electric field within the filament. With increasing width the filament starts to engulf the small central contact whose diameter it exceeds.

When the filament width starts to approach the order of the contact distance, i. e. the width of the filament becomes similar to its length, (Fig. 5.3 (f)) the parallel bordered shape gets lost starting from the outer contact, and the filament more and more assumes a convex shape, paying tribute to the curvature of the contacts (Fig. 5.3 (g)).

This transition from a thin parallell-bordered to a convex-shaped filament with increasing current has also been observed in both measurements and simulations for current filamentation between two small circular contacts [Hir00, Sch00a]. Not surprisingly, the filamentary shape found here in a Corbino sample is almost identical to one half of a filament in those geometries. The results obtained here from the dynamical simulation of the full nonlinear system are in excellent agreement to the shape of the filamentary boundaries calculated for the Corbino geometry from NOVÁK's stationary model [Nov97a, Hir00].

For $U_0 = 173.5$ V (Fig. 5.3 (h)) a second filament spontaneously forms. It joins at that sector of the central contact which is covered the least by the first filament. Further increase of U_0 again leads to a broadening of that new filament which upon attaining a width of the order of the contact distance also starts to gradually loose its parallel-bordered shape (Figs. 5.3 (i) – (l)).

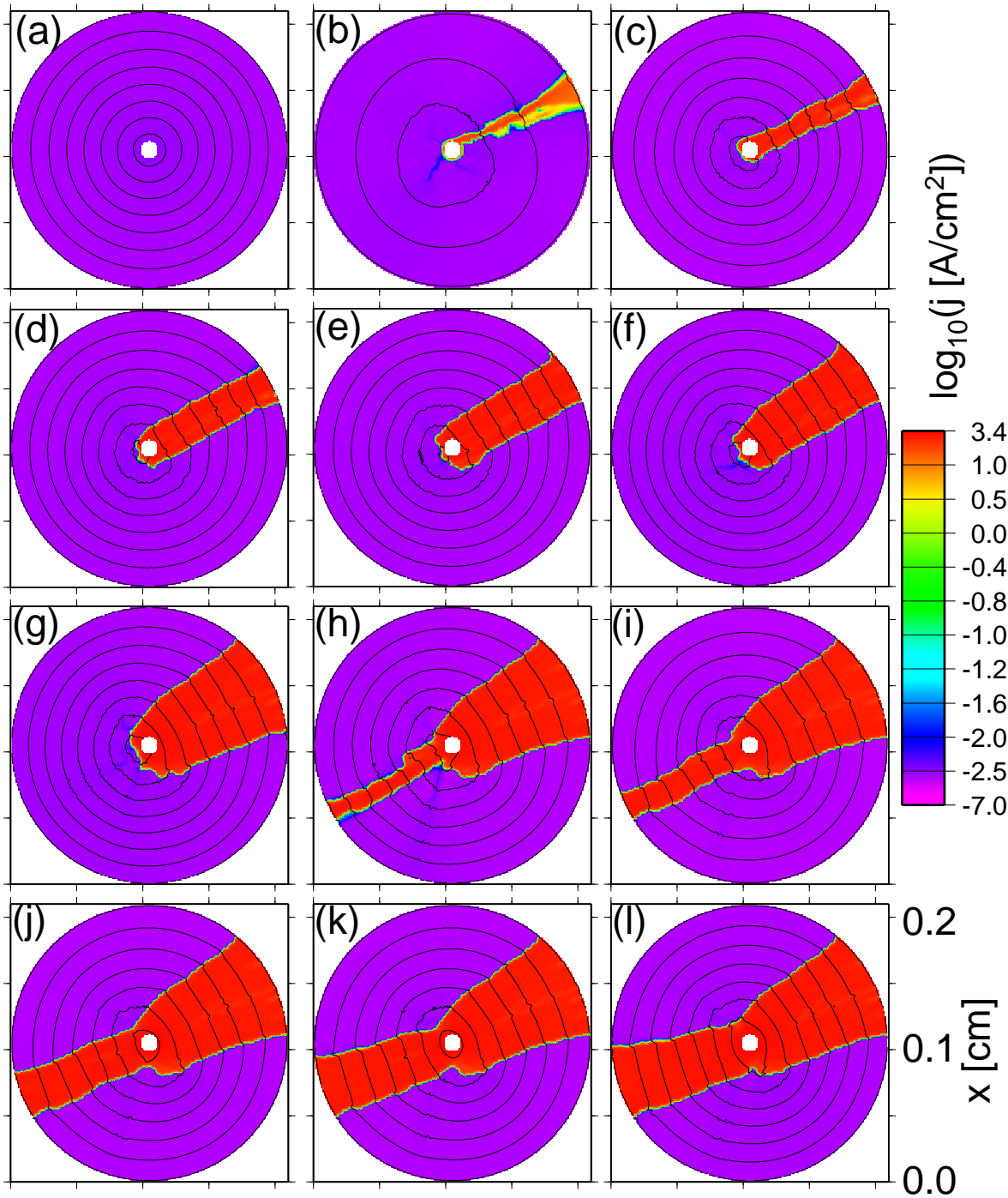


Figure 5.3: Nascence and expansion of two current filaments in a Corbino disk sample with radii $R_1 = 0.06$ mm, $R_2 = 1.05$ mm and a slowly increasing bias U_0 : current density profiles at different bias (a): $U_0 = 1.5$ V, sample voltage $U = 1.50$ V, total current $I = 2.58 \cdot 10^{-8}$ A; (b): $U_0 = 2.0$ V, $U = 0.56$ V, $I = 1.44 \cdot 10^{-4}$ A; (c): $U_0 = 23.5$ V, $U = 1.23$ V, $I = 2.23 \cdot 10^{-3}$ A; (d): $U_0 = 61.0$ V, $U = 1.36$ V, $I = 5.96 \cdot 10^{-3}$ A; (e): $U_0 = 83.0$ V, $U = 1.33$ V, $I = 8.17 \cdot 10^{-3}$ A; (f): $U_0 = 106.5$ V, $U = 1.37$ V, $I = 1.05 \cdot 10^{-2}$ A; (g): $U_0 = 164.5$ V, $U = 1.41$ V, $I = 1.63 \cdot 10^{-2}$ A; (h): $U_0 = 173.5$ V, $U = 1.24$ V, $I = 1.72 \cdot 10^{-2}$ A; (i): $U_0 = 187.5$ V, $U = 1.18$ V, $I = 1.86 \cdot 10^{-2}$ A; (j): $U_0 = 237.5$ V, $U = 1.26$ V, $I = 2.36 \cdot 10^{-2}$ A; (k): $U_0 = 258.0$ V, $U = 1.29$ V, $I = 2.56 \cdot 10^{-2}$ A; (l): $U_0 = 300.5$ V, $U = 1.39$ V, $I = 2.99 \cdot 10^{-2}$ A. Equipotential lines are spaced by 0.2 V.

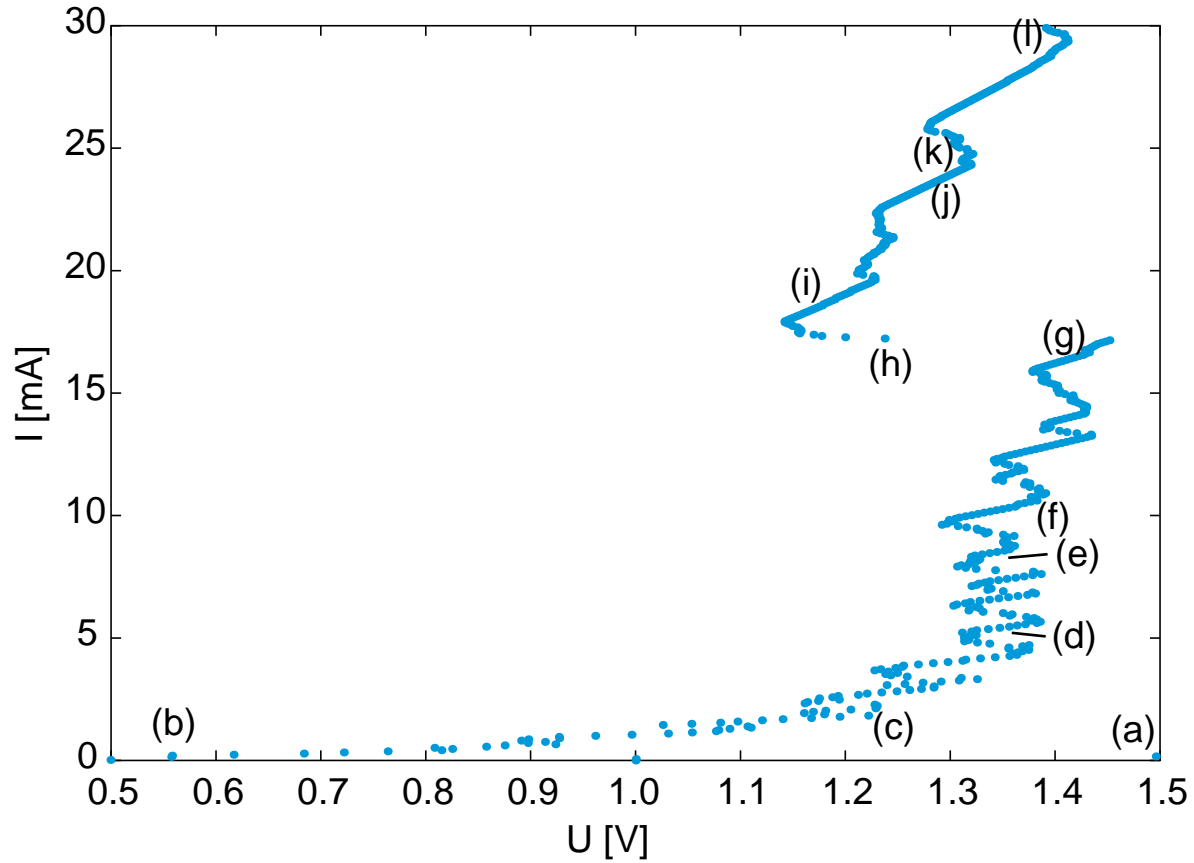


Figure 5.4: Current-voltage characteristic of a Corbino disk sample with radii $R_1 = 0.06$ mm, $R_2 = 1.05$ mm. The letters indicate the corresponding current density profiles in Fig. 5.3.

Fig. 5.4 depicts the corresponding current-voltage characteristic. It has been obtained by recording the total current I as a function of the sample voltage U after each time step Δt . The letters (a) – (l) indicate the corresponding current density distributions of Fig. 5.3. The current-voltage characteristic can clearly be divided into three separate parts, corresponding to qualitatively different states of the sample: the first part represents the initial state of the low-conducting sample with no filamentation. In the linear plot it is made up of just three dots lying virtually on the lower horizontal axis due to the small current. We have seen in Figs. 5.3 (a), (b) that upon increasing the bias U_0 from 1.5 V to 2.0 V a filament spontaneously appears. In terms of the electric field, those values correspond to about 15.1 V/cm and 20.2 V/cm, respectively, if one assumes a linear electric potential drop between the two contacts. We have seen that the latter condition is fulfilled once a filament has formed, and we have learned in chapter 3 that this is also the case already during the transient pre-filamentary phase, even if a pre-filament (or all of them) later dies due to insufficient field. The first stable filament thus forms once the electric field $U_0/\Delta R$ has passed the threshold field \mathcal{E}_{th} , which in chapter 2 has been shown to be about 17 V/cm for our material system. $\Delta R = R_2 - R_1$ here is the contact distance.

The nucleation of a filament means a spontaneous increase in the total current I and thus via

Kirchhoff's law (3.1) a respective drop in the sample voltage U . This causes the backward jump between points (a) and (b) in Fig. 5.4. The new sample voltage $U = 0.5$ V corresponds to a field of $\mathcal{E} = 5.1$ V/cm and is thus still higher than the holding field \mathcal{E}_h of about 4 V/cm. As the current density within a fully-developed stable filament is a fixed quantity for a given field \mathcal{E} that requirement limits the initial width of a newly formed filament.

With further increasing bias U_0 the current density within the filament rises, and the filament gradually broadens, which both leads to a steady increase of the total current I . Depending on whether this increase ΔI following a bias step ΔU_0 is smaller or greater than $\Delta U_0/R_L$ the sample voltage U in turn either slightly increases or decreases, according to Kirchhoff's law (3.1). This is the reason for the zig-zag shape of the characteristic. In particular after the current density within the filament has saturated ((c)) small spontaneous expansions in the detailed filamentary shape as a reaction to a bias step ΔU_0 can result in a sufficiently large ΔI and thus a small backward jump in the current-voltage characteristic. In experiments with point contact samples such small jumps in the characteristic have in fact been observed and could be attributed to small local sample imperfections [Kli99]. In the simulations the finite resolution of the numerical grid takes a similar role.

Between points (g) and (h) the second filament nucleates. Due to the high load resistance R_L of 10 k Ω the resulting rather minor increase of the overall current leads to a noticeable jump backwards in the characteristic, breaking it up into discontinuous parts each corresponding to a different number of filaments. Those results are in line with respective experimental measurements of a current-voltage characteristic of an n-doped GaAs Corbino disk sample [Ebe97a].

Fig. 5.5 shows a series of current density profiles of a Corbino sample with radii $R_1 = 0.5$ mm and $R_2 = 1.05$ mm. Starting from $U_0 = 0.5$ V the external voltage is again increased in steps of $\Delta U_0 = 0.5$ V. In order to stay within a reasonable overall computing time here we have limited the intermediate interval of time Δt between each small voltage step to 20 ns.¹ At $U_0 = 150$ V the direction of the bias ramp is reversed, and U_0 is decreased again in steps of $\Delta U_0 = -0.5$ V.

We see that starting from the non-conducting state (Fig. 5.5 (a)) one filament after the other spontaneously forms with increasing bias (Figs. 5.5 (b) – (i)). As in the previously presented simulation new filaments have the tendency to join the central electrode at sectors that have not yet been engulfed by the existing filaments. In Fig. 5.5 (h) a new filament is already visible in the logarithmic current density plot. Nevertheless, its current density is still orders of magnitude smaller than in the fully developed ones. Only after one further bias step (Fig. 5.5 (i)) a full filament has formed at that position.

For $U_0 = 150$ V (Fig. 5.5 (j)) there exist six stable current filaments. Reversing the direction of the bias ramp leads to a gradual uniform decline of all of them with decreasing U_0 (Fig. 5.5 (k)). For zero bias (Fig. 5.5 (l)) all six filaments have vanished.

In the corresponding current-voltage characteristic (Fig. 5.6) we can again clearly distinguish between separate parts for the different numbers of stable filaments. Reversing the bias sweep direction we find a monotonical descent of the total current I , indicating a uniform decline in

¹Still such a simulation typically takes a few weeks to two months on a dedicated 500 MHz Intel Pentium III system to complete.

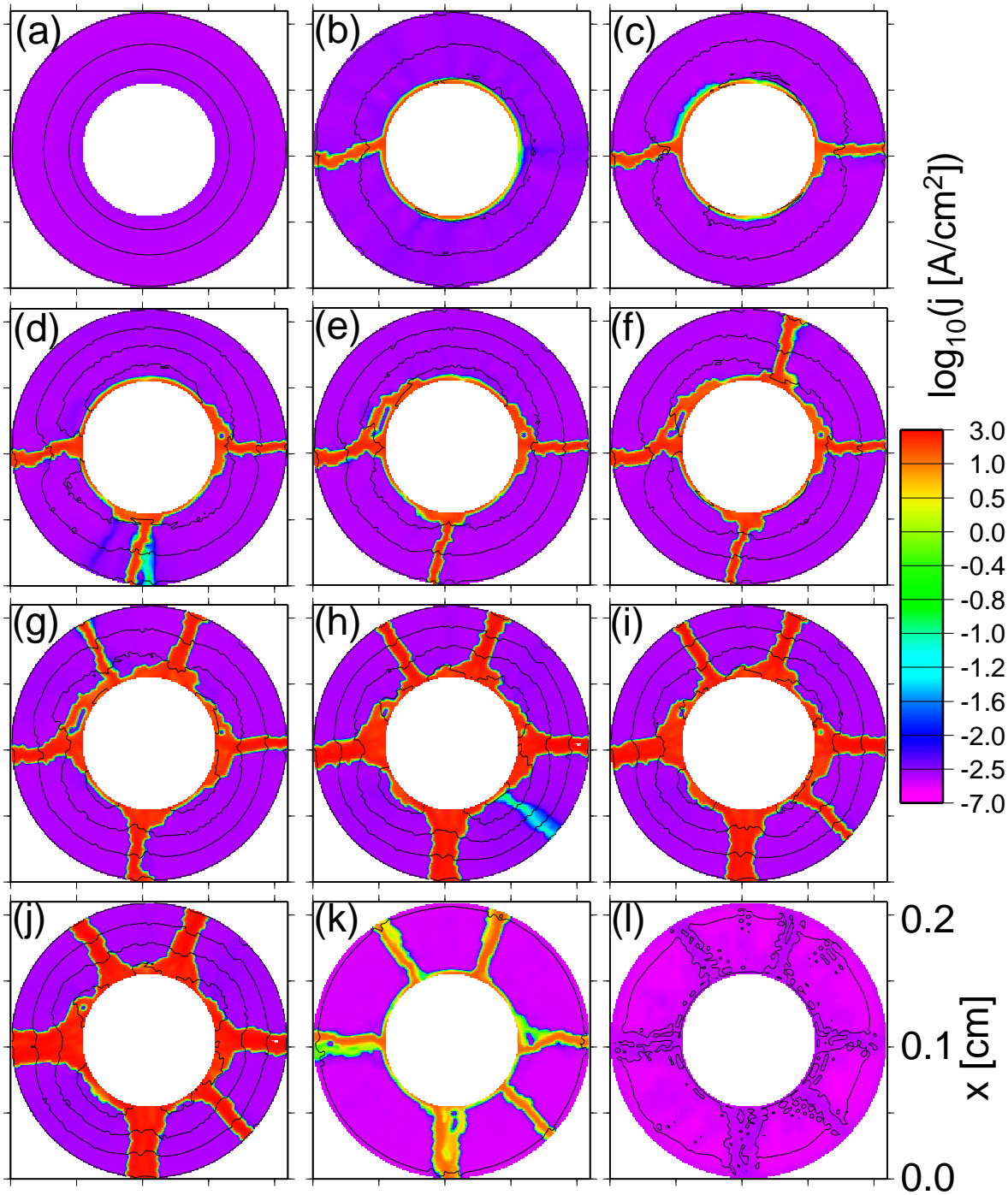


Figure 5.5: Consecutive nascence and subsequent decay of up to six current filaments in a Corbino disk sample with radii $R_1 = 0.5$ mm, $R_2 = 1.05$ mm and a slowly increasing bias U_0 : current density profiles at different bias (a): $U_0 = 1.0$ V, sample voltage $U = 0.51$ V, total current $I = 4.91 \cdot 10^{-5}$ A; (b): $U_0 = 1.5$ V, $U = 0.41$ V, $I = 1.09 \cdot 10^{-4}$ A; (c): $U_0 = 3.5$ V, $U = 0.37$ V, $I = 3.13 \cdot 10^{-4}$ A; (d): $U_0 = 11.0$ V, $U = 0.55$ V, $I = 1.04 \cdot 10^{-3}$ A; (e): $U_0 = 13.5$ V, $U = 0.57$ V, $I = 1.29 \cdot 10^{-3}$ A; (f): $U_0 = 18.5$ V, $U = 0.53$ V, $I = 1.80 \cdot 10^{-3}$ A; (g): $U_0 = 45.5$ V, $U = 0.59$ V, $I = 4.49 \cdot 10^{-3}$ A; (h): $U_0 = 89.5$ V, $U = 0.67$ V, $I = 8.89 \cdot 10^{-3}$ A; (i): $U_0 = 90.0$ V, $U = 0.61$ V, $I = 8.94 \cdot 10^{-3}$ A; (j): $U_0 = 150.0$ V, $U = 0.65$ V, $I = 1.49 \cdot 10^{-2}$ A; (k): $U_0 = 2.0$ V, $U = 0.15$ V, $I = 1.85 \cdot 10^{-4}$ A; (l): $U_0 = 0.0$ V, $U = 0.0$ V, $I = 1.23 \cdot 10^{-10}$ A. Equipotential lines are spaced by 0.2 V.

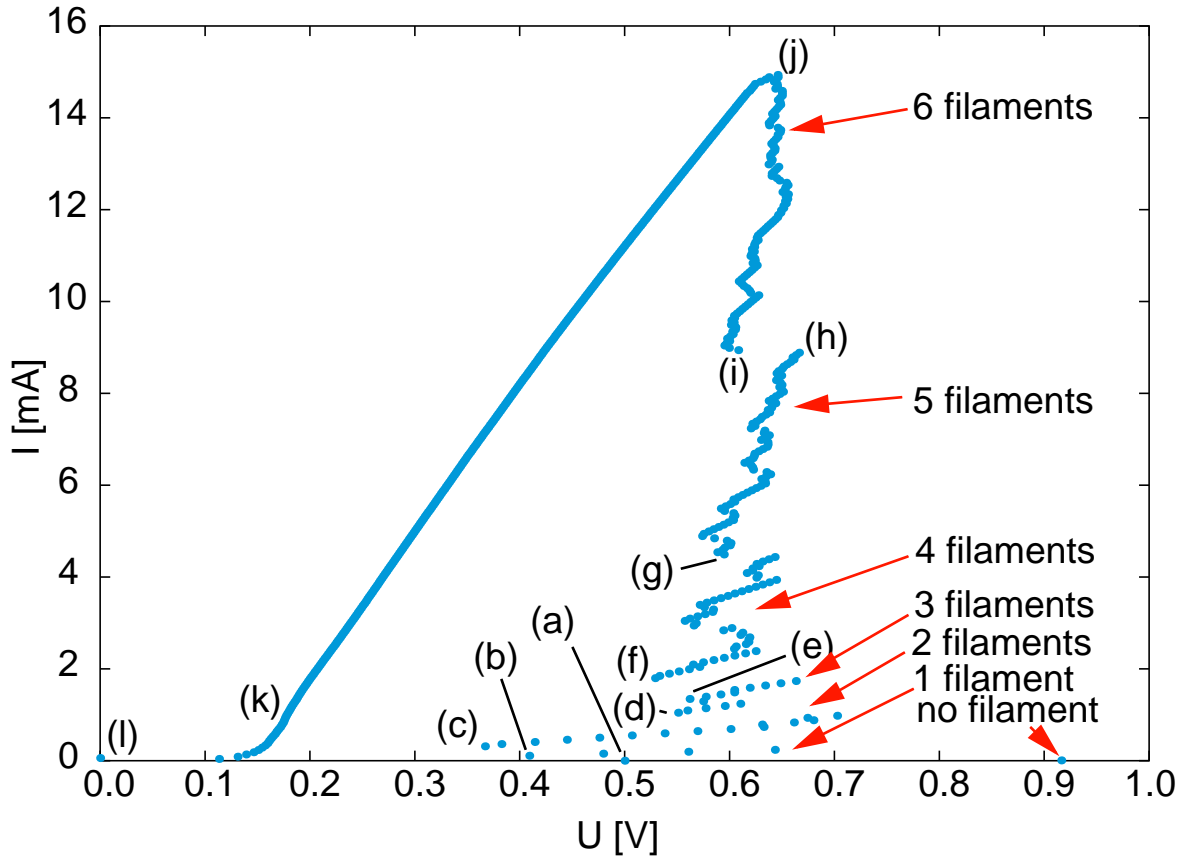


Figure 5.6: Current-voltage characteristic of a Corbino disk sample with radii $R_1 = 0.5$ mm, $R_2 = 1.05$ mm. The letters indicate the corresponding current density profiles in Fig. 5.5.

the current density in all of the existing filaments with decreasing U_0 . Since the system does not follow back the same path it has taken for the rising bias, where one filament has appeared after the other, we have a hysteretic behavior. In bias sweep-up and sweep-down experiments with Corbino disk samples hysteresis in the current-voltage characteristic has also been observed. There however, the filaments have been found to disappear one after another, which manifests itself in a discontinuous characteristic for the down-sweep as well [Ebe97a]. The fact that in the calculations the traces of the filaments which have vanished can still clearly be seen in the electric potential profile ((Fig. 5.5 (l)) is an indication that the relevant recombination timescales are longer than the simulation time Δt used².

In order to test this hypothesis we simulate a voltage ramp applied to a Corbino disk with radii $R_1 = 0.2$ mm and $R_2 = 1.05$ mm. We start with $U_0 = 1.0$ V and increase in small steps of $\Delta U_0 = 0.125$ V up to $U_0 = 25.875$ V, after which U_0 is again decreased in steps of $\Delta U_0 = -0.125$ V. As in the previous simulations each voltage step is applied as a sharp linear ramp of 1 ps length,

²In the simulations of current filamentation it has turned out quite generally that less prominent patterns tend to be visible much better or longer in the spatial potential profile than in the electron or current density profiles.

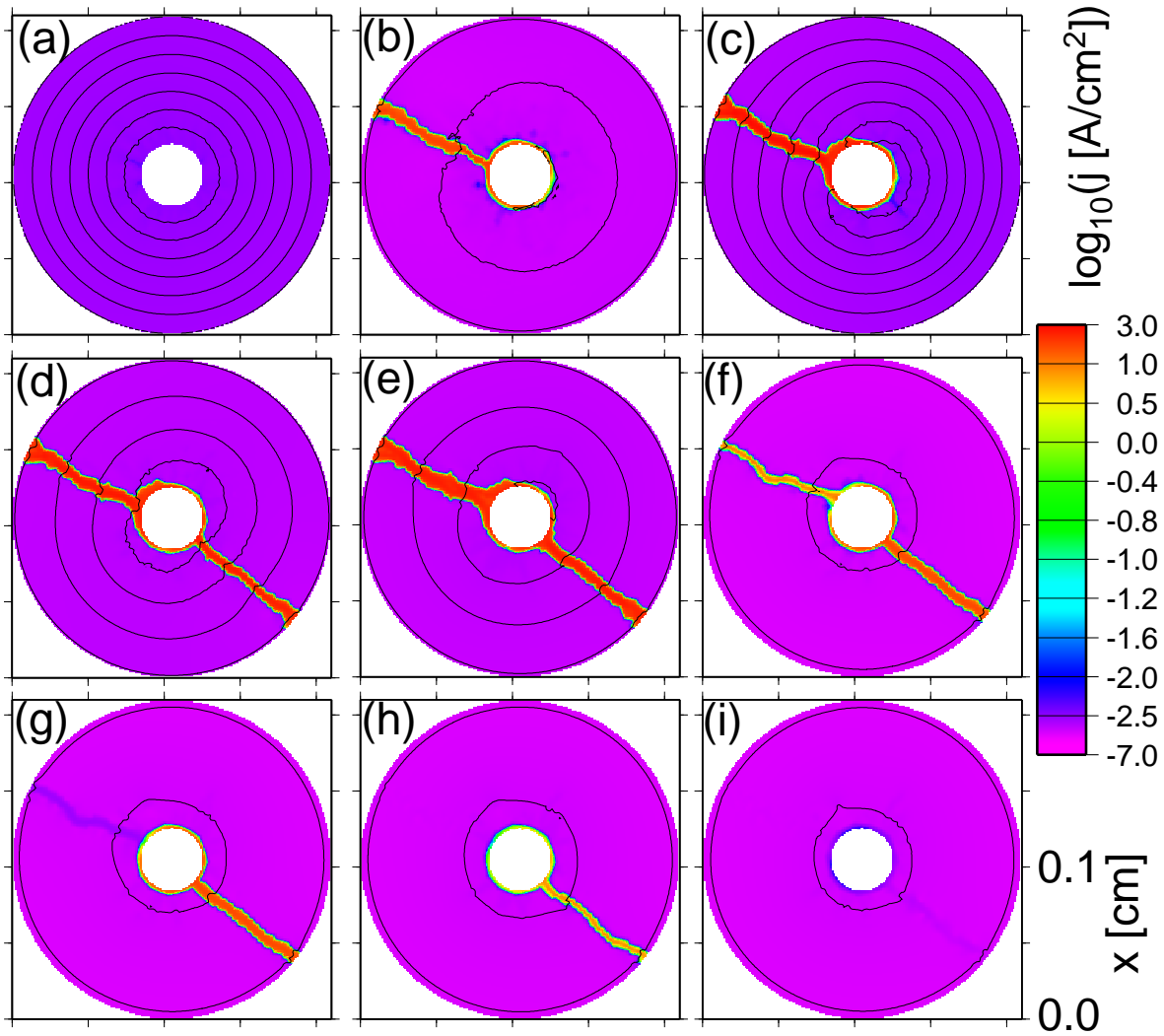


Figure 5.7: Consecutive nascence and decay of two current filaments in a Corbino disk sample with radii $R_1 = 0.2$ mm, $R_2 = 1.05$ mm with slowly increasing and decreasing bias U_0 : current density profiles at different bias (a): $U_0 = 1.375$ V, sample voltage $U = 1.374$ V, total current $I = 7.16 \cdot 10^{-8}$ A; (b): $U_0 = 1.50$ V, $U = 0.38$ V, $I = 1.11 \cdot 10^{-4}$ A; (c): $U_0 = 11.75$ V, $U = 1.17$ V, $I = 1.05 \cdot 10^{-3}$ A; (d): $U_0 = 11.875$ V, $U = 0.71$ V, $I = 1.10 \cdot 10^{-3}$ A; (e): $U_0 = 13.25$ V, $U = 0.59$ V, $I = 1.28 \cdot 10^{-3}$ A; (f): $U_0 = 1.25$ V, $U = 0.26$ V, $I = 9.87 \cdot 10^{-5}$ A; (g): $U_0 = 1.125$ V, $U = 0.26$ V, $I = 8.61 \cdot 10^{-5}$ A; (h): $U_0 = 0.375$ V, $U = 0.28$ V, $I = 9.92 \cdot 10^{-6}$ A; (i): $U_0 = 0.25$ V, $U = 0.25$ V, $I = 4.09 \cdot 10^{-10}$ A. Equipotential lines are spaced by 0.2 V. (Bias ramp with positive slope: (a) – (d); ramp with negative slope (e) – (i); maximum bias: $U_0 = 25.875$ V)

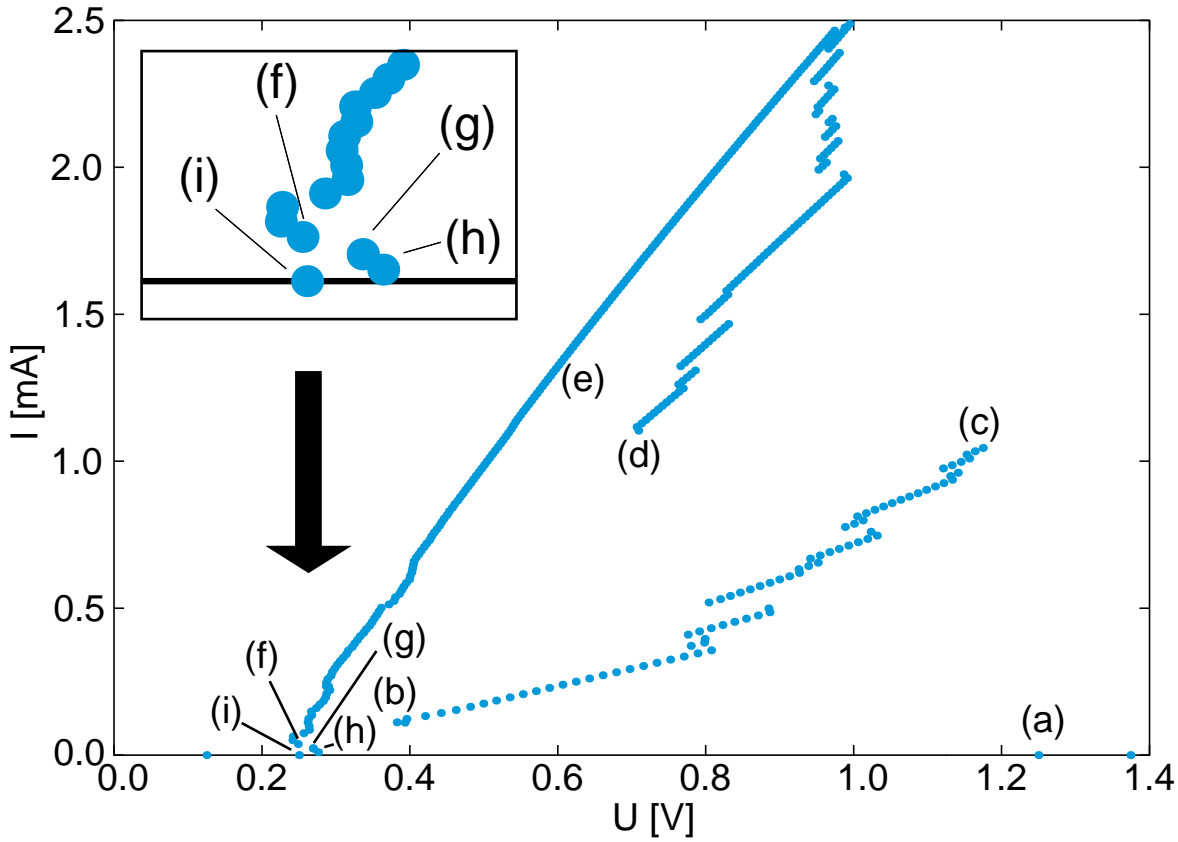


Figure 5.8: Current-voltage characteristic of a Corbino disk sample with radii $R_1 = 0.2$ mm, $R_2 = 1.05$ mm. The letters indicate the corresponding current density profiles in Fig. 5.7. The inset enhances the part of the down-sweep where the two filaments subsequently vanish.

which is here followed by a “relaxation” interval of $\Delta t = 200$ ns, i. e. ten times longer than in the previous simulation.

The respective series of current density profiles is depicted in Fig. 5.7, and the corresponding current-voltage characteristic is shown in Fig. 5.8. Again we find that a single current filament nucleates at $U_0 = 1.5$ V (Fig. 5.7 (b)), which for the given contact dimensions translates to an average field of 17.6 V/cm, i. e. just above the threshold field \mathcal{E}_{th} (the resulting sample voltage of $U = 0.38$ V after the filament formation again corresponds to an electric field of 4.5 V/cm, which is slightly higher than the holding field \mathcal{E}_h). A second filament forms at $U_0 = 11.875$ V (Fig. 5.7 (d)).

Reversing the direction of the bias ramp again (between (d) and (e)), both filaments gradually decline. For $U_0 = 1.125$ V (Fig. 5.7 (g)) the first filament spontaneously disappears. In the current-voltage characteristic this leads to a jump towards higher sample voltage U due to the drop in the total current I . Fig. 5.8 clearly shows that the characteristic exhibits a discontinuity here, owing to the sudden change in the number of filaments. The first filament still remains for some bias range until it vanishes as well for $U_0 = 0.25$ V (Fig. 5.7 (i)). We have thus

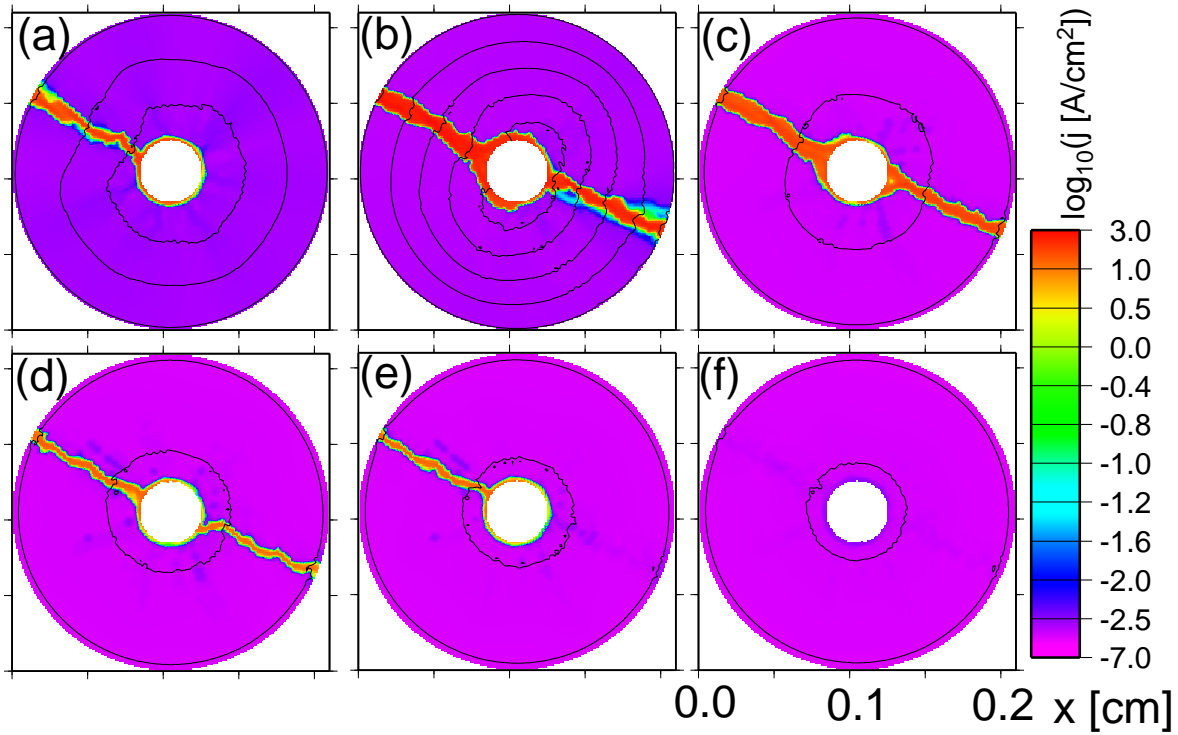


Figure 5.9: Consecutive nascence and decay of two current filaments in a Corbino disk sample with radii $R_1 = 0.2$ mm, $R_2 = 1.05$ mm with slowly increasing and decreasing bias U_0 : current density profiles at different bias (a): $U_0 = 1.75$ V, sample voltage $U = 0.54$ V, total current $I = 1.21 \cdot 10^{-4}$ A; (b): $U_0 = 16.5$ V, $U = 0.84$ V, $I = 1.57 \cdot 10^{-3}$ A; (c): $U_0 = 3.25$ V, $U = 0.32$ V, $I = 2.93 \cdot 10^{-4}$ A; (d): $U_0 = 0.75$ V, $U = 0.27$ V, $I = 4.79 \cdot 10^{-5}$ A; (e): $U_0 = 0.5$ V, $U = 0.26$ V, $I = 2.43 \cdot 10^{-5}$ A; (f): $U_0 = 0.25$ V, $U = 0.25$ V, $I = 3.97 \cdot 10^{-10}$ A. Equipotential lines are spaced by 0.2 V. (Bias ramp with positive slope: (a) – (b); ramp with negative slope (c) – (f); maximum bias: $U_0 = 20.75$ V)

seen that using a sufficiently long simulation time we obtain a successive disappearance of the individual current filaments on a descending bias ramp as well as a respective discontinuous current-voltage characteristic.

Figs. 5.9, 5.10 show a current density plot series as well as the respective current-voltage characteristic of a simulation series with a nominally identical sample (radii $R_1 = 0.2$ mm, $R_2 = 1.05$ mm) as in Fig. 5.7. Here we increase the applied voltage U_0 in steps of 0.25 V and simulate for 20 ns after each voltage step. Upon reaching $U_0 = 20.75$ V the bias sweep direction is reversed again. On the descending bias ramp, for the last few voltage steps, starting with $U_0 = 0.75$ V, a significantly longer simulation time of $\Delta t = 300$ ns is used in each bias step.

Again, we observe the nucleation of two filaments at $U_0 = 1.75$ V and $U_0 = 16.5$ V, respectively (Figs. 5.9 (a) and (b)). If we compare those values to the respective voltages in Figs. 5.7 (b) and (d) we find them to be somewhat higher than in that previous simulation. This indicates that even for the generation time of a filament the shorter simulation time Δt used here is not

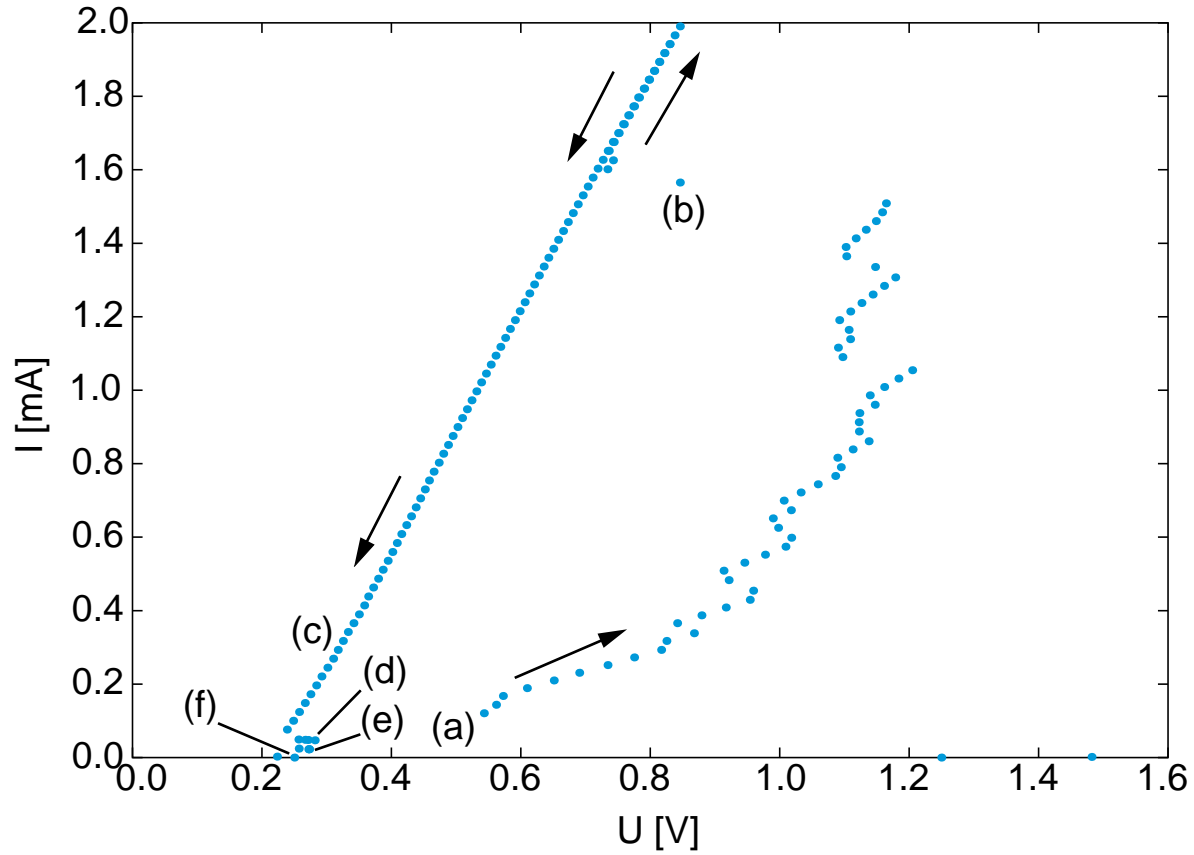


Figure 5.10: Current-voltage characteristic of a Corbino disk sample with radii $R_1 = 0.2$ mm, $R_2 = 1.05$ mm. The letters indicate the corresponding current density profiles in Fig. 5.9. The arrows denote the sweep direction.

completely sufficient (i. e. if we use a longer simulation time, which is still orders of magnitude shorter than any experimental time scales, the new filaments already appear for some lower U_0). On the down-sweep ramp ((c) – (f)) this time the filament which had appeared second is the first to disappear again, in contrast to the previous simulation.

The fact that minor differences like the simulation time or the size of the bias steps influence the order of disappearance of the filaments indicates the high degree of symmetry of the system and the resulting equivalence of different states. On the other hand, the formation of several filaments with increasing bias and the corresponding discontinuous multistable current voltage characteristic as such is not affected by the details of the respective simulation and can therefore be regarded as a robust, inherent property of the system.

In summary, we have demonstrated that our model produces a spontaneous consecutive nucleation and disappearance, respectively, of multiple current filaments in a Corbino disk subject to an ascending or descending voltage ramp. In the current-voltage characteristic this leads to the occurrence of several discontinuous branches, each of which corresponds to a state of the sample with a specific number of filaments. Since for a given voltage U within a certain

range, corresponding to the bistability range of the microscopic current density-field relation, the system can attain different values of the overall sample current I depending on the number of existing filaments, it thus exhibits a high degree of multistability. Reversing the direction of the bias ramp we find hysteresis in the current-voltage characteristic. Those results are in good agreement to corresponding experimental measurements on thin-film GaAs samples with concentric circular contacts.

We have not found, however, in the simulations any indication of new filaments forming via a splitting process, whereas in the experiments there is evidence that at least some of the filaments emerge through such a process. Calculations by NOVÁK suggest that for a splitting process the electric field right at the outer contact within an existing filament might play a crucial role. This opens up room for speculation whether the numerical treatment of the boundary conditions at the contacts could be a decisive factor for the specific formation process of a new filament. Also, the time scales used here in the simulations between each voltage step might be too short for any splitting to occur since splitting can be expected to be a rather slow process. Simulations which could resolve that question would likely have to employ a more refined treatment of the contacts and substantially longer simulation times as well as smaller bias steps, which is beyond the scope and the computational capabilities of this investigation.

Chapter 6

Corbino disks in a transversal magnetic field

In this chapter we investigate how a constant magnetic field B normal to the thin-film sample acts upon current filamentation in the Corbino geometry.

In earlier theoretical work both HÜPPER [Hüp93c, Hüp93a] and CHRISTEN [Chr94b] obtained a transversal motion of current filaments under the influence of a perpendicular magnetic field. KUNIHIO used a spatially two-dimensional numerical simulation to investigate current filamentation in a sample with two point contacts under a constant magnetic field B normal to the surface [Kun96a, Kun97a, Kun97b]. He found an asymmetric broadening of the filament. Experimentally, stationary bent filaments [Hir97c, Kli99, Hir00] as well as relaxation oscillations [Hir97b, Hir97e, Hir98, Aok99a] of a filament between two point contacts were observed. In the latter case a filament nucleates between the contacts and bends due to the Lorentz force exerted by the transversal magnetic field. The resulting elongation leads to a reduction of the electric field \mathcal{E} within the filament that extinguishes when \mathcal{E} drops below the holding field. The process then starts over again. That mechanism can result in complex oscillation scenarios. In a sample with two parallel stripe contacts the visualization of a current filament has been used to directly measure the Hall angle and determine the carrier mobility from it [Nov97b, Nov98a, Hir99].

In the Corbino disk geometry under the influence of a normal magnetic field of the order of $B = 100$ mT stationary bent filaments as well as filaments rotating with a frequency of several 10 kHz were observed [Mar96, Ebe97a, Hir97e, Nie98, Hir99, Hir00]. For a magnetic field *parallel* to the surface of a thin-film Corbino disk AOKI and FUKUI observed a broadening of the filaments for the case where the Lorentz force is directed towards the sample surface and an extinction of those filaments where the Lorentz force points in the direction of the substrate [Aok99b].

In Fig. 6.1 photoluminescence measurements of two different Corbino samples ((a) – (d) and (e) – (h), respectively) subject to a perpendicular magnetic field are shown for several different values of the total current I . As already observed in chapter 5 the number of filaments in both samples increases with rising I . Here however, each filaments exhibits a bending due to the

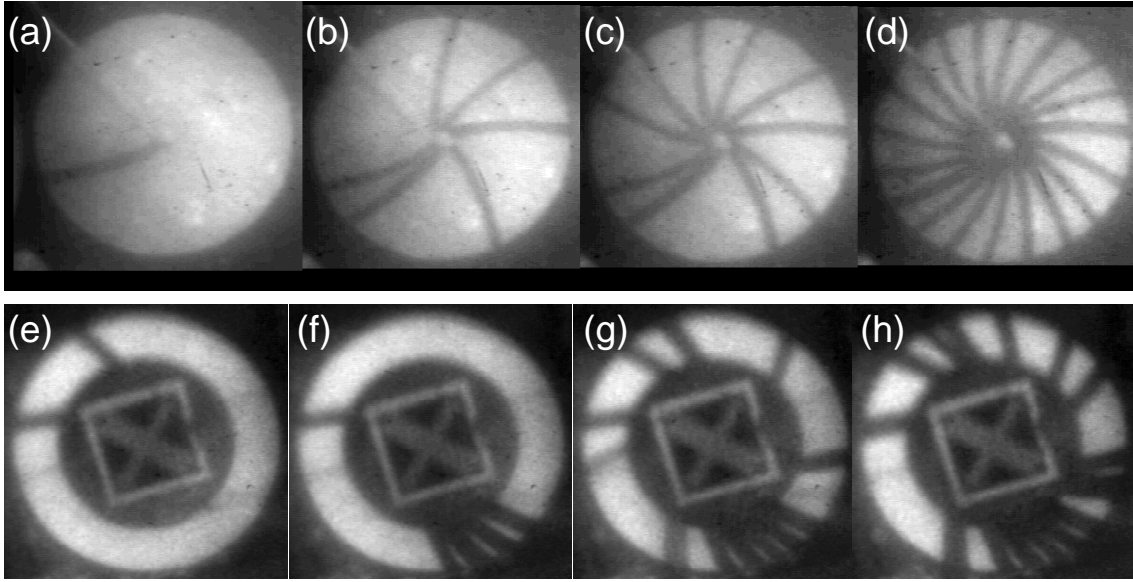


Figure 6.1: Experimental photoluminescence images of current filaments in two different Corbino disks at different bias voltages subject to a perpendicular magnetic field B ((a) – (d): inner contact radius 0.04 mm, outer contact radius 1.05 mm, magnetic field $B = 152$ mT; (e) – (h): inner contact radius 1.0 mm, outer contact radius 1.5 mm, magnetic field $B = 237$ mT; thickness of the epitaxial layer $3.0 \mu\text{m}$). Total current through the sample: (a): 0.2 mA, (b): 1.1 mA, (c): 1.7 mA, (d): 3.3 mA, (e): 0.7 mA, (f): 1.9 mA, (g): 4.4 mA, (h): 5.9 mA. (from [Hir00])

Lorentz force.

In order to take into account the effect of a perpendicular magnetic field \underline{B} in the simulations the expression for the current density \underline{j} has to be modified [Kun97a]:

$$\underline{j} = \frac{\underline{j}_0 + \mu \underline{B} \times \underline{j}_0}{1 + |\mu \underline{B}|^2}. \quad (6.1)$$

Here \underline{j}_0 is the current density in the case of absence of an external magnetic field as in eq. (2.8). The calculated temporal evolution of a filament in a Corbino disk with contact radii $R_1 = 0.2$ mm and $R_2 = 1.05$ mm and an applied voltage of $U_0 = 1.95$ V is depicted in Figs. 6.2 (a) through (h) for different values of B . For comparison Figs. 6.2 (a_1) – (a_3) show the case with no magnetic field ($B = 0$): several streamers develop into pre-filaments, one of which subsequently emerges as the winner of the competition mediated by the global coupling.

With an additional perpendicular magnetic field present, that basic process still holds. With increasing B however, we observe that the radially expanding streamers already start to get more and more twisted around the central contact as an effect of the Lorentz force acting on them. The subsequent pre-filaments that extend between the two contacts on the other hand are

only slightly bent. One explanation could be that the current flow favors a short path between the two contacts. We also observe that with increasing magnetic fields the process of filament formation gets notably faster, and for sufficiently high B the first streamer to hit the outer electrode already carries that much current that the other ones immediately start to recombine (note that the current density snapshots are taken at different times t for different B).

Once a fully developed filament has formed it starts to broaden in the direction of the Lorentz force. That azimuthal expansion is the faster the higher the applied magnetic field. The broadening of the filament is brought about by the shift of the one filament wall (on the side to which the Lorentz force points) into the adjacent low-conducting sample region, while the opposite wall remains in place. That behavior is different from the results of one-dimensional simulations of a filament under the influence of a perpendicular magnetic field where both walls have been found to move in the direction given by the Lorentz force [Hüp93c, Hüp93a], but similar to the asymmetric widening of filaments found by KUNIHIRO for two point contacts [Kun96a, Kun97b, Kun97a]. As in chapter 5 one might speculate whether this is an effect of the boundary conditions at the contacts, which in a spatially one-dimensional simulation cannot be taken into account.

In Fig. 6.3 four different sequences (a) through (d) of filament formation in a Corbino disk with radii $R_1 = 0.2$ mm, $R_2 = 1.05$ mm are shown for different combinations of the directions of the applied bias U_0 and of the perpendicular magnetic field B . We see that the direction of the twisting of the streamers as well as the bending and expansion of the subsequently remaining filament depends on the sign of both U_0 and B . This is expected since the Lorentz force is linear in both the magnetic field and in the velocity of the carriers. That result corresponds to measurements of the bending of a current filament in a Corbino disk under the influence of an applied voltage and a magnetic field normal to the sample surface, which also depends on the sign of both of them (Fig. 6.4).

That latter comparison, however, also points out a seemingly significant discrepancy between the results of the experiments and of the simulations. While in experiments stable bent filaments are observed in a Corbino sample under the influence of a magnetic field, in all simulations a newly created filament has been found to expand in direction of the Lorentz force. We try to resolve that problem by considering a longer simulation of that transient process, which is depicted in Fig. 6.5. Again, after the evolution of a single, fully developed filament its one boundary azimuthally expands into the direction of the Lorentz force while the opposite one remains pinned. The “leading” boundary starts circling around the central contact sweeping into the low-conducting region of the sample (Figs. 6.5 (e) – (i)). With expanding area of the filament its current density on the trailing side declines significantly but is still higher than in the rest of the Corbino disk.

Within about 23 ns the leading boundary has completed one full circle, hitting the pinned back of the filament, which brings it to a stop. Since in a narrow region directly behind the boundary the current density is still of the order found in a corresponding filament without magnetic field we again have a narrow high conducting channel embedded in a region of significantly lower conductivity (Figs. 6.5 (j) – (l)).

Whether or not that filament actually remains stable over much longer timescales, or whether

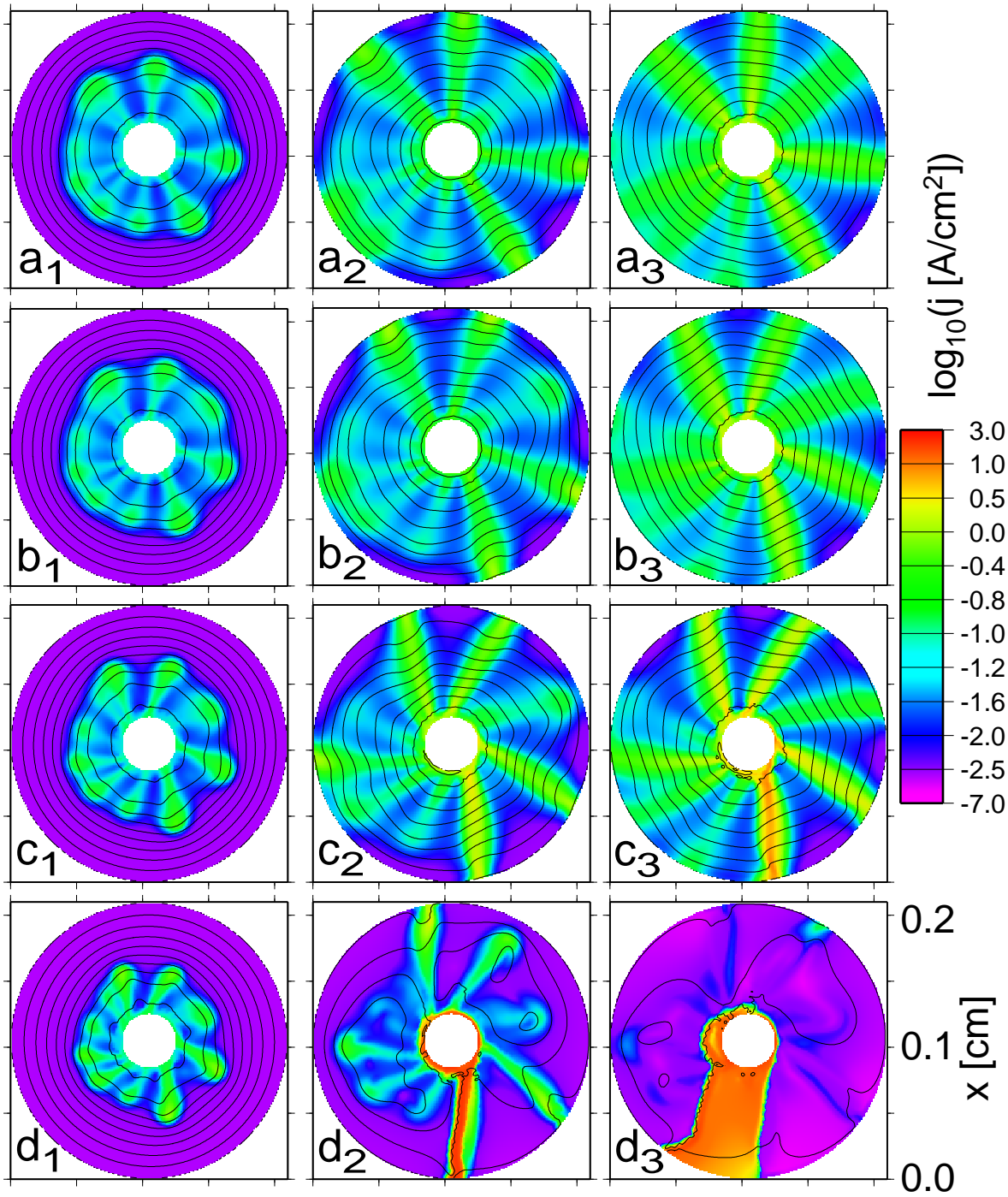


Figure 6.2: Temporal evolution of a current filament in a Corbino disk of radii $R_1 = 0.2$ mm, $R_2 = 1.05$ mm under different orientation of bias $U_0 = 1.95$ V and perpendicular magnetic field B of different strength: $a_1 - a_3$: without magnetic field ($B = 0$); $b_1 - b_3$: $B = 30$ mT; $c_1 - c_3$: $B = 50$ mT; $d_1 - d_3$: $B = 90$ mT. a_1 : $t = 8.9 \cdot 10^{-10}$ s, a_2 : $t = 1.4 \cdot 10^{-9}$ s, a_3 : $t = 2.0 \cdot 10^{-9}$ s, b_1 : $t = 8.9 \cdot 10^{-10}$ s, b_2 : $t = 1.4 \cdot 10^{-9}$ s, b_3 : $t = 2.0 \cdot 10^{-9}$ s, c_1 : $t = 8.2 \cdot 10^{-10}$ s, c_2 : $t = 1.5 \cdot 10^{-9}$ s, c_3 : $t = 2.0 \cdot 10^{-9}$ s, d_1 : $t = 7.3 \cdot 10^{-10}$ s, d_2 : $t = 1.2 \cdot 10^{-9}$ s, d_3 : $t = 2.0 \cdot 10^{-9}$ s. Equipotential lines are spaced by 0.2 V. (continued on the next page)

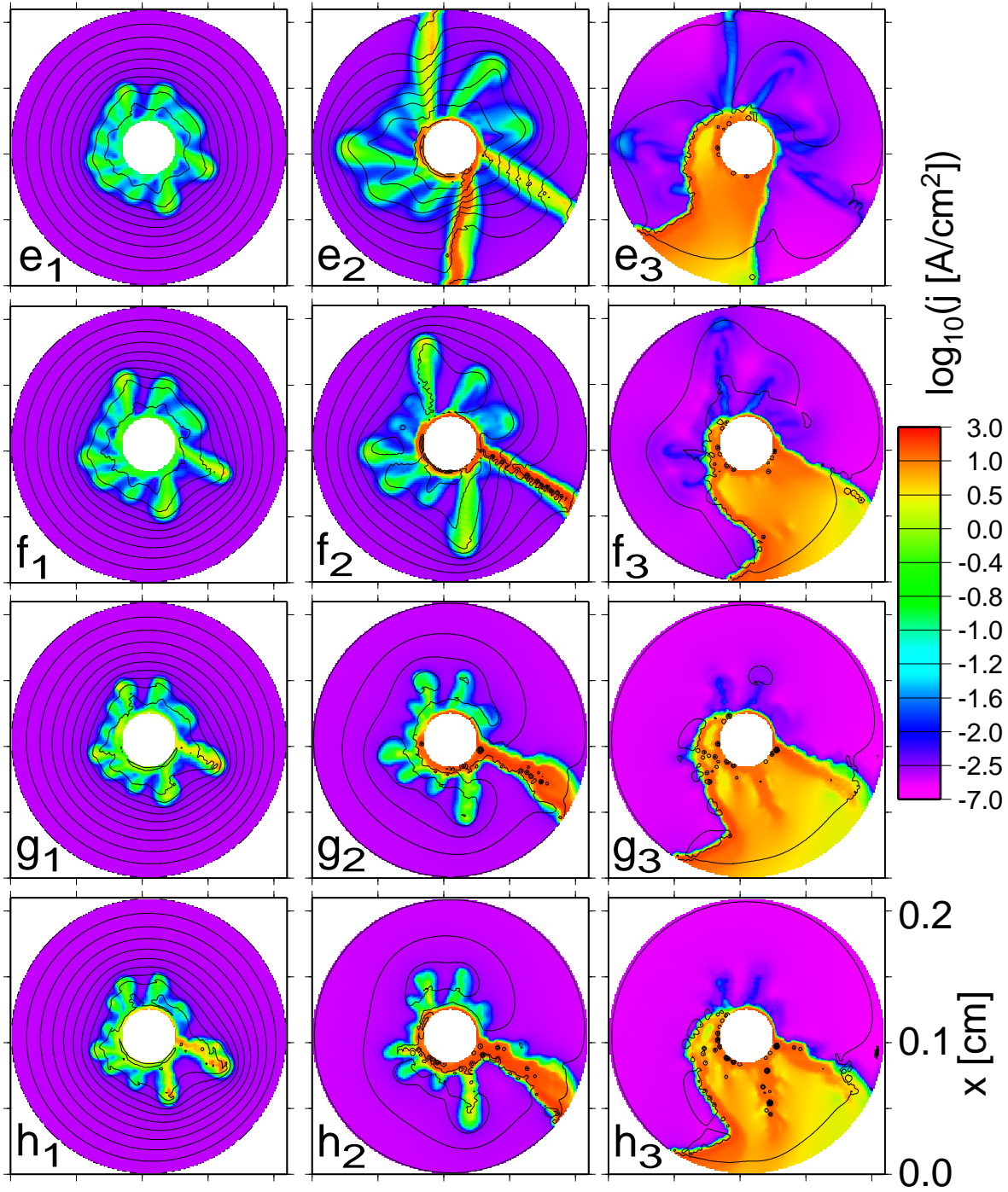


Figure 6.2: Temporal evolution of a current filament in a Corbino disk of radii $R_1 = 0.2$ mm, $R_2 = 1.05$ mm under different orientation of bias $U_0 = 1.95$ V and perpendicular magnetic field B of different strength: $e_1 - e_3$: $B = 125$ mT; $f_1 - f_3$: $B = 150$ mT; $g_1 - g_3$: $B = 200$ mT; $h_1 - h_3$: $B = 250$ mT. e_1 : $t = 5.6 \cdot 10^{-10}$ s, e_2 : $t = 1.1 \cdot 10^{-9}$ s, e_3 : $t = 2.0 \cdot 10^{-9}$ s, f_1 : $t = 6.4 \cdot 10^{-10}$ s, f_2 : $t = 8.8 \cdot 10^{-10}$ s, f_3 : $t = 2.0 \cdot 10^{-9}$ s, g_1 : $t = 4.8 \cdot 10^{-10}$ s, g_2 : $t = 6.4 \cdot 10^{-10}$ s, g_3 : $t = 2.0 \cdot 10^{-9}$ s, h_1 : $t = 4.4 \cdot 10^{-10}$ s, h_2 : $t = 5.6 \cdot 10^{-10}$ s, h_3 : $t = 2.0 \cdot 10^{-9}$ s. Equipotential lines are spaced by 0.2 V. (continued from previous page)

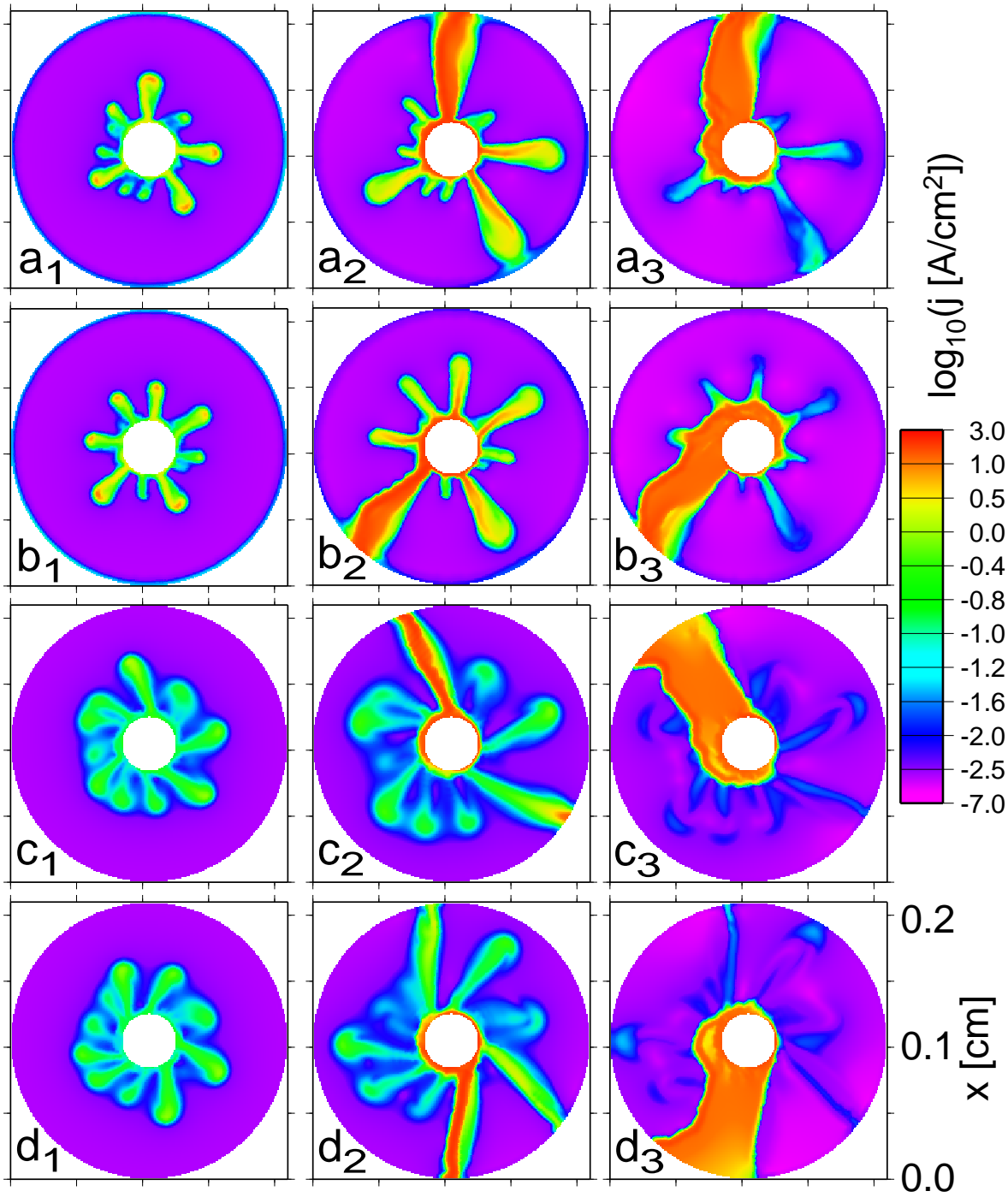


Figure 6.3: Temporal evolution of a current filament in a Corbino disk of radii $R_1 = 0.2$ mm, $R_2 = 1.05$ mm under different orientation of bias $U_0 = \pm 1.95$ V and perpendicular magnetic field $B = \pm 100$ mT: a): $U_0 < 0$ (central contact is anode), $B < 0$; b): $U_0 < 0$, $B > 0$; c): $U_0 > 0$ (central contact is cathode), $B < 0$; d): $U_0 > 0$, $B > 0$. a_1 : $t = 4.0 \cdot 10^{-10}$ s, a_2 : $t = 6.0 \cdot 10^{-10}$ s, a_3 : $t = 1.00 \cdot 10^{-9}$ s, b_1 : $t = 4.0 \cdot 10^{-10}$ s, b_2 : $t = 6.0 \cdot 10^{-10}$ s, b_3 : $t = 1.00 \cdot 10^{-9}$ s, c_1 : $t = 7.6 \cdot 10^{-10}$ s, c_2 : $t = 1.16 \cdot 10^{-9}$ s, c_3 : $t = 1.84 \cdot 10^{-9}$ s. d_1 : $t = 7.6 \cdot 10^{-10}$ s, d_2 : $t = 1.24 \cdot 10^{-9}$ s, d_3 : $t = 2.00 \cdot 10^{-9}$ s,

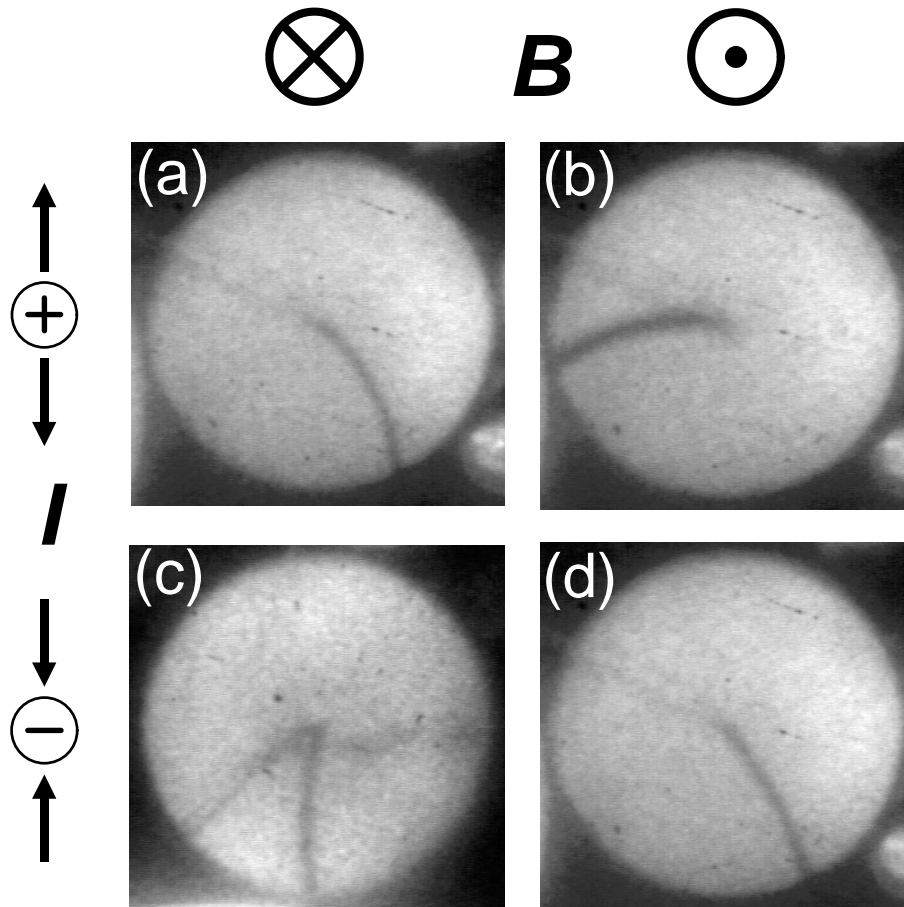


Figure 6.4: Experimental photoluminescence images of a current filament in a Corbino disk sample for different orientations of the perpendicular magnetic field B and electric polarity (inner contact radius 0.04 mm, outer contact radius 1.05 mm, magnetic field $B = 152$ mT, thickness of the epitaxial layer $3.0 \mu\text{m}$). (a): total current $I = 0.11$ mA, $B = -170$ mT, (b): $I = 0.20$ mA, $B = 170$ mT, (c): $I = -0.13$ mA, $B = -77$ mT. (d): $I = -0.11$ mA, $B = 100$ mT. (from [Hir00])

it might start circling around the central contact would require even much longer simulation times to determine. Since the oscillation frequencies for rotating filaments in a Corbino sample observed experimentally are of the order of 10 kHz, i. e. one cycle takes about $100\ \mu\text{s}$, one presently cannot hope to resolve that process with the simulation methods used here.

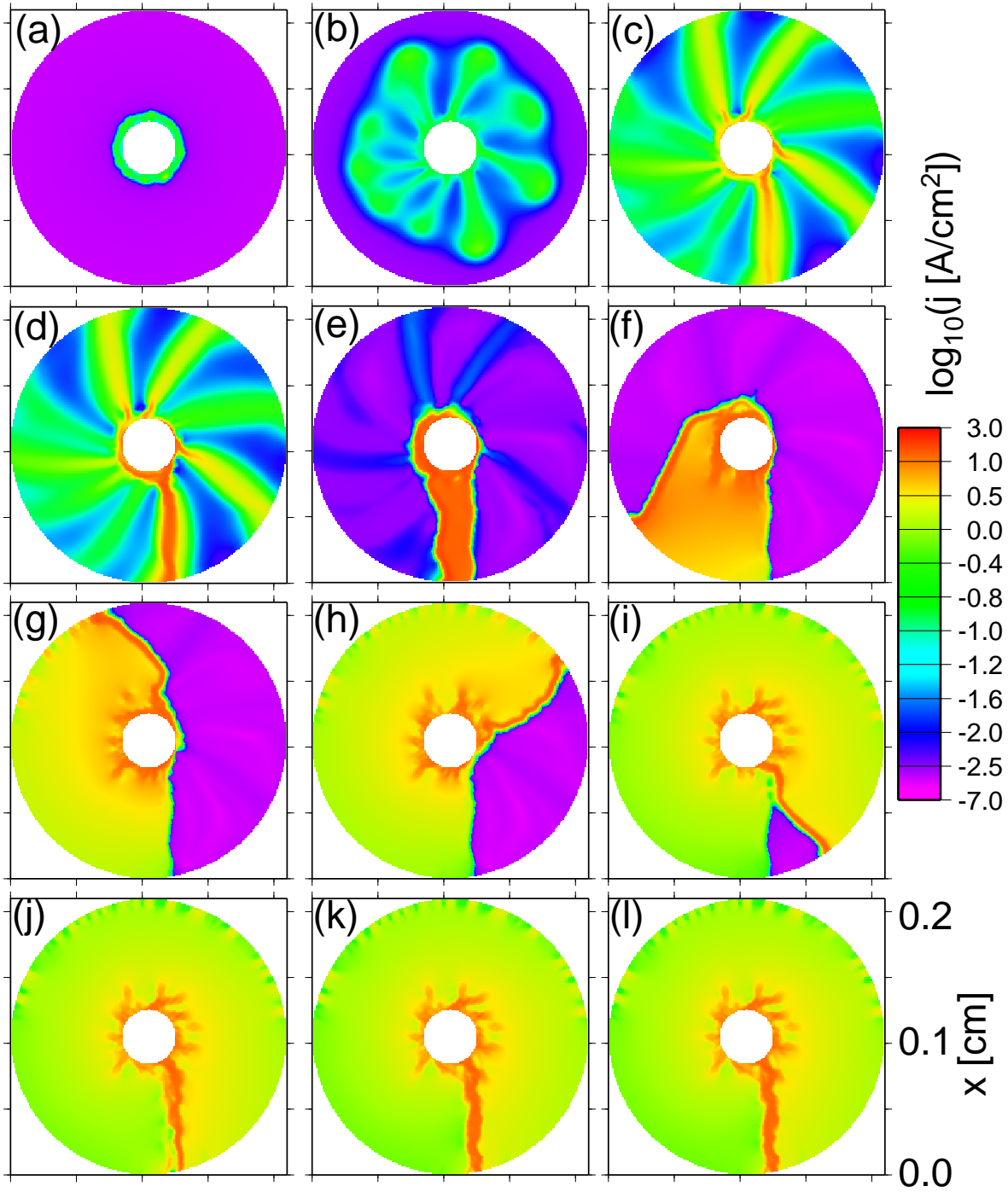


Figure 6.5: Nascence of a current filament in a Corbino disk sample with radii $R_1 = 0.2$ mm, $R_2 = 1.05$ mm with bias voltage $U_0 = 2.05$ V under the influence of a magnetic field $B = 50$ mT normal to the thin-film sample surface: (a): $t = 0.07$ ns, (b): $t = 0.98$ ns, (c): $t = 1.89$ ns, (d): $t = 2.24$ ns, (e): $t = 2.80$ ns, (f): $t = 4.90$ ns, (g): $t = 10.0$ ns, (h): $t = 16.0$ ns, (i): $t = 23.8$ ns, (j): $t = 26.3$ ns, (k): $t = 31.0$ ns, (l): $t = 35.0$ ns.

Chapter 7

Conclusions

In this work the process of current filamentation based on the low-temperature impurity breakdown in n-doped GaAs has been theoretically investigated for thin-film samples with two concentric circular contacts, so-called *Corbino disks*. The research had been motivated by spatially-resolved measurements of current density pattern formation in such samples by PRETTL and coworkers. The formation process of a current filament, i. e. a channel of high current density embedded in region of low conductivity, has been resolved with the help of numerical simulations based on a rate equation model for the generation-recombination processes of the electrons which gives rise to an S-shaped stationary current density-field relation. In the calculations the results of a Monte Carlo simulation of the microscopic scattering processes for the respective material system have been used as expressions for the generation-recombination coefficients. The constitutive dynamical semiconductor equations have been solved on a two-dimensional spatial domain using a sophisticated numerical finite elements code.

It was found that the formation of a current filament in a Corbino disk occurs as a multi-stage process: initially, a radially symmetric impact ionization front forms at the central contact where the field is the highest due to the geometry of the sample. It subsequently expands towards the outer ring electrode, acquiring more and more an azimuthal modulation. It dissolves into a number of finger-like current density structures which head towards the outer contact. Upon reaching it those “streamers”, as we have come to call them due to their geometrical and conceptional similarity to respective transient structures known in a variety of other systems, each constitutes a pre-filament as it had previously been observed in numerical simulations of current filamentation in samples with two point contacts. As a result of the global coupling via the external circuit a process of competition between the pre-filaments sets in. We have found a “winner-takes-all” dynamics where one pre-filament prevails and grows to a fully-developed filament, while the remaining ones decay. In the Corbino geometry the nucleation of a filament constitutes a symmetry breaking process and therefore represents a qualitatively different degree of self-organization than in previously investigated samples with two point contacts.

We have investigated the propagation mechanism of the impact ionization front whose velocity is significantly faster than the single carrier drift velocity and have demonstrated that it inherently relies on the finite radius of the sample as well as on the circular geometry which gives

rise to a monotonically descending radial electric field profile even in the electrically neutral state. Due to screening of the electric field by free electrons created through impact ionization around the peak of the field distribution the part of the sample across which the applied voltage drops steadily shrinks, resulting in a motion of the field profile towards the outer electrode. It is that mechanism of propagation that justifies our choice of the term “streamers” for the finger-shaped current density patterns which evolve out of the propagating impact ionization front¹. While a qualitative argument for the instability of that radially symmetric front with respect to azimuthal fluctuations has been given it turned out that due to the importance of the monotonically descending radial field profile a respective linear stability analysis around a homogeneous state does not yield any mode selection mechanism that would explain the specific number of streamers observed in the simulations.

It was not until very recently that, inspired by our contribution at the HCIS-11 conference, Kyoto 1999 [Sch99b], the transient process of filament formation has actually been observed experimentally in a Corbino disk GaAs sample by AOKI [Aok01b, Aok01a]. Using triggered imaging of quenched photoluminescence it was possible to identify five pre-filaments, three of which subsequently developed into full stable filaments. The same technique has previously been used by that author to experimentally resolve the nucleation process of a single filament between two point contacts [Aok98]. In those experiments a significantly longer nucleation time was observed than in the two-dimensional numerical simulations. Whether this indicates a quantitative weakness of the model or of the generation-recombination parameters would require further independent measurements to assess.

One interesting phenomenon found both in the experiment and in the simulations of the low temperature impact ionization regime in doped GaAs Corbino disks is the occurrence of a multistable global current-voltage characteristic based on a simple bistable microscopic current density-field relation. In this respect current filamentation in GaAs bears a lot of similarity to sequential tunneling through semiconductor multi quantum well structures, which is governed by an N-shaped (thus also bistable) local current density-field relation, but in a certain voltage regime, though domain formation, can lead to a multistable global current-voltage relation, too [Pre94, Kas94, Ama01]. There, however, multistability is brought about by the fact that the space charge that forms the wall between the two electric field domains can be centred in a quantum well at different locations for a given total voltage. The global current-voltage characteristic is thus closely related the spatial discretization and artificial periodicity of the sample (and in fact, the measured global current-voltage characteristic in turn can be used as a probe of the specific microscopic structure of a sample, identifying local deviations from periodicity [Sch96b, Sch96a, Sch98b]).

In contrast, multistability in GaAs Corbino disks is not guided by any spatial constraints in the sample but is an effect of self-organization which results from the different number of stable current filaments that can form and coexist for a given total current through the Corbino sample. Our simulations of current filamentation in a Corbino sample subject to a quasi-static bias ramp have yielded the consecutive nucleation of multiple stable filaments, in good agreement with experimental results. In the global current-voltage characteristic each additional filament ap-

¹Some authors in literature even use that term for a corresponding planar front as well.

pearing with rising bias manifests itself by a discontinuity because of the spontaneous increase of the total current and the resulting drop of the sample voltage due to the load resistance. In the simulations new filaments have been found to always appear through a nucleation process, while there is experimental evidence that a splitting process of an already existing filament should take place at least in some cases. A possible explanation might be an insufficient numerical treatment of the boundary conditions representing the contacts. For a descending voltage ramp we have found a hysteretic behavior.

In simulations involving an additional external magnetic field normal to the sample surface a twisting of the expanding streamers around the central contact due to the Lorentz force has been observed. It was found that the presence of a magnetic field accelerates the process of competition among the different pre-filaments. One boundary of the fully-developed filament under the influence of the perpendicular magnetic field starts to move in azimuthal direction around the central contact, expanding the filament until that boundary hits the back of the filament and it covers the entire Corbino sample. However, since that process happens on a nanosecond time scale it should not be relevant to experimental observation. After cycle one has been completed we again find one channel of significantly higher conductivity than in the rest of the sample since the current density in the inner regions of the filament has dropped as a result of its spatial expansion. Our simulation times have not been sufficiently long to assess whether that structure remains stable or even might start rotating on the much slower time scales expected from corresponding experiments.

In summary, the numerical simulations have been successful in reproducing and explaining many of the effects observed experimentally, such as the spontaneous symmetry breaking by the nucleation of a filament in a sample with Corbino geometry, as well as multistability and hysteresis in the current-voltage characteristic. Those results demonstrate the general applicability of the underlying simple generation-recombination model for an appropriate description of the phenomena of self-organization and pattern formation in doped GaAs thin-film samples at low temperatures. For a better comparison of some effects a more refined modeling of some of the sample details such as the treatment of the contacts might be required.

Although both the experimental and the theoretical investigation of current filamentation in doped thin-film GaAs samples have been aimed towards the study of the basic phenomena of pattern formation some of the findings might hold a potential for application. A system exhibiting multistability can, in principle, be used to build a data storage device which can hold more than one bit of information within a single “memory element”. The advantage over a comparable bistable, i.e. binary, memory device is a higher storage density and thus potentially faster switching time due to shorter signaling paths. Because of the comparably long nascence and extinction times of the filaments and the rather large size of the samples, let alone the requirement of very low temperatures for impact ionization to dominate over thermal excitation, GaAs Corbino samples can of course by no means be expected to become a match to existing, well established memory technology.

A probably more promising feature for application is the superfast impact ionization front. In fact, in other semiconductor devices such as Silicon diodes that phenomenon is used to achieve sharpening of pulse signals and to build fast electrical power switches. Streamers on the other

hand have come to interest in recent years in the growing field of environmental pollution control technology: there superfast impact ionization streamers in gases are used to quickly produce a high amount of energetic electrons which generate active radicals that can suitably react with pollutants rendering them intoxic [Vit93]. The efficiency of those processes have turned out to highly depend on the details of the streamers' shapes, which are thus subject of ongoing research.

Acknowledgements

I would like very much to thank Prof. Eckehard Schöll for not only supervising this research work but moreover for the extensive discussions on the subject of pattern formation we had had as well as for his countless hints and suggestions, while at the same time leaving me the freedom to pursue ideas of my own. I would like to acknowledge the excellent close collaboration with Prof. Wilhelm Prettl of Regensburg University and his group, particularly Dr. Jürgen Hirschinger, whose experimental work on current filaments in doped GaAs thin film samples provided the basis to this theoretical investigation. I am indebted to Prof. Herbert Gajewski and Dr. Reiner Nürnberg of Weierstraß Institute for Applied Analysis and Stochastics (WIAS) for providing the TeSCA simulation code and for their testing and the various corrections and improvements they have added to it in response to numerical problems that have surfaced during this research.

Both Dr. Vít Novák and Dr. Pavel Rodin, with whom I had had the pleasure of sharing office for some time, I would like to thank for the numerous interesting discussions I had had with each of them over the course of this research. I would like to add that the two symposia which Vít Novák had organized in Prague were of great benefit for the collaboration between the theoretical and experimental groups working on current filamentation in thin GaAs films.

I should also mention Dr. Franz-Josef Niedernostheide, who was the one to first introduce me to the experimental measurements of current filaments in Corbino disks, sparking my idea of the theoretical investigation of the processes in that sample geometry, and Dr. Ute Ebert, who brought my attention to the subject of streamers.

The collaboration with Carsten Lehmann, Jens Murawski and Axel Reimann on various aspects of current filaments in different contact geometries had been very pleasant and fruitful for this research. Last but not least I would like to thank my present and former colleagues at ITP, in particular Andreas Amann, Sumit Bose, Michael Gaa and Reinhard Wetzler, not only for the many valuable discussions on issues of pattern formation, semiconductor physics, computing, or numerics we had had but more generally for the good collaboration during the past years.

Funding for the computing resources, without which this research would not have been possible, was provided to a large extent by German Science Foundation (DFG) in the framework of Collaborative Research Centre (SfB) 555 “Complex Nonlinear Processes”.

Appendix A

Material parameters

The following material parameters were used in the simulation of current filamentation in n-GaAs [Gaa94, Gaa96b]:

material parameter	symbol	value
lattice temperature	T_L	4.2 K
donor concentration	N_D	$7 \cdot 10^{15} \text{ cm}^{-3}$
acceptor concentration	N_A	$2 \cdot 10^{15} \text{ cm}^{-3}$
effective impurity concentration	$N_D^* = N_D - N_A$	$5 \cdot 10^{15} \text{ cm}^{-3}$
relative dielectric constant	ϵ_r	10.9
electron mobility	μ	$10^5 \frac{\text{cm}^2}{\text{Vs}}$
diffusion constant	$D = \mu k_B T_L / e$	$36.2 \frac{\text{cm}^2}{\text{s}}$
load resistance	R_L	10 k Ω
sample thickness	d	3 μm

Appendix B

Analytical representations of the GR coefficients

The following analytical representations of the GR coefficients, which have been derived by GAA [Gaa94, Gaa95, Gaa96b] from the results of the Monte Carlo simulations for GaAs [Keh95], are used in the numerical simulations:

$$T_e^{up}(\mathcal{E}) = \frac{1}{\gamma_0} \left(a_1 + \frac{a_2}{1 + \exp(a_3 - a_4 \gamma_2 \mathcal{E})} + a_5 \gamma_2 \mathcal{E} \right) \quad (\text{B.1})$$

$$T_e^{lo}(\mathcal{E}) = \frac{1}{\gamma_0} \left(b_1 + \frac{b_2}{1 + \exp(b_3 - b_4 \gamma_2 \mathcal{E})} + b_5 \gamma_2 \mathcal{E} \right) \quad (\text{B.2})$$

$$X_1(T_e) = \gamma_3 c_1 \exp \left(\frac{c_2}{1 + \exp(c_3 - c_4 \gamma_0 T_e)} + c_5 \gamma_0 T_e \right) \quad (\text{B.3})$$

$$X_1^*(T_e) = \gamma_3 d_1 \exp \left(\frac{d_2}{1 + \exp(d_3 - d_4 \gamma_0 T_e)} + d_5 \gamma_0 T_e \right) \quad (\text{B.4})$$

$$T_1^{Sup}(T_e) = \gamma_3 e_1 \exp(e_2(\gamma_0 T_e - e_4)^{e_3}) \quad (\text{B.5})$$

$$T_1^{Slo}(T_e) = \gamma_3 f_1 \exp(f_2(\gamma_0 T_e)^{f_3}) \quad (\text{B.6})$$

with the following parameters

	$i = 1$	$i = 2$	$i = 3$	$i = 4$	$i = 5$
a_i	2.336	18.111	2.896	140.5	57.967
b_i	3.417	1.689	6.098	678.9	63.191
c_i	$1.161 \cdot 10^{-5}$	6.687	5.928	0.694	$6.104 \cdot 10^{-2}$
d_i	$7.530 \cdot 10^{-3}$	0.458	4.657	1.030	$2.836 \cdot 10^{-2}$
e_i	$4.979 \cdot 10^{-6}$	9.726	-0.278	2.143	
f_i	$6.138 \cdot 10^{-3}$	-0.265	1.254		

and scaling parameters $\gamma_0 = 1/T_L = 0.238 \text{ K}^{-1}$, $\gamma_2 = 1/54810.0 \frac{\text{m}}{\text{V}}$, $\gamma_3 = 2.554 \cdot 10^{-9} \frac{\text{m}^3}{\text{s}}$.

For numerical reasons the Heaviside functions Θ have been approximated by smooth functions:

$$\begin{aligned}
T_e(n, \mathcal{E}) &= \Theta(n - n_{th}) T_e^{up}(\mathcal{E}) + \Theta(n_{th} - n) T_e^{lo}(\mathcal{E}) \\
&\approx \frac{1}{2} \left[\left(T_e^{up}(\mathcal{E}) + T_e^{lo}(\mathcal{E}) \right) + \tanh(\log_{10}(n/n_{th})) \left(T_e^{up}(\mathcal{E}) - T_e^{lo}(\mathcal{E}) \right) \right] \quad (\text{B.7}) \\
T_1^S(n, T_e) &= \Theta(n - n_{th}) T_e^{up}(T_e) + \Theta(n_{th} - n) T_e^{lo}(T_e) \\
&\approx \frac{1}{2} \left[\left(T_1^{Sup}(T_e) + T_1^{Slo}(T_e) \right) + \tanh(\log_{10}(n/n_{th})) \left(T_1^{Sup}(T_e) - T_1^{Slo}(T_e) \right) \right] \quad (\text{B.8})
\end{aligned}$$

with a threshold value for the free electron density $n_{th} = 0.1 N_D^*$.

The remaining three GR coefficients are treated as constants: $X_1^S = 1.17 \cdot 10^6 \text{ s}^{-1}$, $X^* = 3.36 \cdot 10^3 \text{ s}^{-1}$, $T^* = 4.10 \cdot 10^7 \text{ s}^{-1}$.

Appendix C

Calculation of the steady state

One important property of the two-level rate equation model for low temperature impact ionizations from shallow impurities derived by SCHÖLL [Sch87] is the fact that none of the generation-recombination coefficients depends on the carrier concentration in the impurities, n_1 and n_2 . This can be used to directly calculate the steady-state expressions for those concentrations as functions of the local free electron density n and electric field \mathcal{E} (the dependence of the dynamic variables on time and space is being omitted here for brevity).

With the formal vector $\underline{n}_t = (n_1 \ n_2)^T$ eqs. (2.2), (2.5), (2.6) can be written as

$$\begin{aligned} \dot{\underline{n}}_t &= \begin{pmatrix} \phi_1 \\ \phi_2 \end{pmatrix} \\ &= \begin{pmatrix} -X^* - X_1 n & T^* \\ -T_1^S n + X^* & -X_1^S - T_1^S n - X_1^* n - T^* \end{pmatrix} \begin{pmatrix} n_1 \\ n_2 \end{pmatrix} + \begin{pmatrix} 0 \\ T_1^S n N_D \end{pmatrix} \\ &:= \underline{\underline{B}} \underline{n}_t + \underline{c}. \end{aligned} \tag{C.1}$$

$\underline{\underline{B}}$ and \underline{c} are functions of n and \mathcal{E} . Eq. C.1 can be solved for the steady-state solution of \underline{n}_t , \underline{n}_t^{st} , by inverting $\underline{\underline{B}}$:

$$\underline{n}_t^{st} = -\underline{\underline{B}}^{-1} \underline{c} = \frac{T_1^S n N_D}{\det \underline{\underline{B}}} \begin{pmatrix} T^* \\ X^* + X_1 n \end{pmatrix}. \tag{C.2}$$

One thus obtains an analytical expression for the steady state charge density $\rho = e(N_D^* - n_1(n, \mathcal{E}) - n_2(n, \mathcal{E}) - n)$ as a function of n and \mathcal{E} , which serve as parameters in this local steady state analysis of the generation-recombination terms. The roots of $\rho(n, \mathcal{E})$ can be solved numerically in the \mathcal{E} - n plane (cf. Fig. 2.6).

Appendix D

A linear stability analysis

We present a linear stability analysis similar to the ones carried out in [Sch87] and [Gaa96e] for cylindrical filament breathing and longitudinal waves, respectively. We will start with the simpler one-dimensional case with one spatial coordinate z , which is the direction of the current flow, and subsequently see what is different in a two-dimensional circular geometry expressed by cylindrical coordinates r, ϕ .

Apart from the localized generation-recombination kinetics the two equations governing our system are Gauss's law (2.10), which links the local electric field to the local carrier concentrations, and the drift-diffusion equation (2.8), which defines the (particle) current density \underline{j} for the electrons. With the help of Maxwell's equation for the electric field \underline{H} , $\underline{\nabla} \times \underline{H} = -e\underline{j} + \epsilon \dot{\underline{E}}$, we arrive at the following expression for the total current density \underline{j}^{tot} defined as the sum of the conduction current density of the electrons and the Maxwellian displacement current density:

$$0 = \underline{\nabla} \cdot \underline{j}^{tot} = \underline{\nabla} \cdot (\epsilon \dot{\underline{E}} + en\mu\underline{E} + eD\underline{\nabla}n) . \quad (\text{D.1})$$

We now introduce small spatial fluctuations $\delta\underline{E}$, δn around a homogeneous steady state characterized by \underline{E}_0 , n_0 . For those fluctuations we assume proportionality to a factor $\exp(\Lambda t - ikz)$, with i being the imaginary unit. That ansatz expresses a damping (or a growth) and an oscillatory behavior of the fluctuations in time through the real and imaginary parts of Λ , respectively, as well as a longitudinal spatial modulation with wave number k . For the fluctuation of the total current density we obtain from eq. (D.1), which is already linear,

$$\begin{aligned} 0 &= \underline{\nabla} \cdot \delta\underline{j}^{tot} \\ &= \epsilon \underline{\nabla} \cdot \delta \dot{\underline{E}} + en_0\mu \underline{\nabla} \cdot \delta\underline{E} + e\underline{\nabla} \delta n \cdot \mu \underline{E}_0 + e\underline{\nabla} n_0 \cdot \mu \delta\underline{E} + e\delta n \mu \underline{\nabla} \cdot \underline{E}_0 + eD\Delta \delta n. \end{aligned} \quad (\text{D.2})$$

Since we are linearizing around a homogeneous state $\underline{\nabla} \cdot \underline{E}_0$ and $\underline{\nabla} n_0$ both vanish, and by carrying out the temporal derivative we arrive at

$$0 = (\epsilon\Lambda + en_0\mu) \underline{\nabla} \cdot \delta\underline{E} + e\mu\underline{E}_0 \cdot \underline{\nabla} \delta n + eD\Delta \delta n. \quad (\text{D.3})$$

As demonstrated in appendix C, the steady-state values of the trapped electron densities n_1 and n_2 can be expressed analytically as functions of n and \mathcal{E} . By linearizing those dependencies fluctuations in those two variables and thus fluctuations of the charge density, $\delta\rho$, can be expressed through $\delta\mathcal{E}$, δn [Sch87, Gaa96e]. A further simplification of the system can be obtained by directly considering the function $\rho(n, \mathcal{E})$ obtained for the steady state and using that in the linear stability analysis instead of the full generation-recombination kinetics. This approximation is equivalent to an assumption that n_1, n_2 adapt quickly, virtually instantaneously, to any changes in the local free electron density n and electric field \mathcal{E} , i. e. the dynamics of the donor electron densities is enslaved. Although that way the GR rates have formally been eliminated from the system their essence is now contained in the nonlinear function $\rho(n, \mathcal{E})$.

In that approximation one can write Gauss's law (2.10) for the fluctuations as

$$\epsilon \nabla \cdot \delta \underline{\mathcal{E}} = \delta \rho(n, \mathcal{E}) = \frac{\partial \rho}{\partial n} \delta n + \frac{\partial \rho}{\partial \mathcal{E}} \frac{\underline{\mathcal{E}}_0}{\mathcal{E}_0} \cdot \delta \underline{\mathcal{E}}. \quad (\text{D.4})$$

Here it was used that the GR coefficients and hence ρ do not depend on the direction but just on the strength of the electric field $\underline{\mathcal{E}}$.

Replacing $\delta \underline{\mathcal{E}}$ by the negative gradient of the electric potential fluctuation, $\delta \Psi$, and carrying out the spatial derivatives in eq. (D.4) we get

$$\epsilon k^2 \delta \Psi = \frac{\partial \rho}{\partial n} \delta n + \frac{\partial \rho}{\partial \mathcal{E}} \frac{\mathcal{E}_{0||}}{\mathcal{E}_0} ik \delta \Psi \quad (\text{D.5})$$

which can be solved for δn :

$$\delta n = \left(\frac{\partial \rho}{\partial n} \right)^{-1} \left(\epsilon k^2 - \frac{\partial \rho}{\partial \mathcal{E}} \frac{\mathcal{E}_{0||}}{\mathcal{E}_0} ik \right) \delta \Psi \quad (\text{D.6})$$

with $\mathcal{E}_{0||}$ the longitudinal component of $\underline{\mathcal{E}}_0$, i. e. the projection of $\underline{\mathcal{E}}_0$ on the unit vector in longitudinal direction.

Inserting this into (D.3) yields

$$\begin{aligned} (\epsilon \Lambda + en_0 \mu) k^2 \delta \Psi - e D k^2 \delta n - e \mu \mathcal{E}_{0||} ik \delta n &= 0 \\ (\epsilon \Lambda + en_0 \mu) k \delta \Psi - (e D k + i e \mu \mathcal{E}_{0||}) \delta n &= 0 \\ \left[(\epsilon \Lambda + en_0 \mu) - (e D k + i e \mu \mathcal{E}_{0||}) \left(\frac{\partial \rho}{\partial n} \right)^{-1} \left(\epsilon k - i \frac{\partial \rho}{\partial \mathcal{E}} \frac{\mathcal{E}_{0||}}{\mathcal{E}_0} \right) \right] k \delta \Psi &= 0 \end{aligned} \quad (\text{D.7})$$

and finally

$$\Lambda = -\frac{1}{\tau_M} + \left(\frac{\partial \rho}{\partial n} \right)^{-1} \left(e D k^2 + \frac{e \mu}{\epsilon} \frac{\partial \rho}{\partial \mathcal{E}} \mathcal{E}_0 \right) - ik \left(\frac{\partial \rho}{\partial n} \right)^{-1} \left(\frac{e D}{\epsilon} \frac{\partial \rho}{\partial \mathcal{E}} \frac{\mathcal{E}_{0||}}{\mathcal{E}_0} - e \mu \mathcal{E}_{0||} \right) \quad (\text{D.8})$$

with $\tau_M = \epsilon / (en_0 \mu)$ the Maxwellian relaxation time.

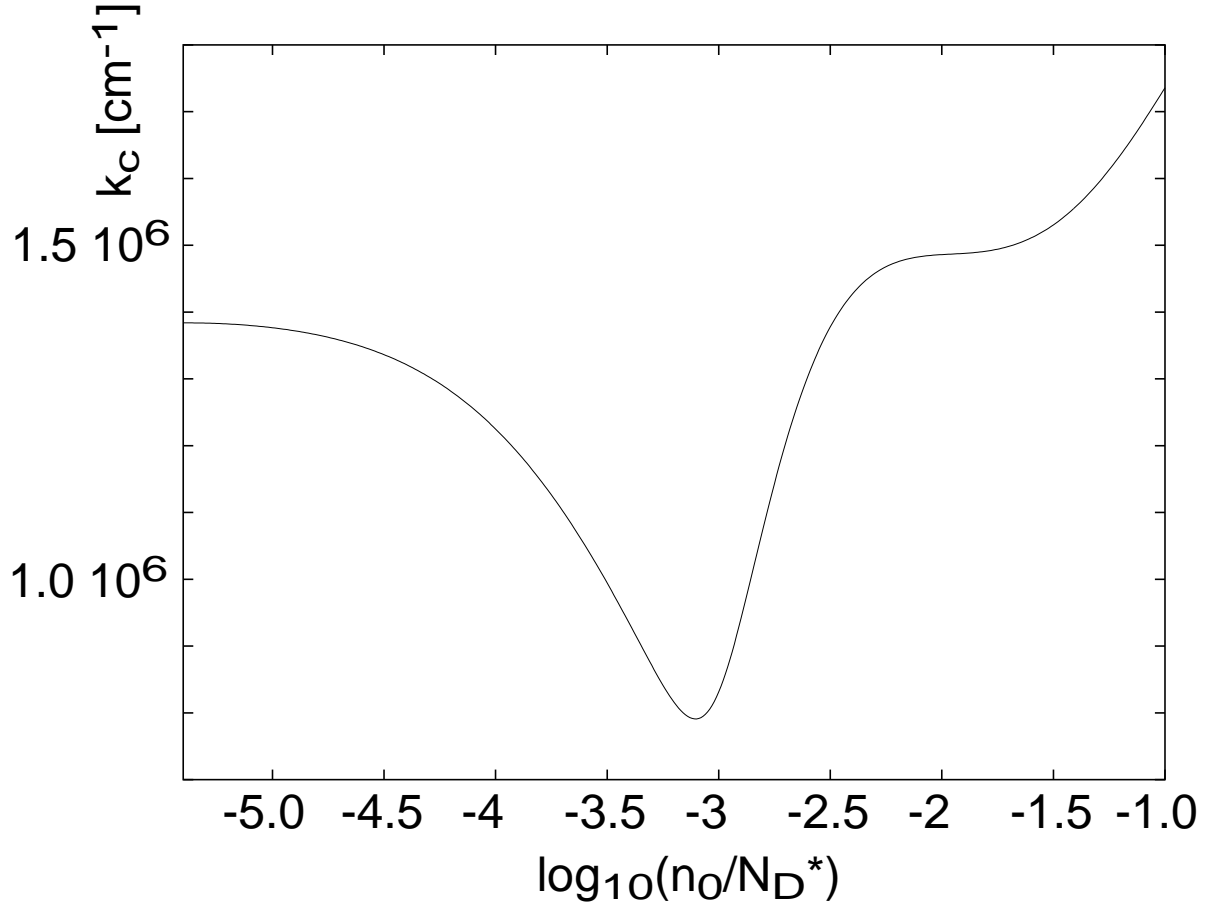


Figure D.1: Critical wave vector k_c above which the homogeneous state becomes unstable against respective longitudinal fluctuations as a function of the stationary free electron density n_0 .

We can split up Λ into a real and an imaginary part $\Lambda = \lambda + i\omega$. The system is linearly stable for $\lambda < 0$ and linearly unstable for $\lambda > 0$. Since for the given GR kinetics $\frac{\partial \rho}{\partial \mathcal{E}}$ is always non-negative, the sign of $\frac{\partial \rho}{\partial n}$ determines whether there exists a minimum wave number k_c so that $\lambda(k)$ becomes positive for $k > k_c$. The condition $\frac{\partial \rho}{\partial n} > 0$ for linear instability is met exactly on the negative differential intermediate branch of the stable \mathcal{E} - n characteristic (Fig. 2.6), which is expected from topological considerations as well¹. On the unstable branch, one finds that $\frac{\partial \rho}{\partial n} n_0$ is always greater than $\frac{\partial \rho}{\partial \mathcal{E}} \mathcal{E}_0$, thus

$$k_c = \sqrt{\frac{\mu}{D\epsilon} \left(\frac{\partial \rho}{\partial n} n_0 - \frac{\partial \rho}{\partial \mathcal{E}} \mathcal{E}_0 \right)}. \quad (\text{D.9})$$

¹the fact that in [Gaa96e] the region of instability extends somewhat into the positive differential conductivity branch is a result of considering the full dynamics of the trapped electron densities as well as an external capacity

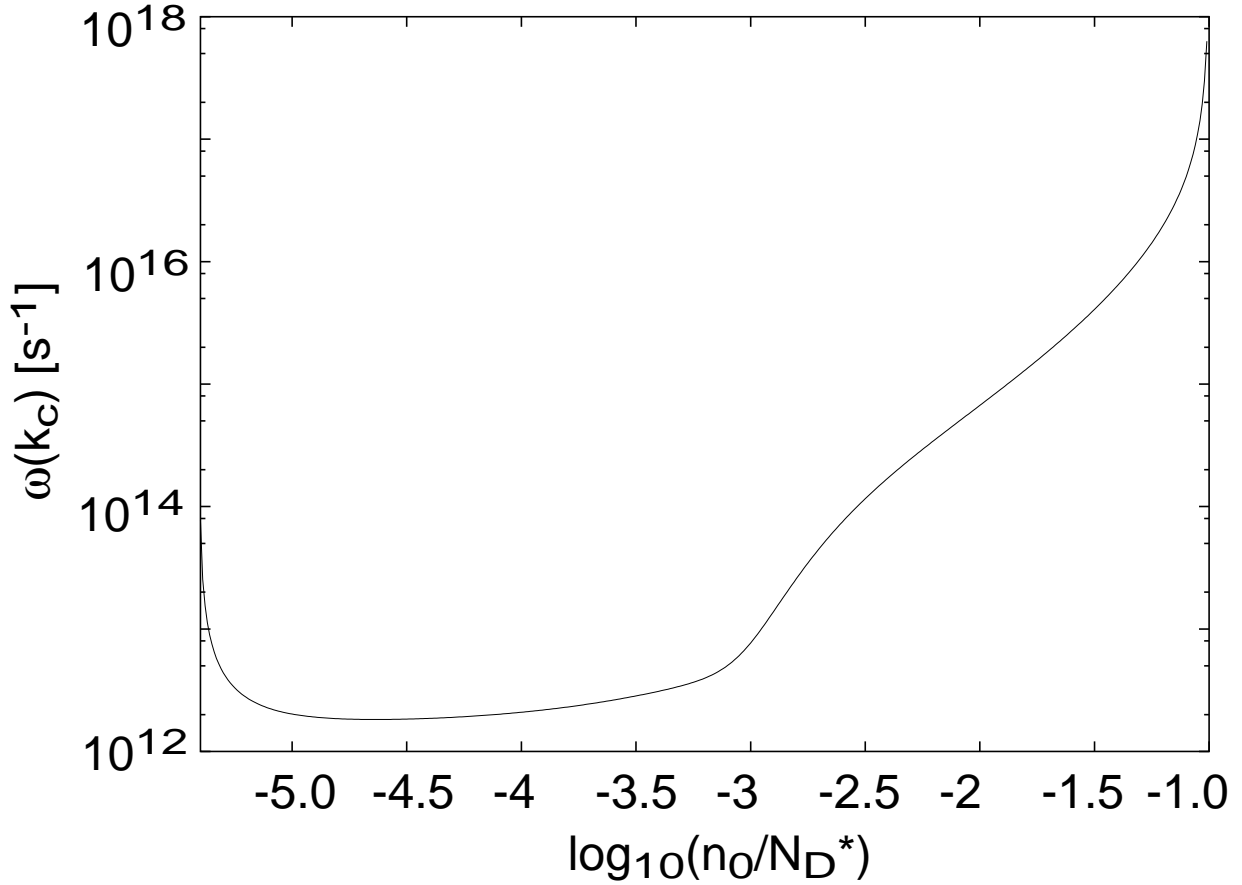


Figure D.2: Critical (angular) frequency $\omega(k_c)$ as a function of the stationary free electron density n_0 .

In Fig. D.1 the critical wave number k_c is drawn along the negative differential conductivity branch of the steady states parameterized by the free electron density n_0 . We find values of the order of 10^6 cm^{-1} . That value lies slightly below the upper edge of the range of instability for k that GAA had found in a comparable linear stability analysis for GaAs which did not eliminate the dynamics of the trapped electrons and included a field-dependent mobility μ [Gaa94, Gaa96e].

From eq. (D.8) one can directly read off the (angular) frequency (the imaginary part of Λ) at the critical wave number, $\omega(k_c)$, which is depicted in Fig. D.2. We read off a value of $5 \cdot 10^{15}$ to about 10^{16} s^{-1} . Those values are above the maximum $\omega(k_c)$ of about $3.4 \cdot 10^{12}$ obtained by GAA [Gaa94, Gaa96e], which is not surprising if one considers that $\omega(k)$ is linear in k and the values k_c obtained here are somewhat too high compared to the results of Refs. [Gaa96c, Gaa96e].

At the edges of the negative differential conductivity range corresponding to the holding and threshold fields, \mathcal{E}_h and \mathcal{E}_{th} , respectively, ω has poles because of the factor $\left(\frac{\partial p}{\partial n}\right)^{-1}$. This clearly shows that there the approximation of enslaving n_1, n_2 breaks down and that their dynamics plays an important role at those two transition points.

Unlike in the calculations by GAA [Gaa94, Gaa96e] this analysis yields no upper bound for k above which the system is stable again. This is not surprising if one considers that for large k the oscillations expressed through $\omega(k)$ will get very fast, thus rendering pointless the initial assumption of the donor concentration kinetics being adiabatically eliminated. As a check of consistency it should be mentioned that in (D.8) $\lambda(k)$ is an even (symmetric) function in both k and $\mathcal{E}_{||}$, whereas $\omega(k)$ is odd (asymmetric) in both k and $\mathcal{E}_{||}$.

In order to transfer those results to the case of a circular geometry we assume transversal, or more precisely azimuthal fluctuations $\delta n = \delta n(r) \exp(im\phi + \Lambda t)$ (and analogously for $\delta\Psi$)². Due to the circular condition in ϕ m must be an integer. Strictly speaking, there exists no homogeneous, electrically neutral stationary state since in cylindrical coordinates we get a $1/r$ dependence for the electric field, hence \mathcal{E} and the GR coefficients (or $\rho(n, \mathcal{E})$) differ along the sample radius³. If, however, the dependence of ρ on \mathcal{E} is weak we can neglect that effect and assume, as a stationary state to linearize about, a spatially constant n_0 . The condition of local charge neutrality $\rho(n_0, \mathcal{E}_0) = 0$ yields $\nabla \cdot \underline{\mathcal{E}}_0 = 0$, which in a radially symmetric geometry with eq. (2.10) gives

$$\frac{d\mathcal{E}_0}{dr} + \frac{\mathcal{E}_0}{r} = 0. \quad (\text{D.10})$$

Solving eq. (D.10) one obtains $\mathcal{E}_0(r) = \frac{c_0}{r}$. The integration constant c_0 is given by the sample voltage U as follows: since $U = \int_{R_1}^{R_2} \mathcal{E} dr$ must hold this yields $U = c_0 \ln(R_2/R_1)$, or

$$c_0 = \frac{U}{\ln(R_2/R_1)}. \quad (\text{D.11})$$

The ansatz of a spatially constant n_0 is consistent with the steady-state continuity equation, $0 = \nabla \cdot \underline{j} = n_0 \mu \nabla \cdot \underline{\mathcal{E}}$, since $\nabla \cdot \underline{\mathcal{E}} = 0$ holds.

We can solve eq. (D.4) for $\Delta\delta\Psi = -\nabla \cdot \delta\underline{\mathcal{E}}$ and insert that expression into eq. (D.2) (the two equations do not assume any specific coordinates). We obtain, after taking the temporal derivative,

$$\left(\Lambda + \frac{en_0\mu}{\varepsilon}\right) \frac{\partial\rho}{\partial n} \delta n + eD\Delta\delta n + e\mu\underline{\mathcal{E}}_0 \cdot \underline{\nabla}\delta n = 0. \quad (\text{D.12})$$

Inserting the specific expressions for cylindrical coordinates r, ϕ into eq. (D.12) we get

$$eD \left(\frac{\partial^2}{\partial r^2} + \frac{1}{r} \frac{\partial}{\partial r} - \frac{m^2}{r^2} \right) \delta n + e\mu \frac{c_0}{r} \frac{\partial}{\partial r} \delta n + \left(\Lambda + \frac{en_0\mu}{\varepsilon} \right) \frac{\partial\rho}{\partial n} \delta n = 0 \quad (\text{D.13})$$

and finally

$$\left[r^2 \frac{\partial^2}{\partial r^2} + \left(1 + \frac{\mu c_0}{D} \right) r \frac{\partial}{\partial r} + \left(\frac{\Lambda}{eD} + \frac{n_0\mu}{\varepsilon D} \right) \frac{\partial\rho}{\partial n} r^2 - m^2 \right] \delta n = 0. \quad (\text{D.14})$$

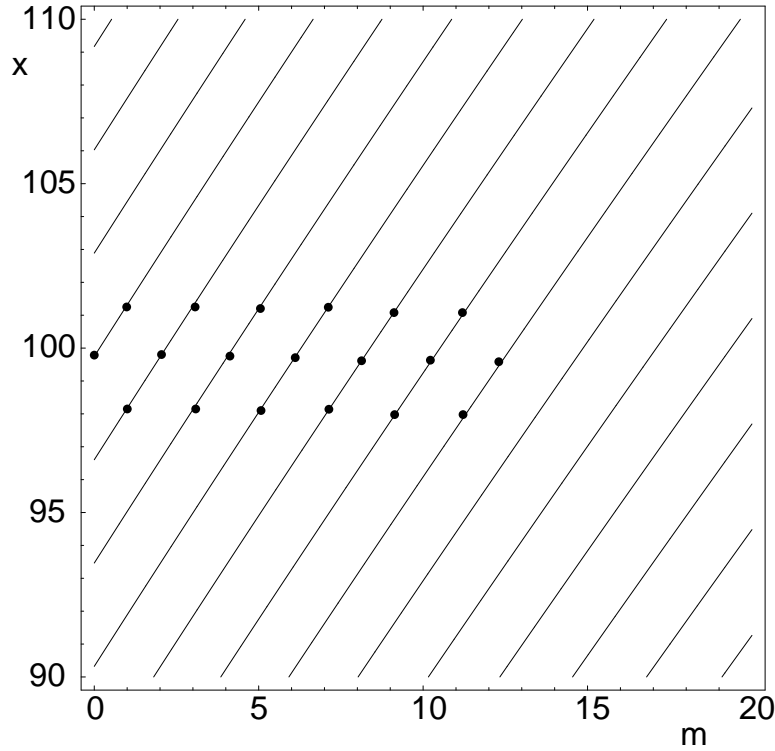


Figure D.3: Roots of the Bessel function of the first kind, $J_m(x)$, for arguments x around 100 and small m . The dots are examples of $J_m(x) = 0$ for small integers m and $x \approx 100$.

If $\mu c_0/D$ is small against 1 eq. (D.14), which represents the eigenvalue problem of the stability analysis, is precisely a Bessel equation, and the solutions $\delta n(r)$ are the Bessel functions of first and second kind $J_m(kr)$, $Y_m(kr)$, respectively⁴, for a given azimuthal modulation number m with longitudinal wave vector $k = \sqrt{(\frac{\Lambda}{eD} + \frac{n_0 u}{\epsilon D}) \frac{\partial \rho}{\partial n}}$. For general $\mu c_0/D$ eq. (D.14) has a complicated combination of different Bessel functions as the solution for $\delta n(r)$. The important point to note here is that the solution of eq. (D.14) does not yield any dependence of Λ on m .

The selection of azimuthal modes, i. e. which m lead to a positive real part of Λ , could still come from boundary conditions via the selection of the allowed values for k . If we assume Dirichlet boundary conditions at the two contacts $\delta n(r)$ must vanish at both R_1 and R_2 . Since for a given m the general solution for $\delta n(r)$ is a linear combination of J_m and Y_m , one boundary condition, say the one at R_1 , can always be fulfilled (if one assumes that R_1 is vanishingly small $\delta n(r)$ will become identical to just J_m). The outer contact radius R_2 is typically of the order of 10^{-1} cm.

²in the spatially two-dimensional case it is important to consider fluctuations of the electrical potential Ψ instead of the electrical field so that $\delta \underline{\mathcal{E}} = -\underline{\nabla} \delta \Psi$ still holds.

³a similar problem already exists in a finite rectangular system if one tries to take into account boundary conditions at the contacts.

⁴here again we have made use of the approximation that $\rho(n, \mathcal{E})$ does not change too much across the sample radius.

The instability regime for the k vectors, which for n-GaAs can, for this simple estimate, be taken from the results of [Gaa94], lie in the range of approximately 10^3 to $5 \cdot 10^6 \text{ cm}^{-1}$. Thus the arguments of the Bessel functions $x = kr$ must be from a range of 10^2 to $5 \cdot 10^5$. For large arguments x the Bessel functions approximate the trigonometric function of sin and cos, which means that their roots occur every $\Delta x = \pi$. For small m (say up to $m = 20$) this holds already to a high precision for arguments of $x = 100$ or above. Moreover, with large x the roots tend to be at the same values x_i for all even and for all odd m , respectively. This is visualized in Fig. D.3 where the roots of $J_m(x)$ are plotted for x around 100 (as an example) and small m (here only integer values of m are of relevance). So even if one had an entirely unrealistically thin k -band of instability (and has a very precise value for R_2) one would find an allowed solution for any (or at least every second) m . Thus even taking into account boundary conditions the linear stability analysis does not select any specific azimuthal modes.

Bibliography

- [Ama01] A. Amann, A. Wacker, L. L. Bonilla, and E. Schöll. Field domains in semiconductor superlattices: Dynamic scenarios of multistable switching. In N. Miura, editor, *Proc. 25th International Conference on the Physics of Semiconductors*, Berlin, 2001. Springer. in print.
- [Aok81] K. Aoki, T. Kobayashi, and K. Yamamoto. Periodic oscillations and turbulence of hot-carrier plasma at 4.2K in n-GaAs. *J. Physique Colloque C*, C7, 51–57, 1981.
- [Aok98] K. Aoki and S. Fukui. Nucleation process of a filamentary current during impact ionization avalanche in n-GaAs. *J. Phys. Soc. Jpn.*, 67, 1106–1109, 1998.
- [Aok99a] K. Aoki. Pattern dynamics of a current density filament during impact ionization avalanche in n-GaAs. In D. Gershoni, editor, *Proc. 24th International Conference on The Physics of Semiconductors (ICPS-24)*, Jerusalem, Israel, Singapore, 1999. World Scientific. (published on CD).
- [Aok99b] K. Aoki and S. Fukui. Dynamics of filamentary currents in Corbino discs under magnetic fields. *Physica B*, 272, 274–278, 1999.
- [Aok01a] K. Aoki. Anomalous brightening of donor-band excitation photoluminescence caused by a pulsed electric field in n-GaAs. In M. Suezawa, editor, *Proc. 9th International Conference on Shallow-Level Centers in Semiconductors*, Amsterdam, 2001. Elsevier. in print.
- [Aok01b] K. Aoki. Self-organization of current density filaments in n-GaAs Corbino disks. In N. Miura, editor, *Proc. 25th International Conference on the Physics of Semiconductors*, Berlin, 2001. Springer. in print.
- [Ash76] N. W. Ashcroft and N. D. Mermin. *Solid State Physics*. Saunders College, Philadelphia, 1976.
- [Bas76] N. G. Basov, A. G. Molchanov, A. S. Nasibov, and A. Z. Obidin. Solid state streamer lasers. *Sov. Phys. JETP*, 43(5), 912–917, 1976.
- [Bon94] L. L. Bonilla, J. Galán, J. A. Cuesta, F. C. Martínez, and J. M. Molera. Dynamics of electric field domains and oscillations of the photocurrent in a simple superlattice model. *Phys. Rev. B*, 50, 8644, 1994.

- [Bra89] A. Brandl, M. Völcker, and W. Prettl. Reconstruction of the spatial structure of current filaments in n-GaAs. *Appl. Phys. Lett.*, 55, 238, 1989.
- [Chr94a] T. Christen. Nonequilibrium phase transitions and current filaments in extrinsic semiconductors. *Z. f. Naturforsch.*, 49a, 851–855, 1994.
- [Chr94b] T. Christen. The velocity of current filaments in weak magnetic fields. *Z. f. Naturforsch.*, 49a, 847–850, 1994.
- [Del70] B. C. Deloach and D. L. Scharfetter. Device physics of TRAPATT oscillators. *IEEE Trans. Electron Devices*, 17(1), 9–21, 1970.
- [Dha87] S. K. Dhali and P. F. Williams. Two-dimensional studies of streamers in gases. *J. Appl. Phys.*, 62(12), 4696–4707, 1987.
- [D’y88] M. I. D’yakonov and V. Yu. Kachorovskii. Theory of streamer discharge in semiconductors. *Sov. Phys. JETP*, 67(5), 1049–1054, 1988.
- [D’y89] M. I. D’yakonov and V. Yu. Kachorovskii. Streamer discharge in a homogeneous field. *Sov. Phys. JETP*, 68(5), 1070–1074, 1989.
- [Ebe96a] W. Eberle, J. Hirschinger, U. Margull, W. Prettl, V. Novák, and H. Kostial. Visualization of current filaments in n-GaAs by photoluminescence quenching. *Appl. Phys. Lett.*, 68(23), 3329–3331, 1996.
- [Ebe96b] U. Ebert, W. van Saarloos, and C. Caroli. Streamer propagation as a pattern formation problem: Planar fronts. *Phys. Rev. Lett.*, 77(4), 4178–4181, 1996.
- [Ebe97a] W. Eberle, U. Margull, J. Grebler, J. Hirschinger, W. Prettl, H. Kostial, and V. Novák. Rotating filaments in a n-GaAs Corbino disk. *Acta Techn. CSAV*, 42(5), 623–632, 1997.
- [Ebe97b] U. Ebert, W. van Saarloos, and C. Caroli. Propagation and structure of planar streamer fronts. *Phys. Rev. E*, 55(2), 1530–1549, 1997.
- [Foc97] R. J. Focia, E. Schamiloglu, C. B. Fleddermann, F. J. Agee, and J. Gaudet. Silicon diodes in avalanche pulse-sharpening applications. *IEEE Trans. Plasma Science*, 25(2), 138–144, 1997.
- [Gaa94] M. Gaa. Laufende Ladungsdichtewellen beim Stoßionisationsdurchbruch in Halbleitern, 1994. Studienarbeit, Technische Universität Berlin.
- [Gaa95] M. Gaa. Die Simulation raumzeitlicher Dynamik in Halbleitern. Master’s thesis, Technische Universität Berlin, 1995.
- [Gaa96a] M. Gaa, K. Kunihiro, and E. Schöll. Formation dynamics of current filaments. In H. Engel, F.-J. Niedernostheide, H. G. Purwins, and E. Schöll, editors, *Self-Organization in Activator-Inhibitor-Systems: Semiconductors, Gas Discharge, and Chemical Active Media*, pages 38–43. Wissenschaft & Technik Verlag, Berlin, 1996.

- [Gaa96b] M. Gaa, R. E. Kunz, and E. Schöll. Dynamics of nascent current filaments in low-temperature impurity breakdown. *Phys. Rev. B*, 53, 15971, 1996.
- [Gaa96c] M. Gaa, R. E. Kunz, and E. Schöll. Spatio-temporal dynamics of filament formation induced by impurity impact ionization in GaAs. In K. Hess, J. P. Leburton, and U. Ravaioli, editors, *Proc. 9th Int. Conf. on Hot Carriers in Semiconductors*, pages 347–351, New York, 1996. Plenum.
- [Gaa96d] M. Gaa, R. E. Kunz, E. Schöll, W. Eberle, J. Hirschinger, and W. Prettl. Spatial structure of impact-ionization induced current filaments in n-GaAs films. *Semicond. Sci. Technol.*, 11, 1646–1655, 1996.
- [Gaa96e] M. Gaa and E. Schöll. Traveling carrier density waves in n-GaAs at low-temperature impurity breakdown. *Phys. Rev. B*, 54(23), 16733, 1996.
- [Gaj91] H. Gajewski, B. Heinemann, R. Nürnberg, H. Langmach, G. Telschow, and K. Zarachias. Manual of the two-dimensional semi-conductor analysis package (ToSCA) (unpublished), 1991.
- [Gaj93] H. Gajewski. Analysis und Numerik von Ladungstransport in Halbleitern. Report ISSN 0942-9077, WIAS Berlin, 1993.
- [Hir97a] J. Hirschinger, W. Eberle, W. Prettl, F.-J. Niedernostheide, and H. Kostial. Self-organized current-density patterns and bifurcations in n-GaAs with a circular contact symmetry. *Phys. Lett. A*, 236, 249–255, 1997.
- [Hir97b] J. Hirschinger, U. Margull, H. Klimenta, W. Prettl, H. Kostial, and V. Novák. Laterally oscillating current-filaments in n-GaAs layers with point contacts. *Acta Techn. CSAV*, 42(6), 723–731, 1997.
- [Hir97c] J. Hirschinger, F.-J. Niedernostheide, W. Prettl, V. Novák, M. Cukr, J. Oswald, and H. Kostial. Current filamentation in n-gaas samples with different contact geometries. *Acta Techn. CSAV*, 42(6), 661–667, 1997.
- [Hir97d] J. Hirschinger, F.-J. Niedernostheide, W. Prettl, V. Novák, and H. Kostial. Self-organized current filament patterns and bifurcations in n-GaAs Corbino disks. *phys. stat. sol.*, 204, 477–480, 1997.
- [Hir97e] J. Hirschinger, F.-J. Niedernostheide, W. Prettl, V. Novák, and H. Kostial. Spatial oscillations of current filaments. *Acta Techn. CSAV*, 42(6), 699–704, 1997.
- [Hir98] J. Hirschinger, H. Kostial, and W. Prettl. Visualization of lateral movement of current filaments in n-GaAs. *Sol. Stat. Comm.*, 106(4), 187–192, 1998.
- [Hir99] J. Hirschinger. *Struktur und Dynamik von Stromfilamenten*. Verlag Mainz, Aachen, 1999.

- [Hir00] J. Hirschinger, F.-J. Niedernostheide, W. Prettl, and V. Novák. Current filament patterns in n-GaAs layers with different contact geometries. *Phys. Rev. B*, 61(3), 1952–1958, 2000.
- [Hüp93a] G. Hüpper. *Magnetfeldinduzierte raum-zeitliche Strukturbildung beim Stromtransport in Halbleitern*. Dissertation TU Berlin, Harri Deutsch, Frankfurt am Main, 1993.
- [Hüp93b] G. Hüpper, K. Pyragas, and E. Schöll. Complex dynamics of current filaments in the low temperature impurity breakdown regime of semiconductors. *Phys. Rev. B*, 47, 15515, 1993.
- [Hüp93c] G. Hüpper, K. Pyragas, and E. Schöll. Complex spatio-temporal dynamics of current filaments in crossed electric and magnetic fields. *Phys. Rev. B*, 48, 17633, 1993.
- [Kas94] J. Kastrup, H. T. Grahn, K. Ploog, F. Prengel, A. Wacker, and E. Schöll. Multistability of the current-voltage characteristics in doped GaAs-AlAs superlattices. *Appl. Phys. Lett.*, 65, 1808, 1994.
- [Keh95] B. Kehrner, W. Quade, and E. Schöll. Monte Carlo simulation of impact-ionization-induced breakdown and current filamentation in δ -doped GaAs. *Phys. Rev. B*, 51, 7725, 1995.
- [Kli99] H. Klimenta, M. Alshuth, W. Prettl, and H. Kostial. Discontinuities and hysteresis in the I-V characteristics of n-GaAs at low temperatures. *phys. status solidi (a)*, 176(2), 1017–1024, 1999.
- [Kuh93] T. Kuhn, G. Hüpper, W. Quade, A. Rein, E. Schöll, L. Varani, and L. Reggiani. Microscopic analysis of noise and nonlinear dynamics in p-type germanium. *Phys. Rev. B*, 48, 1478, 1993.
- [Kun92] R. E. Kunz and E. Schöll. Globally coupled dynamics of breathing current filaments in semiconductors. *Z. Phys. B*, 89, 289, 1992.
- [Kun96a] K. Kunihiro, M. Gaa, and E. Schöll. Dynamics of current filaments in n-type GaAs under the influence of a transverse magnetic field. In M. Scheffler and R. Zimmermann, editors, *Proc. 23rd Int. Conf. Physics of Semiconductors*, volume 1, pages 137–140, Singapore, 1996. World Scientific.
- [Kun96b] R. E. Kunz and E. Schöll. Dynamics of stochastically induced and spatially inhomogeneous impurity breakdown in semiconductors. *Z. Phys. B*, 99, 185, 1996.
- [Kun96c] R. E. Kunz, E. Schöll, H. Gajewski, and R. Nürnberg. Low-temperature impurity breakdown in semiconductors: an approach towards efficient device simulation. *Sol. State El.*, 39(8), 1155–1164, 1996.
- [Kun97a] K. Kunihiro, M. Gaa, and E. Schöll. Formation of current filaments in n-type GaAs under crossed electric and magnetic fields. *Phys. Rev. B*, 55(4), 2207–2213, 1997.

- [Kun97b] K. Kunihiro, M. Gaa, and E. Schöll. Influence of external circuits on filamentary current flow during impurity breakdown in n-type GaAs. *Electronics Letters*, 33(14), 1261–1262, 1997.
- [Mar96] U. Margull. Rotating current filaments in n-GaAs layers with Corbino contacts. In H. Engel, F.-J. Niedernostheide, H. G. Purwins, and E. Schöll, editors, *Selforganization in Activator-Inhibitor-Systems*, page 50. Wissenschaft & Technik Verlag, Berlin, 1996.
- [May87] K. M. Mayer, R. Gross, J. Parisi, J. Peinke, and R. P. Huebener. Spatially resolved observation of current filament dynamics in semiconductors. *Solid State Comm.*, 63, 55, 1987.
- [May88] K. M. Mayer, J. Parisi, and R. P. Huebener. Imaging of self-generated multifilamentary current patterns in GaAs. *Z. Phys. B*, 71, 171, 1988.
- [Min94] A. M. Minarskiĭ and P. B. Rodin. Long-wavelength instability of impact-ionization waves in diode structures. *Technical Physics Letters*, 20(6), 490–491, 1994. [Pis'ma Zh. Tekn. Fiz. **20**, 38 (1994)].
- [Min97a] A. M. Minarskiĭ and P. B. Rodin. Transverse stability of an impact-ionization front in a Si p^+-n-n^+ structure. *Semiconductors*, 31(4), 366–370, 1997. [Fiz. Tekn. Poluprovodn. **31**, 432 (1997)].
- [Min97b] A. M. Minarsky and P. B. Rodin. Transverse instability and inhomogeneous dynamics of superfast impact ionization waves in diode structures. *Sol. State El.*, 41(6), 813–824, 1997.
- [Min00] A. M. Minarskiĭ and P. B. Rodin. Critical voltage growth rate when initiating the ultrafast impact ionization front in a diode structure. *Semiconductors*, 34(6), 665–667, 2000.
- [Mor98] H. Mori and Y. Kuramoto. *Dissipative structures and chaos*. Springer, Berlin, 2 edition, 1998.
- [Mul64] W. W. Mullins and R. F. Sekerka. Stability of a planar interface during solidification of a dilute binary alloy. *J. Appl. Phys.*, 35(2), 444–451, 1964.
- [Nic97] B. Niceno. Easymesh. <http://www-dinma.univ.trieste.it/~nirftc/research/easymesh/>, University of Trieste 1997.
- [Nie98] F.-J. Niedernostheide, J. Hirschinger, W. Prettl, V. Novák, and H. Kostial. Oscillations of current filaments in n-GaAs caused by a magnetic field. *Phys. Rev. B*, 58(8), 4454–4458, 1998.
- [Nov95a] V. Novák and W. Prettl. Current filamentation in dipolar electric fields. In F.-J. Niedernostheide, editor, *Nonlinear Dynamics and Pattern Formation in Semiconductors*, pages 144–167. Springer, Berlin, 1995.

- [Nov95b] V. Novák, C. Wimmer, and W. Prettl. Impurity-breakdown-induced current filamentation in a dipolar electric field. *Phys. Rev. B*, 52(12), 9023–9030, 1995.
- [Nov96] V. Novák, J. Hirschinger, W. Eberle, C. Wimmer, and W. Prettl. Simplified 2-D model of current filamentation in low temperature breakdown regime of semiconductors. *Acta Techn. CSAV*, 41, 553, 1996.
- [Nov97a] V. Novák, J. Hirschinger, W. Prettl, and F.-J. Niedernostheide. 2-D stationary model of current filament in point contact geometry. *Acta Techn. CSAV*, 42(6), 685–692, 1997.
- [Nov97b] V. Novák, J. Hirschinger, W. Prettl, F.-J. Niedernostheide, M. Cukr, and J. Oswald. Mobility measurements in current filaments. *Acta Techn. CSAV*, 42(6), 705–710, 1997.
- [Nov98a] V. Novák, J. Hirschinger, F.-J. Niedernostheide, W. Prettl, M. Cukr, and J. Oswald. Direct experimental observation of the hall angle in the low-temperature breakdown regime of n-GaAs. *Phys. Rev. B*, 58(19), 13099–13102, 1998.
- [Nov98b] V. Novák, J. Hirschinger, W. Prettl, and F.-J. Niedernostheide. Current filamentation in point contact geometry and its 2D stationary model. *Semicond. Sci. Technol.*, 13, 756–761, 1998.
- [Pel88] P. Pelcé. *Dynamics of Curved Fronts*. Academic Press, San Diego, 1988.
- [Pre92] W. H. Press, B. P. Flannery, S. A. Teukolsky, and W. T. Vetterling. *Numerical Recipes in C (2nd ed.)*. Cambridge University Press, Cambridge, 1992.
- [Pre94] F. Prengel, A. Wacker, and E. Schöll. Simple model for multistability and domain formation in semiconductor superlattices. *Phys. Rev. B*, 50, 1705, 1994. *ibid* **52**, 11518 (1995).
- [Pre97] W. Prettl and V. Novák. Visualization of impact ionization generated current filaments in semiconductors. *Acta Techn. CSAV*, 42(6), 647–659, 1997.
- [Qua94] W. Quade, G. Hüpper, E. Schöll, and T. Kuhn. Monte Carlo simulation of the nonequilibrium phase transition in p-type Ge at impurity breakdown. *Phys. Rev. B*, 49, 13408, 1994.
- [Rei98] A. Reimann. Nichtlineare Dynamik von Stromfilamenten in gekreuzten elektrischen und magnetischen Feldern. Master's thesis, Technische Universität Berlin, 1998.
- [Saa98] W. van Saarloos. Three basic issues concerning interface dynamics in nonequilibrium pattern formation. *Physics Reports*, 301, 9–43, 1998.
- [Sch82] E. Schöll. Bistability and nonequilibrium phase transitions in a semiconductor recombination model with impact ionization of donors. *Z. Phys. B*, 46, 23, 1982.

- [Sch87] E. Schöll. *Nonequilibrium Phase Transitions in Semiconductors*. Springer, Berlin, 1987.
- [Sch90] E. Schöll and D. Drasdo. Nonlinear dynamics of breathing current filaments in n-GaAs and p-Ge. *Z. Phys. B*, 81, 183, 1990.
- [Sch96a] G. Schwarz, F. Pregel, E. Schöll, J. Kastrup, H. T. Grahn, and R. Hey. Electric field domains in intentionally perturbed semiconductor superlattices. *Appl. Phys. Lett.*, 69(5), 626–628, 1996.
- [Sch96b] G. Schwarz, A. Wacker, F. Pregel, E. Schöll, J. Kastrup, H. T. Grahn, and K. Ploog. Influence of imperfections and weak disorder on domain formation in superlattices. *Semicond. Sci. Technol.*, 11(4), 475–482, 1996.
- [Sch97] G. Schwarz and E. Schöll. Simulation of current filaments in semiconductors with point contacts and Corbino disks. *Acta Techn. CSAV*, 42(6), 669–684, 1997.
- [Sch98a] E. Schöll, editor. *Theory of Transport Properties of Semiconductor Nanostructures*, volume 4 of *Electronic Materials Series*. Chapman and Hall, London, 1998.
- [Sch98b] E. Schöll, G. Schwarz, and A. Wacker. Nonlinear and oscillatory electronic transport in superlattices as a probe of structural imperfections. *Physica B*, 249–251(1–4), 961–965, 1998.
- [Sch99a] G. Schwarz, C. Lehmann, and E. Schöll. Symmetry-breaking current instability in Corbino disks. In D. Gershoni, editor, *Proc. 24th International Conference on The Physics of Semiconductors (ICPS-24)*, Jerusalem, Israel, Singapore, 1999. World Scientific. (published on CD).
- [Sch99b] G. Schwarz, C. Lehmann, and E. Schöll. Symmetry-breaking multiple current filamentation in n-GaAs. *Physica B*, 272, 270–273, 1999.
- [Sch00a] G. Schwarz, C. Lehmann, A. Reimann, E. Schöll, J. Hirschinger, W. Prettl, and V. Novák. Current filamentation in n-GaAs thin films with different contact geometries. *Semicond. Sci. Technol.*, 15, 593–603, 2000.
- [Sch00b] G. Schwarz, C. Lehmann, and E. Schöll. Self-organized symmetry-breaking current filamentation and multistability in Corbino disks. *Phys. Rev. B*, 61(15), 10194–10200, 2000.
- [Sch00c] G. Schwarz, E. Schöll, R. Nürnberg, and H. Gajewski. Simulation of current filamentation in an extended drift diffusion model. In B. Fiedler, K. Gröger, and J. Sprekels, editors, *Proc. Equadiff 99*, volume 2, pages 1334–1336, Singapore, 2000. World Scientific Publishing.
- [Sch01] E. Schöll. *Nonlinear spatio-temporal dynamics and chaos in semiconductors*. Cambridge University Press, Cambridge, 2001. Nonlinear Science Series, Vol. 10.

- [Sel84] S. Selberherr. *Analysis and Simulation of Semiconductor Devices*. Springer, Wien, New York, 1984.
- [Sha92] M. P. Shaw, V. V. Mitin, E. Schöll, and H. L. Grubin. *The Physics of Instabilities in Solid State Electron Devices*. Plenum Press, New York, 1992.
- [Spa94] J. Spangler, B. Finger, C. Wimmer, W. Eberle, and W. Prettl. Magnetic-field-induced lateral displacements of current filaments in n-GaAs. *Semicond. Sci. Technol.*, 9, 373, 1994.
- [Tei83] S. W. Teitsworth, R. M. Westervelt, and E. E. Haller. Nonlinear oscillations and chaos in electrical breakdown in Ge. *Phys. Rev. Lett.*, 51, 825, 1983.
- [Vit93] P. A. Vitello, B. M. Penetrante, and J. N. Bardsley. Multi-dimensional modeling of the dynamic morphology of streamer coronas. In B. M. Penetrante and S. E. Schultheis, editors, *Proc. NATO Advanced Research Workshop on Non-Thermal Plasma Techniques for Pollution Control*, volume A, pages 249–271. Springer, Berlin, Heidelberg, New York, 1993.
- [Vit94] P. A. Vitello, B. M. Penetrante, and J. N. Bardsley. Simulation of negative-streamer dynamics in nitrogen. *Phys. Rev. E*, 49(6), 5574–5598, 1994.